Thesis for the Degree of Licentiate of Technology

Modelling and Retrieval of Forest Parameters from Synthetic Aperture Radar Data

Maciej Jerzy Soja

CHALMERS

Department of Earth and Space Sciences
Chalmers University of Technology
Gothenburg, Sweden 2012

Modelling and Retrieval of Forest Parameters from Synthetic Aperture Radar Data
Maciej Jerzy Soja

Technical Report 51L,
Radar Remote Sensing Group
Department of Earth and Space Sciences
Chalmers University of Technology
SE–412 96 Gothenburg, Sweden
Phone: +46 (0)31 772 1000

Cover: A gradual transition between two co-registered images of Remningstorp is shown. To the left, a biomass map estimated from P-band SAR using the model introduced in Paper A is shown. The SAR data were obtained within the BioSAR 2010 experiment (heading 200°). To the right, a Google Earth image of the same region is shown.

Printed by Chalmers Reproservice
Chalmers University of Technology
Gothenburg, Sweden 2012

"Genius is one percent inspiration,
ninety-nine percent transpiration."
Thomas Alva Edison (1847–1931)

dla dziadków Jasiów

Modelling and Retrieval of Forest Parameters from Synthetic Aperture Radar Data
MACIEJ JERZY SOJA
Department of Earth and Space Sciences
Chalmers University of Technology

Abstract

Currently, one of the most uncertain factors in the global carbon cycle models lies in the terrestrial carbon stock, mainly forests. The available methods for global forest resource mapping provide only rough estimates of biomass, the most relevant practical quantity related to carbon stock.

Spaceborne synthetic aperture radar (SAR) is a tool potentially suitable for global forest monitoring. As an active microwave sensor, SAR has the advantage of being independent of weather and external illumination. Spaceborne SAR can be designed for different frequencies and with resolutions as low as a few metres. Moreover, SAR systems operating at frequencies below L-band show good sensitivity to biomass. A spaceborne solution introduces also the possibility of frequent acquisitions, which is beneficial in applications such as detection of unlawful clear-cutting, storm damages, and forest fires.

In the first paper, a new biomass retrieval model for boreal forest using polarimetric, airborne P-band SAR backscatter is presented. The model is based on two main SAR quantities: the HV backscatter gamma nought and the HH/VV backscatter ratio, together with a topographic correction. Data from the two airborne experiments BioSAR 2007 and BioSAR 2008, performed in two distinct test sites Remningstorp and Krycklan, were used for this study. The model was compared to other, previously published models in a set of tests. In one of the tests, the models were evaluated across sites, i.e. training was done with data from one test site, and the models were validated using data from the other test site. Stand-wise root-mean-square errors of 40–59 tons/ha, or 22–32% of the mean biomass were observed for across-site validation.

In the second paper, a forward model for extended covariance matrix prediction for boreal forest in P-band SAR is presented. Data from BioSAR 2007 campaign were used for model derivation. The model is able to predict backscatter at HH, HV, and VV, together with the complex correlation between HH and VV, and complex correlation coefficients for three interferometric pairs (one for each polarisation). The forward model builds on a physical model and linear regression of BioSAR 2007 data. The model is further developed in the third paper. In the fourth paper, a tropical forest scenario is added, derived from the data acquired within the TropiSAR 2009 experiment.

In the fifth paper, spaceborne SAR is used to delineate wind-thrown trees and clear-cuts during a controlled experiment conducted in the test site of Remningstorp in 2009. Data from three satellites were used: ALOS PALSAR (L-band), RADARSAT-2 (C-band), and TerraSAR-X (X-band). The detection capabilities vary for the different satellites due to different resolutions, and also due to different scattering properties. It is observed, that TerraSAR-X is suitable for storm damage detection due to its high resolution. ALOS PALSAR is suitable for detection of clear-cuts due to its sensitivity to biomass.

Keywords: synthetic aperture radar (SAR), forest, biomass estimation, modelling

Appended papers

This thesis is based on the following papers:

Paper A: **M. J. Soja**, G. Sandberg, and L. M. H. Ulander. Biomass Retrieval for Boreal Forests using P-band SAR Backscatter. Submitted to *IEEE Transactions on Geoscience and Remote Sensing*, February 2012.

Paper B: **M. J. Soja** and L. M. H. Ulander. A Hybrid Model for Interferometric and Polarimetric P-band SAR Imaging of Forests. *Proceedings for "PolInSAR 5th International Workshop on Science and Applications of SAR Polarimetry and Polarimetric Interferometry"*, Frascati, Italy, 24–28 January 2011 (ESA SP-695, March 2011).

Paper C: **M. J. Soja**. Forward Model for Interferometric and Polarimetric P-band SAR Imaging of Forests. Manuscript submitted to DLR as a part of the WP20 Report for the ESA project *Development of Algorithms for Forest Biomass Retrieval*, June 2011.

Paper D: **M. J. Soja**. Tropical Forest Update to Paper C. Manuscript submitted to DLR as annex to Paper C, September 2011.

Paper E: L. E. B. Eriksson, J. E. S. Fransson, **M. J. Soja**, and M. Santoro. Spaceborne SAR for detection of boreal wind-thrown forest and clear-cuts. Submitted to *Remote Sensing of Environment*, August 2011.

Related papers

The following papers are related to the work presented in this thesis, but they have not been appended:

Paper 1: **M. J. Soja**, G. Sandberg, and L. M. H. Ulander. Topographic Correction for Biomass Retrieval from P-band SAR Data in Boreal Forests. *Proceedings of IEEE International Geoscience and Remote Sensing Symposium (IGARSS)*, Honolulu, HI, USA, 25–30 July 2010, pp. 4776–4779.

Paper 2: J. E. S. Fransson, A. Pantze, L. E. B. Eriksson, **M. J. Soja**, and M. Santoro. Mapping of windthrown forests using satellite SAR images. *Proceedings of IEEE International Geoscience and Remote Sensing Symposium (IGARSS)*, Honolulu, HI, USA, 25–30 July 2010, pp. 1242–1245.

Paper 3: G. Sandberg, **M. J. Soja**, and L. M. H. Ulander. Impact and Modeling of Topographic Effects on P-band SAR Backscatter from Boreal Forests. *Proceedings of IEEE International Geoscience and Remote Sensing Symposium (IGARSS)*, Vancouver, BC, Canada, 24–29 July 2011, pp. 3522–3525.

Paper 4: L. M. H. Ulander, G. Sandberg, and **M. J. Soja**. Biomass retrieval algorithm based on P-band BioSAR experiments of boreal forest. *Proceedings of IEEE International Geoscience and Remote Sensing Symposium (IGARSS)*, Vancouver, BC, Canada, 24–29 July 2011, pp. 4245–4248.

Paper 5: L. M. H. Ulander, A. Gustavsson, P. Dubois-Fernandez, X. Depuis, J. E. S. Fransson, J. Holmgren, J. Wallerman, L. E. B. Eriksson, G. Sandberg, and **M. J. Soja**. BioSAR 2010 — A SAR Campaign in Support to the BIOMASS Mission. *Proceedings of IEEE International Geoscience and Remote Sensing Symposium (IGARSS)*, Vancouver, BC, Canada, 24–29 July 2011, 1528–1531.

Acknowledgements

First and foremost, I would like to thank my supervisor and mentor, Lars Ulander, for making the writing of this thesis possible. Thank you for your guidance and support. Thank you for the countless hours spent on reading and correcting my papers.

★

Also, I would like to thank my two assistant supervisors: Leif Eriksson and Johan Fransson, for being there for me whenever necessary. Also, thank you, Leif, for being a great leader for the Radar Remote Sensing group. Thanks to you, the atmosphere in the group is outstanding.

★

I would like to dedicate special thanks to Gustaf Sandberg and Anders Berg, my superb colleagues and friends. Thank you for being my sounding board, for your feedback and input. Thank you for your constant support. Thank you for making this thesis so much better.

★

Many thanks to my current and former colleagues from the Radar Remote Sensing Group, Jan Torgrimsson, Gisela Carvajal, Annelie Wyholt, and Jan Askne, as well as Mattias Andersson and Maurizio Santoro, for all the fruitful discussions, helpful comments, and valuable input. Thank you for your contribution to the great atmosphere in our group.

★

Special thanks to Donal, Marston, and Matthew, for being my good friends and my English gurus. Many thanks to all my other colleagues and staff from the department of Earth and Space Sciences. Thank you all for keeping the department wheels in motion and for making the coffee breaks very enjoyable.

★

Additionally, I would like to express my gratitude to my colleagues from the German Aerospace Center (DLR), Kostas Papathanassiou, Stefan Sauer, Florian Kugler, and Seung-Kuk Lee, for their help during our joint projects. I am very thankful for your time and dedication. I am looking forward to further cooperation with you all.

★

I would also like to thank Swedish National Space Board (SNSB) and European Space Agency (ESA) for the funding of my research.

★

Thank you, my loving and beloved family, for providing motivation and support whenever needed. Thank you, my awesome friends, for enlightening the darkness during winters and for making the summer days less rainy. I love you all!

Maciej

Contents

Chapter 1

Introduction

1.1 Forests in Environment and Human Society

Forests play a vital role in Earth's ecosystems. Through the process of photosynthesis, trees and plants bind CO_2 from the atmosphere, part of which is transformed into carbon stock. Forests provide shelter to countless animal and vegetation species, housing around 80 % of the terrestrial biodiversity [1]. They also take part in the water cycle, prevent soil from erosion, clean water and air from pollutants, etc. At the same time, forests are one of our greatest natural resources. Timber is used as a construction material, for paper production, and as a fuel. Animals and vegetation provide food. Forests also have great recreational values.

Until quite recently, the global effects of human exploitation of forests were negligible due to a small population and low demand, and inefficient harvesting methods. However, as the human population grew rapidly, the demand on forest products increased. With the advent of industrialisation, the harvesting methods became more efficient, and fossil fuels such as coal, gas, and oil became essential to the society. Only in the late 20th century, the first signs of a possible human influence on the global ecosystem were observed. Acid rain, ozone depletion, and global warming are just a few, potentially human-induced threats. Presently, the public awareness of the climate problems is increased, the first measures are taken, and a lot of research is centred around Earth system science and climate change (see [2] and references therein).

One of the greatest concerns is the influence of deforestation on global carbon dioxide emissions. During the last 50 years, a steady increase of the atmospheric CO_2 has been observed [3, 4]. Some sources state, that as much as 20 % of the global carbon dioxide emissions come from deforestation [2, 5]. However, the exact effect of deforestation is unknown. The single largest uncertainty in the current carbon cycle models lies in the terrestrial carbon sink, mainly forests [4]. The most relevant, measurable quantity directly related to the carbon distribution in biosphere is biomass, the mass of the organic matter living in a certain region. Since forests account for over 80 % of the terrestrial above ground biomass, and around 50 % of biomass is carbon [6], accurate, global forest biomass maps are required to improve global carbon cycle modelling. The possibility of periodic updates should also exist in order to be able to detect unlawful deforestation, aid disaster handling, and improve forest management.

1.2 Remote Sensing of Forests

Since forests cover more than 31 % of Earth's total land surface [1], satellite remote sensing is the only applicable method for frequent, global biomass mapping. This can be done in several ways. Optical methods have long been used for this task. However, these methods are inaccurate and sensitive to weather conditions [6]. This is especially problematic around the equator, where most of the high-biomass tropical rainforests are situated, but also where the cloud cover is the most persistent. Small-footprint lidar scanning is currently the most accurate method for remote forest mapping [7]. However, spaceborne application of this technique is difficult, mostly due to complications such as large footprint and low coverage [6].

Synthetic aperture radar (SAR) does not suffer from the same disadvantages as the optical and lidar sensors. As an active microwave sensor, SAR carries its own illumination and is weather independent. Thanks to the synthetic aperture technique, the resolution of a spaceborne SAR system can be of the order of metres. Moreover, many studies show that P-band SAR (around 0.22–0.45 MHz) is suitable for forest biomass mapping [8–20]. Although SAR mapping at VHF-band gives even better results, as shown by the CARABAS-system operational at 20–90 MHz (see [21] and references therein), the large ionospheric influence makes the VHF-band unsuitable for spaceborne use [22].

Spaceborne use of P-band SAR has previously been impossible due to frequency restrictions. However, after the World Radiocommunication Conference in 2003, a narrow band within the P-band has been opened for secondary use (432–438 MHz, wavelengths around 69 cm). A fully polarimetric P-band SAR satellite system called BIOMASS has been proposed to European Space Agency (ESA) for the 7th Earth Explorer mission [19, 23, 24]. The major part of the work presented in this thesis has been done within the feasibility study for this mission.

1.3 Outline of this Thesis

This thesis is concentrated on SAR imaging of forests. It is structured as follows:

- In Chapter 2, the basic radar and SAR theory is presented. The most important equations dealing with resolution, ranging, and Doppler measurements are explained. Some examples of SAR imagery are shown, and the differences between SAR and optical imaging are pointed out. SAR polarimetry and interferometry are also introduced. Different scattering mechanisms are described.
- In Chapter 3, the appended papers are presented. In Paper A, biomass retrieval from P-band SAR is assessed. In Papers B, C, and D, a forward model for polarimetric and interferometric P-band SAR modelling is presented. In Paper E, storm damage and clear cut detection at L-, C-, and X-band with spaceborne SAR is evaluated.
- In Chapter 4, the thesis is summed up and conclusions are drawn. Some ideas for future work are also mentioned.

Chapter 2

Synthetic Aperture Radar Principles

2.1 Radar Basics

Radar stands for ***ra**dio **d**etection **a**nd **r**anging* [25,26]. Although the term "radar" was first introduced by the US Navy in 1940, the development of radar started in the beginning of the 20th century. Radar was initially used, as the name suggests, only for detection and ranging of military targets. Nowadays, the functions of radar extend far beyond that, including velocity measurements, shape and size determination of objects, angular measurements, 2- and 3-dimensional mapping, etc. Radar applications include parking assistance in cars, traffic speed measurements, airport surveillance, rain rate mapping and weather monitoring, missile detection, missile guidance, earth observations from satellites, satellite and space debris monitoring from ground, and many others.

Radar is an active remote sensing technique in which an electromagnetic (EM) signal is transmitted, and the reflected echoes are detected and studied[1]. Advantages of radar are many. Since radar is an active system, no external illumination is needed. Also, the terrestrial atmosphere is almost transparent to EM waves with frequencies between a few hundred MHz and approximately 10 GHz [27]. In practice, this means that most radar systems are unaffected by clouds, rain, wind, etc. Also, the choice of frequency gives many possibilities. High frequency means in general better resolution, but small penetration depth. At lower frequencies, penetration capabilities are better, thus making it possible to uncover objects invisible with traditional optical methods. The trade-off is lower resolution and larger antennas. Radar systems are primarily classified by the frequency band used. In Table 2.1, the most commonly used frequency bands are presented.

The transmitted signal usually has a well-determined polarisation, that is the orientation of EM wave oscillations. The returning signal is then measured at a certain polarisation. If the transmission is done with a horizontally polarised antenna (H), and the reception is done with a vertically polarised antenna (V), the polarisation mode is then called VH. Similarly, HH means that horizontally polarised antennas are used both for transmission and reception. If a system is capable of measuring all four combinations (HH, HV, VV, and VH) at the same time, together with their phase information, it is called *fully polarimetric.* If transmission and reception are both done with the same antenna, the radar system is called *monostatic.* In case of two separate antennas, the system is called *bistatic.* Throughout this work, only monostatic systems are used.

In radar imaging, the position of a target is determined by its *range* and *azimuth* (or *cross-range*) positions. Azimuth is the along-track position. *Slant range* is the line-of-sight distance between the antenna

[1] The principles of radar can be compared to echolocation, which is a navigation technique based on ultrasound sensing, used by bats and toothed whales in optically thick environments. Also sonar works similarly to radar, using sound waves in water (hydroacoustics).

phase centre and the target. *Ground range* is the corresponding distance projected to the ground. These dimensions are illustrated in Figure 2.1 and Figure 2.2.

2.1.1 Ranging, Radar Equation, and Radar Cross Section

The ranging technique using radar is straightforward. If the time between transmission and reception of a pulse is T, then the corresponding distance is [26]:

$$R = \frac{cT}{2}, \tag{2.1}$$

where the factor of 2 accounts for the two-way propagation, and c is the propagation velocity of EM waves in the propagation medium. In most radar applications, the latter is air and $c = c_0$ can be assumed, where c_0 is the speed of light in vacuum.

The ratio of the received and transmitted power (P_r and P_t, respectively) for a monostatic radar system is given by the *radar equation* [26, 29]:

$$\frac{P_r}{P_t} = \frac{\sigma \lambda^2 G^2}{(4\pi)^3 R^4 L}, \tag{2.2}$$

where σ is the *radar cross section* (RCS) of the object, λ is the wavelength, G is the gain of the antenna, and L is a factor representing losses. In most practical applications, P_t, λ, G, and L are known system parameters, R is computed from time delay according to (2.1), P_r is measured at the antenna. The estimation of RCS, the main observable in a radar system, is then straightforward. In cases when some system parameters are unknown, a calibration procedure needs to be performed first, using objects with known RCS.

A formal definition of RCS, or σ in (2.2) is [29]:

$$\sigma = \lim_{R \to \infty} 4\pi R^2 \frac{|\mathbf{E}^s|^2}{|\mathbf{E}^i|^2}, \tag{2.3}$$

where $\mathbf{E}^i$ and $\mathbf{E}^s$ are the incident and scattered electric fields, respectively, of the corresponding plane waves. The unit is m^2. RCS describes the effective cross section area of the target as it appears to the radar. RCS depends not only on the dielectric properties and the shape of the target, but also on system parameters, such as polarisation, angle of incidence, and frequency. RCS does not have to be related to the physical size of the studied object. Only for a perfect metallic sphere, and wavelengths much shorter than the dimensions of the sphere, RCS and the geometrical cross section area match exactly.

2.1.2 Range and Azimuth Resolutions

The simplest pulsed radar systems use monochromatic signals to create the transmitted pulses. The range resolution is in that case [26]:

$$\Delta R = \frac{c\tau}{2}, \tag{2.4}$$

where τ is the pulse length. Obviously, the resolution is dependent on the pulse length, and short pulses are more desirable. However, to keep the signal-to-noise ratio high, each pulse has to be either very powerful or long. A trade-off has to be made, which generally results in poor range resolution. Therefore, most modern

Table 2.1: Radar frequency band as defined in [28]. Note: P-band is an older band designation, and does not belong to the IEEE Standard.

Band:	Frequency range:
VHF	30–300 MHz
UHF	300–1000 MHz
L	1–2 GHz
S	2–4 GHz
C	4–8 GHz
X	8–12 GHz
P	*216–450 MHz*

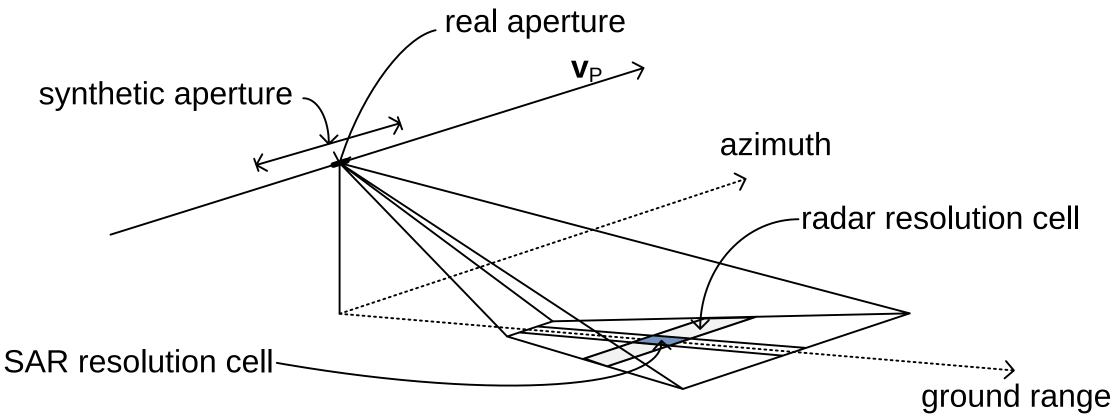

Figure 2.1: Basic SAR geometry under flat-earth approximation. The figure illustrates the principle of synthetic aperture. By synthesising a larger antenna, the resolution cell becomes smaller in azimuth.

radar systems use frequency-modulated pulses instead. This way, the transmitted energy can be distributed over many frequency components, and the effective pulse length can be shortened. For such a system, the range resolution is [25, 29]:

$$\Delta R = \frac{c}{2B}, \tag{2.5}$$

where B is the bandwidth of the pulse. The central frequency of the signal is $f_c = c/\lambda$, where λ is the wavelength.

Two- and three-dimensional imaging can be achieved by sweeping the radar antenna over different directions. If a radar antenna has size D such that:

$$D \gg \lambda, \tag{2.6}$$

then the approximate beamwidth of the antenna can be computed as:

$$\Delta\phi \approx \frac{\lambda}{D}, \tag{2.7}$$

and the size of the illuminated region at distance R is then [29]:

$$\Delta x \approx \Delta\phi R \approx \frac{\lambda R}{D}. \tag{2.8}$$

As it can be observed, Δx depends on both range and antenna size. In order to get a good resolution at long distances, a large antenna is necessary.

2.1.3 Velocity Measurements

Radar systems may be coherent, which means that the phase of the transmitted signal is well known. If a scatterer positioned within the antenna beam is moving radially relative the antenna, a frequency shift will occur. The received signal will have slightly higher frequency if the object is moving towards the antenna, and vice versa. This effect is known as *Doppler shift*[2]. The *Doppler frequency*, that is the frequency shift compared to the nominal carrier frequency, is related to the relative radial velocity v of the scatterer as [29]:

$$f_D = -\frac{2v}{\lambda}. \tag{2.9}$$

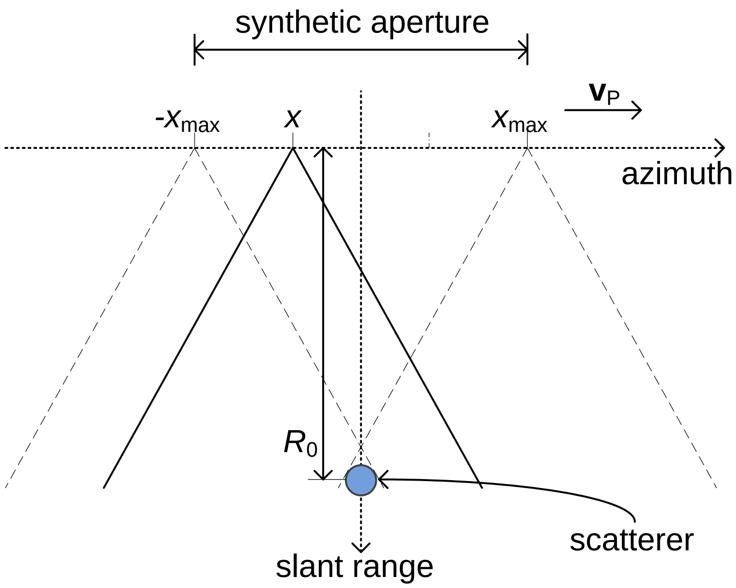

Figure 2.2: Basic SAR geometry seen in the slant range plane. A set of radar measurements is performed by an antenna moving at a constant velocity $\mathbf{v}_P$. At each position, the radial velocity of a stationary scatterer relative the antenna is different.

2.2 Synthetic Aperture Radar

As mentioned in Section 2.1.2, high azimuth resolution in radar requires very large antennas. Such antennas are difficult to design and impractical. In reality, a different approach called *synthetic aperture radar* (SAR) is used for high-resolution radar imaging.

The main idea of SAR is to synthesise a large antenna using multiple acquisitions made with a smaller antenna moving along a known path, see Figure 2.1. A small antenna has a large beamwidth, thus covering a large area on the ground. Each scatterer on the ground is then covered by several consecutive radar acquisitions, each from a different position along the track, see Figure 2.2. The magnitude of the Doppler shift induced by the relative motion depends on the azimuth position of each scatterer. Hence, a Doppler bandwidth is created. Azimuth resolution can now be improved much in the same way as range resolution was improved with the use of frequency-modulated pulses. A short derivation of SAR azimuth resolution is here presented. See also [30].

2.2.1 Resolution

Assume that a stationary scatterer is positioned at range R_0. The position of the antenna at time t is $x = v_P t$, where v_P is the velocity of the radar platform, see Figure 2.2. In the derivation that follows, it is assumed that the boresight (maximum gain) of the antenna is always perpendicular to the velocity vector of the platform (zero squint angle), and that the antenna moves along a straight path. The start-stop approximation is also assumed. Moreover, the imaged area on the ground is assumed to be perfectly flat (flat-earth approximation).

The instantaneous distance to the scatterer is:

$$R(t) = \sqrt{R_0^2 + (v_P t)^2} \approx R_0 \left(1 + \frac{(v_P t)^2}{2R_0^2}\right) \tag{2.10}$$

[2]Doppler shift can be easily observed in everyday life, for example when an ambulance is passing. The frequency of the siren is higher when the ambulance is approaching than when it is leaving.

and the velocity of the scatterer relative the antenna can be computed from (2.10) as:

$$v = \frac{\mathrm{d}R(t)}{\mathrm{d}t} = \frac{v_P^2 t}{R_0}, \tag{2.11}$$

The relative radial movement of the scatterer induces a Doppler shift. The Doppler frequency of this scatterer can be computed using (2.11) in (2.9):

$$f_D(t) = -\frac{2v_P^2 t}{\lambda R_0}, \tag{2.12}$$

where v_P is the velocity of the radar platform. The last time at which the antenna lobe covers the scatterer is $t_{\max}$, and can be computed from the expression for the approximate antenna beamwidth (2.7):

$$t_{\max} = \frac{x_{\max}}{v_P} \approx \frac{\lambda R_0}{2D_x v_P}, \tag{2.13}$$

where $D_x \gg \lambda$ is the antenna size in azimuth direction. Assuming the simplified geometry used in Figure 2.2 (flat earth and zero squint angle), the Doppler bandwidth can be computed as twice the magnitude of the highest Doppler frequency. Using (2.12) and (2.13), the Doppler bandwidth becomes:

$$B_D = 2|f_D(t_{\max})| = \frac{2v_P}{D_x}. \tag{2.14}$$

Equivalently with the expression in (2.5), the azimuth resolution can be computed using Doppler bandwidth B_D and platform velocity v_P:

$$\Delta x = \frac{v_P}{B_D} = \frac{D_x}{2}, \tag{2.15}$$

which means that the azimuth resolution of a SAR image can be as good as half the size of the antenna. Moreover, the resolution is not range dependent.

The SAR mode presented above, with fixed antenna direction, is called *stripmap SAR*. In *spotlight SAR*, the antenna is focussed on the same point along the whole synthetic aperture, giving better spatial resolution, but lower coverage. In *scan SAR*, the antenna beam is swept, which results in better coverage than stripmap at the price of resolution. See [29, 31, 32] for more information.

2.2.2 Image Characteristics

At a first glance, SAR images may remind of the more familiar optical images. However, the two imaging methods are conceptually different. This should be taken into consideration when studying SAR images.

The first difference between SAR images and optical images is the illumination. While SAR provides its own illumination, which can be easily controlled, optical imagery in remote sensing relies on solar illumination. In this meaning, SAR imagery is more predictable and reproducible. However, SAR imagery is also prone to other types of geometric distortions. In topographic terrain, effects such as layover and foreshortening show up [29]. Both in SAR imaging and optical imaging, the effects of shadow can be seen in non-illuminated regions.

Another difference comes with the way in which images are resolved. Optical imagery features constant resolution angle in both range and azimuth direction. Far-range pixels are therefore resolved with lower resolution than the ones in the near-range. In SAR, pixels are resolved at constant slant-range resolution. When projected on the ground, pixels in far-range have better resolution than those in near-range (assuming flat earth). In azimuth, all pixels have the same resolution (provided that the bandwidth is small compared to the central frequency). See Figure 2.3(a) for a schematic explanation.

While in optical imagery, incoherent radiation is used (the phase of sunlight is random), SAR uses coherent waves. This results in an effect called *speckle*. This effect occurs when more than one scatterer is located within a resolution cell at different distances from the radar. The total reflected wave will be a coherent sum of the waves reflected from each scatterer separately. The interaction of the waves will cause interference. The intensity will vary from pixel to pixel and the phase and amplitude of the reflected radiation will be random. This phenomenon is illustrated in Figure 2.3(b). In Figure 2.4, speckle can be easily observed. One way to reduce speckle effect is by *multilooking*, that is by spatial averaging. However, multilooking degrades the resolution of the image.

Electromagnetic waves interact strongly with objects with sizes comparable to, or larger than the wavelength. For visible light, wavelengths are around 400–700 nm, while for radio waves and microwaves, wavelengths can vary between millimetres and tens or even hundreds of metres. Objects with sizes smaller than

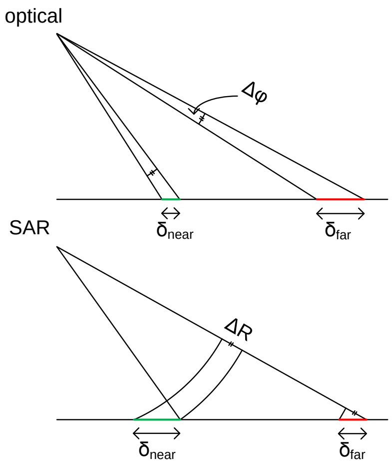

(a) Comparison of the size of the resolution cells in SAR and optical imaging under flat-earth assumption.

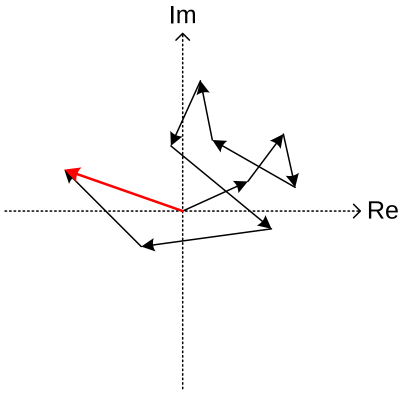

(b) The effect of speckle. Multiple scatterers within a resolution cell cause interference between the scattered waves.

Figure 2.3: Illustration of two principal differences between SAR and optical imagery.

(a) ALOS PALSAR (L-band, 14 MHz@1.3 GHz, date: 2008/08/20, mode: FBD, pol: HH, pixel size: 25 m x 25 m, approx. 7 looks/pixel, inc. angle: 34°, asc. orbit)

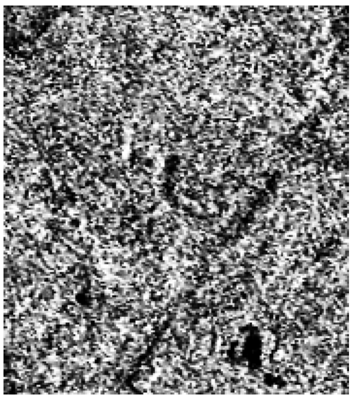

(b) RADARSAT-2 (C-band, 30 MHz@5.4 GHz, date: 2009/08/13, mode: FQ, pol: HH, pixel size: 10 m x 10 m, approx. 1.4 looks/pixel, inc. angle: 37°, desc. orbit)

(c) TerraSAR-X (X-band, 150 MHz@9.6 GHz, date: 2009/08/26, mode: HS, pol: HH, pixel size: 5 m x 5 m, approx. 11 looks/pixel, inc. angle: 34°, desc. orbit)

Figure 2.4: The same region imaged by three different satellites at three different frequencies (the first number is the bandwidth, the second number is the central frequency). The size of the imaged area is 1.78 km x 2.00 km Note: for ALOS PALSAR, no suitable image was available for the same date and orbit type. The shown image comes from the same season, a year earlier than for the two other satellites. Also, the image was acquired in ascending orbit, which means that the acquisition was made from the opposite direction.

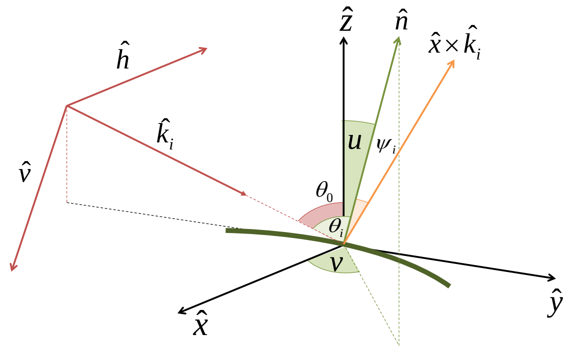

Figure 2.5: Basic geometry of scattering. $\hat{\mathbf{n}}$ is the ground surface normal. $\hat{\mathbf{x}} \times \hat{\mathbf{k}}_i$ is the imaging plane normal.

the wavelength are in the Rayleigh regime and interact weakly. SAR imagery can therefore "see through" objects that normally block visible light. Depending on the wavelength, different features of the imaged region can be observed. In Figure 2.4, a forested region is imaged at three different wavelengths in approximately the same conditions (23 cm for L-band, 5.6 cm for C-band, and 3.1 cm for X-band). The three images all have different resolution, but also the scattering behaviour is different. Some regions that appear bright at L-band, are dark at X-band. By imaging at different frequencies, different features of the same region can be extracted.

2.2.3 Polarimetry and Interferometry

A fully polarised EM wave propagating in the direction of $\hat{\mathbf{k}}_i$, see Figure 2.5, can be expressed as a sum of two components, one in the horizontal direction and one in the vertical direction:

$$\mathbf{E} = E_{\mathrm{H}}\hat{\mathbf{h}} + E_{\mathrm{V}}\hat{\mathbf{v}}, \tag{2.16}$$

where

$$\hat{\mathbf{h}} = \frac{\hat{\mathbf{z}} \times \hat{\mathbf{k}}_i}{|\hat{\mathbf{z}} \times \hat{\mathbf{k}}_i|}$$

is the horizontal unit vector, perpendicular both to the vertical direction and to the direction of propagation, and

$$\hat{\mathbf{v}} = \hat{\mathbf{h}} \times \hat{\mathbf{k}}_i$$

is the vertical unit vector, perpendicular to both the horizontal direction and the direction of propagation, see also Figure 2.5. Equivalently, the electric field can be written as a *Jones vector* [33]:

$$\mathbf{E} = \begin{bmatrix} E_{\mathrm{H}} \\ E_{\mathrm{V}} \end{bmatrix}. \tag{2.17}$$

Assuming plane waves, the incident electric field ($\mathbf{E}^i$) and the scattered electric field ($\mathbf{E}^s$) are now related through:

$$\mathbf{E}^s = \frac{\mathrm{e}^{ik_0R}}{R}\,[S]\,\mathbf{E}^i \tag{2.18}$$

or

$$\begin{bmatrix} E^s_{\mathrm{H}} \\ E^s_{\mathrm{V}} \end{bmatrix} = \frac{\mathrm{e}^{ik_0R}}{R} \begin{bmatrix} S_{\mathrm{HH}} & S_{\mathrm{HV}} \\ S_{\mathrm{VH}} & S_{\mathrm{VV}} \end{bmatrix} \begin{bmatrix} E^i_{\mathrm{H}} \\ E^i_{\mathrm{V}} \end{bmatrix}, \tag{2.19}$$

where R is the distance between the target and the antenna, $k_0 = 2\pi/\lambda$ is the wavenumber, and $[S]$ is the complex 2×2 *scattering matrix*. The scattering matrix fully describes scattering from the target at the governing radar setup (frequency, incident angle). For monostatic radar, $S_{\mathrm{HV}} = S_{\mathrm{VH}}$ due to reciprocity [34].

In remote sensing, most scatterers are not stable, fixed point targets, but they are distributed, dynamic targets stochastically changing in time and space. Such targets are best described using second order moments.

The scattering vector in the lexicographic basis for a SAR image is defined as [33]:

$$\underline{\mathbf{\Omega}} = \left[S_{\mathrm{HH}},\ \sqrt{2}S_{\mathrm{HV}},\ S_{\mathrm{VV}}\right]^{\mathrm{T}}, \tag{2.20}$$

where $^{\mathrm{T}}$ is the transpose operator. The factor $\sqrt{2}$ is introduced to keep the total power invariant after omitting the redundant element S_{VH}. The scattering vector is introduced to enable the use of matrix algebra in further operations.

Polarimetric SAR

If a SAR system is fully polarimetric, that is if it can measure the three elements of $\underline{\mathbf{\Omega}}$ in terms of magnitude and phase, then the *polarimetric covariance matrix* can be computed [33]:

$$[V] = \left\langle \underline{\mathbf{\Omega}} \cdot \underline{\mathbf{\Omega}}^{\mathrm{H}} \right\rangle = \begin{bmatrix} \left\langle |S_{\mathrm{HH}}|^2 \right\rangle & \sqrt{2}\left\langle S_{\mathrm{HH}} S_{\mathrm{HV}}^* \right\rangle & \left\langle S_{\mathrm{HH}} S_{\mathrm{VV}}^* \right\rangle \\ \sqrt{2}\left\langle S_{\mathrm{HV}} S_{\mathrm{HH}}^* \right\rangle & 2\left\langle |S_{\mathrm{HV}}|^2 \right\rangle & \sqrt{2}\left\langle S_{\mathrm{HV}} S_{\mathrm{VV}}^* \right\rangle \\ \left\langle S_{\mathrm{VV}} S_{\mathrm{HH}}^* \right\rangle & \sqrt{2}\left\langle S_{\mathrm{VV}} S_{\mathrm{HV}}^* \right\rangle & \left\langle |S_{\mathrm{VV}}|^2 \right\rangle \end{bmatrix}, \tag{2.21}$$

Where $^{\mathrm{H}}$ is the Hermitian (conjugate transpose) operator. Note, that the elements on the diagonal are real valued, and they represent backscatter intensities for the three polarisations. The *backscattering coefficient sigma nought* for polarisation mode PQ can be defined and expressed in terms of the diagonal elements in (2.21) using (2.3) and (2.18):

$$\sigma^0_{\mathrm{PQ}} = \frac{\langle \sigma_{\mathrm{PQ}} \rangle}{A_{GR}} = \frac{4\pi \left\langle |S_{\mathrm{PQ}}|^2 \right\rangle}{A_{GR}} = \frac{4\pi \cos\psi_i \left\langle |S_{\mathrm{PQ}}|^2 \right\rangle}{A_{SR}}, \tag{2.22}$$

where A_{SR} is the area of a resolution cell in slant range, A_{GR} is the area of a resolution cell in ground range, ψ_i is the angle between the ground surface normal and image plane normal, as defined in [35] and in Figure 2.5. The factor $\cos\psi_i$ projects the resolution cell on the ground.

Using polarimetric SAR (PolSAR) imagery, scattering mechanisms occurring in the imaged region can be studied, often using *polarimetric decompositions*. In this approach, the covariance matrix (or the similar coherency matrix) is decomposed into several matrices, each representing a certain, well defined scattering mechanism (such as direct backscatter, dihedral reflection, and random volume scattering, see Section 2.3). There are many different decomposition theorems based on different principles. Consult [33, 36] for more information.

Three civilian, spaceborne, fully polarimetric SAR systems have been launched, SIR-C/X (USA, Germany, Italy), ALOS PALSAR (Japan) and RADARSAT-2 (Canada), of which only the last one is still operational. Some fully polarimetric airborne SAR systems include: NASA/JPL AIRSAR and UAVSAR (USA), DLR ESAR (Germany), and ONERA RAMSES and SETHI (France). A description of the past and present polarimetric SAR systems can be found in [33].

Interferometric SAR

Assume that two fully polarimetric SAR images are acquired from two positions separated either by a spatial baseline $\mathbf{B}$ or a temporal baseline B_T, see Figure 2.6. The scattering vectors of the two images are $\underline{\mathbf{\Omega}}_1$ and $\underline{\mathbf{\Omega}}_2$. The *interferometric covariance matrix* for this pair is [33]:

$$[K_{12}] = \left\langle \underline{\mathbf{\Omega}}_1 \cdot \underline{\mathbf{\Omega}}_2^{\mathrm{H}} \right\rangle = \begin{bmatrix} \left\langle S^1_{\mathrm{HH}} S^{2*}_{\mathrm{HH}} \right\rangle & \sqrt{2}\left\langle S^1_{\mathrm{HH}} S^{2*}_{\mathrm{HV}} \right\rangle & \left\langle S^1_{\mathrm{HH}} S^{2*}_{\mathrm{VV}} \right\rangle \\ \sqrt{2}\left\langle S^1_{\mathrm{HV}} S^{2*}_{\mathrm{HH}} \right\rangle & 2\left\langle S^1_{\mathrm{HV}} S^{2*}_{\mathrm{HV}} \right\rangle & \sqrt{2}\left\langle S^1_{\mathrm{HV}} S^{2*}_{\mathrm{VV}} \right\rangle \\ \left\langle S^1_{\mathrm{VV}} S^{2*}_{\mathrm{HH}} \right\rangle & \sqrt{2}\left\langle S^1_{\mathrm{VV}} S^{2*}_{\mathrm{HV}} \right\rangle & \left\langle S^1_{\mathrm{VV}} S^{2*}_{\mathrm{VV}} \right\rangle \end{bmatrix}, \tag{2.23}$$

where S^i_{PQ} is the complex scattering amplitude for polarisation PQ and image i, and * is the conjugate operator. Assume also that the difference in incident angles between the two acquisitions is small (same scattering mechanisms), and that the resolution cells cover each other (same speckle effect). The elements on the diagonal of $[K_{12}]$ are called *interferograms*. Interferogram phase is an indicator of the change in distance between the two acquisitions [36]:

$$\Delta\phi = \arg\left(\left\langle S^1_{\mathrm{PQ}} \cdot S^{2*}_{\mathrm{PQ}} \right\rangle\right) = \frac{4\pi}{\lambda} \cdot \Delta R + 2\pi n, \tag{2.24}$$

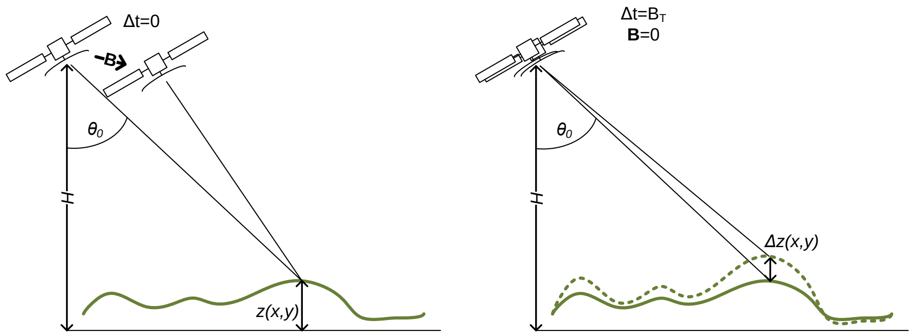

(a) Single-pass interferometry (b) Repeat-pass interferometry

Figure 2.6: Two main interferometric scenarios. Single-pass interferometry is used to measure surface height. Repeat-pass interferometry is used to measure the change in surface height. Here, Δt is the time between the acquisitions.

where ΔR is the change in distance to the scatterers between the acquisitions, and n is an integer related to the 2π phase ambiguity. The removal of this ambiguity is called *phase unwrapping*.

The *complex correlation coefficient* $\widetilde{\gamma}$ for polarisation PQ is defined as [36]:

$$\widetilde{\gamma} = \gamma e^{i\Delta\phi} = \frac{\left\langle S^1_{\mathrm{PQ}} \cdot S^{2*}_{\mathrm{PQ}} \right\rangle}{\sqrt{\left\langle \left|S^1_{\mathrm{PQ}}\right|^2 \right\rangle \left\langle \left|S^2_{\mathrm{PQ}}\right|^2 \right\rangle}} \tag{2.25}$$

where $\gamma = |\widetilde{\gamma}|$ is called *coherence*. Coherence is a real valued quantity between 0 and 1. It is a measure of the degree of similarity between the two images.

If the two acquisitions are made at the same time, but from slightly different positions, as in Figure 2.6(a), then it is possible to estimate the height of the surface $z(x, y)$, the digital surface model, from ΔR. This interferometric approach is called *single-pass interferometry*. It is most often used to create digital elevation models (DEMs), like the SRTM (USA) [37] and TanDEM-X (Germany) [38] missions.

If the two acquisitions are made at different times, but from the same positions, as in Figure 2.6(b), then it is possible to estimate the change of the surface $\Delta z(x, y)$ from ΔR. This is called *repeat-pass interferometry*. It is most often used to track topographic changes due to earthquakes and volcanoes. The ERS-1/2 (ESA) [39] mission and the new satellite constellation COSMO-SkyMed (Italy) [40] are good examples of satellite systems designed for repeat-pass interferometry[3].

Extended Covariance Matrix

The *extended covariance matrix* for the two images 1 and 2 is defined as:

$$[C_6] = \begin{bmatrix} \left\langle \underline{\mathbf{\Omega}}_1 \underline{\mathbf{\Omega}}_1^{\mathrm{H}} \right\rangle & \left\langle \underline{\mathbf{\Omega}}_1 \underline{\mathbf{\Omega}}_2^{\mathrm{H}} \right\rangle \\ \left\langle \underline{\mathbf{\Omega}}_2 \underline{\mathbf{\Omega}}_1^{\mathrm{H}} \right\rangle & \left\langle \underline{\mathbf{\Omega}}_2 \underline{\mathbf{\Omega}}_2^{\mathrm{H}} \right\rangle \end{bmatrix} = \begin{bmatrix} V_{11} & K_{12} \\ K_{12}^{\mathrm{H}} & V_{22} \end{bmatrix}, \tag{2.26}$$

where $[V_{11}]$ and $[V_{22}]$ are polarimetric covariance matrices for image 1 and 2 respectively, as defined in (2.21), and $[K_{12}]$ is as defined in (2.23).

[3]ERS-1/2 and COSMO-SkyMed are two systems consisting of more than one satellite designed for repeat-pass interferometry. However, two acquisitions from one satellite can also be used. In that meaning, almost all satellite systems are suitable for repeat-pass interferometry. However, the time between acquisitions can be too high to be able to extract valuable information.

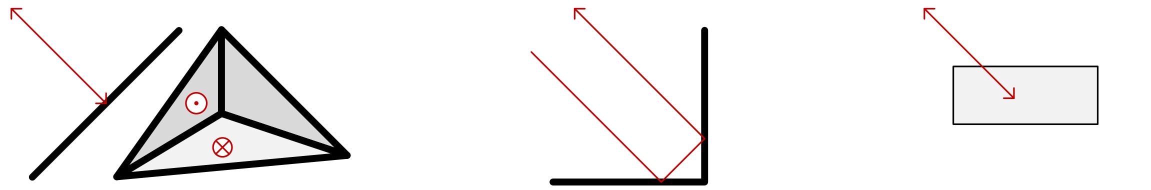

Figure 2.7: Illustration of the three basic scattering mechanisms.

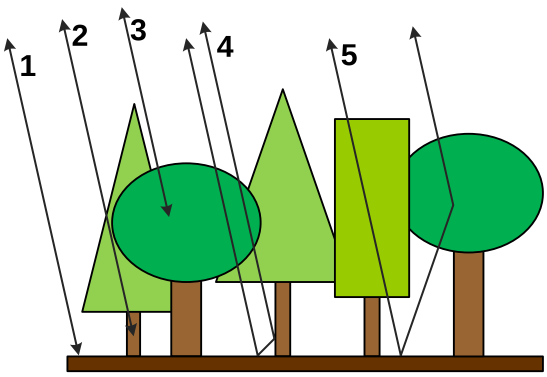

Figure 2.8: Basic scattering mechanisms for forests. 1: Direct backscatter from the ground. 2: Direct backscatter from the trunk. 3: Direct backscatter from the crown. 4: Ground-trunk or trunk-ground backscatter. 5: Ground-crown or crown-ground backscatter.

2.3 Radar Scattering

Basic Mechanisms

Electromagnetic waves can be scattered from objects in many different ways. The three most commonly distinguished scattering mechanisms are:

- single or odd-bounce scattering (e.g. scattering from a plane surface or from a trihedral corner reflector),
- double or even-bounce scattering (e.g. scattering from a dihedral reflector),
- direct backscatter from a volume of randomly oriented particles,

see also Figure 2.7. Each mechanism has different polarisation characteristics. For a metallic plate or a trihedral corner reflector oriented towards the incident electromagnetic field, scattering occurs in the same way for both horizontally and vertically polarised waves. No depolarisation occurs. For a horizontally oriented metallic dihedral, a phase shift of $180°$ is introduced between the vertical and horizontal polarisation, but no depolarisation occurs either. For a volume of randomly oriented particles, scattering occurs at different positions, and the scattered wave is incoherent. Moreover, strong depolarisation can be observed. Consult [33, 34] for more information on this topic.

Scattering from Forests

Radar scattering from forests is in general a complicated process. Forests are multi-scale targets, inhomogeneous in terms of structure and dielectric properties. As mentioned earlier, scattering characteristics are dependent on radar frequency. At lower frequencies, it is sufficient to only consider the large-scale elements, such as tree stems, tree crowns, and the ground. However, at high frequencies, all elements such as leaves, needles, small branches, bark, and understorey vegetation contribute to scattering, making it more difficult to understand and model.

Nevertheless, a basic forest model consisting of the three elements ground, trunk, and crown can in many cases be sufficient. Using such simplified model, scattering from forests can be divided into five basic mechanisms [9]:

1. direct backscatter from the ground,
2. direct backscatter from the trunk,
3. direct backscatter from the crown,
4. ground-trunk or trunk-ground backscatter,
5. crown-ground or ground-crown backscatter,

see also Figure 2.8. Higher order scattering effects and multipath effects are less significant. Note, that the relation of the five mechanisms described above to the basic mechanisms presented in Section 2.3 is not always clear. For example, crown-ground backscatter may consist both of a dihedral reflection and volume scattering.

Using polarimetric decomposition theorems, the contribution of each basic scattering mechanism to the total backscattered field can be studied [33]. In Figure 2.9, *Pauli decomposition* is used to illustrate differences between P- and L-band SAR. Even-bounce scattering (mostly dihedral reflection) is shown in red, odd-bounce scattering (mostly direct backscatter and trihedral reflection) is shown in blue, and volume scattering is shown in green. Note, that Pauli decomposition is an approximative method for scattering mechanism discrimination. All conclusions should be made with care.

To illustrate the different scattering mechanisms, seven areas have been pointed out in Figure 2.9:

- A is a lake, and backscatter is very low in both P- and L-band, since all incident waves are reflected specularly away from the radar.
- B indicates a trihedral corner reflector, which gives a high intensity in the blue channel. Scattering from a trihedral is a triple-bounce effect, and therefore an odd scattering mechanism. Scattering at L-band is also stronger due to shorter wavelength/larger relative size of the reflector.
- C is a building consisting of two parts perpendicular to each other, and together with the ground, a trihedral is created. Also here, scattering is stronger at L-band.
- D is a building which together with ground creates a dihedral reflector, resulting in a high intensity in the red channel.
- E is a clear-cut where some trees were left for seeding. These trees can be clearly seen as lighter dots. The surface in a clear-cut is rough, and thus some direct backscatter can be seen in the blue channel. This backscatter is stronger at L-band because the roughness is more visible for shorter wavelengths.
- F is a forest, in which P-band SAR penetrates deeper. More double-bounce (trunk-ground or ground-trunk) backscatter can be seen in this region at P-band (more red colour). Also, less shadowing is visible in P-band due to smaller differences in height and better penetration at lower frequencies.
- G is partially a lake, but there is also some vegetation. P-band does not "see" the same structures as L-band.

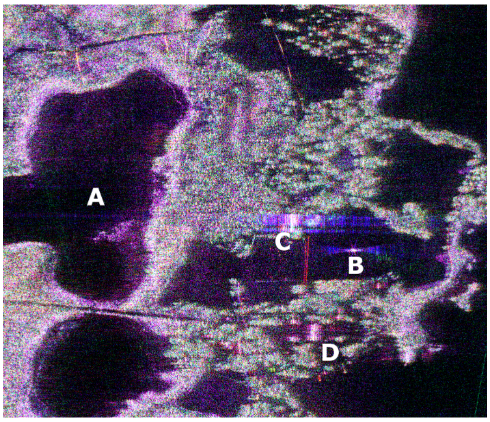

(a) Lakes and houses at the Remningstorp estate at P-band (200 MHz@360 MHz, res: 0.66 m in slant range, 0.75 in azimuth).

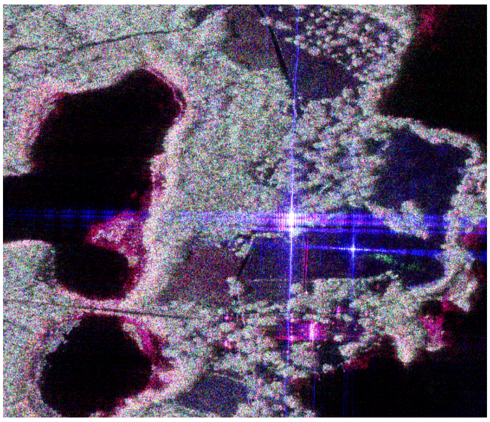

(b) Lakes and houses at the Remningstorp estate at L-band (150 MHz@1.3 GHz, res: 0.89 m in slant range, 0.89 in azimuth).

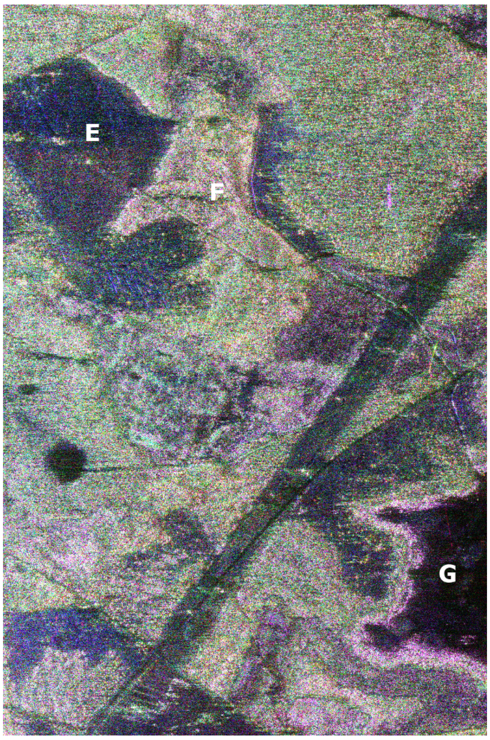

(c) Forested regions and clear-cuts at P-band (200 MHz@360 MHz, res: 0.66 m in slant range, 0.75 in azimuth).

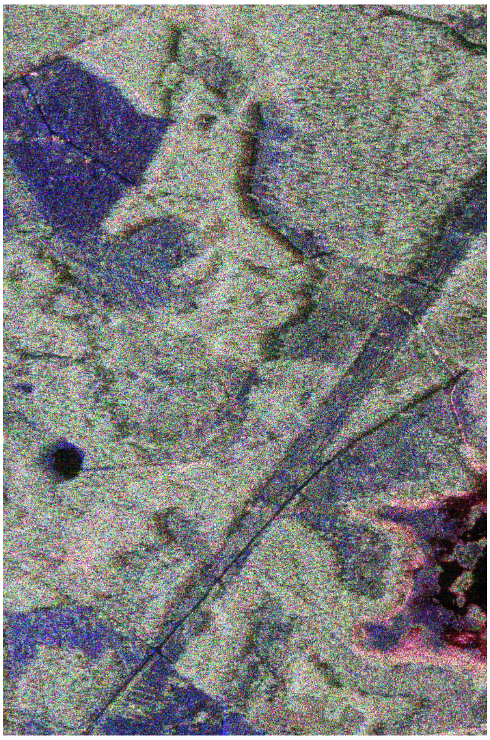

(d) Forested regions and clear-cuts at L-band (150 MHz@1.3 GHz, res: 0.89 m in slant range, 0.89 in azimuth).

Figure 2.9: Comparison between P- and L-band SETHI images of Remningstorp from the BioSAR 2010 campaign [41, 42]. The pixel size is 1 m x 1 m. The nominal angle of incidence is around 57° for images (a) and (b) and around 45° for images (c) and (d). Colour composite images based on Pauli decomposition are shown here. Legend: HH−VV (mostly dihedral scattering), HV (mostly volume scattering), HH+VV (mostly direct backscatter and trihedral scattering). Note: histograms are matched for (a) and (b), and for (c) and (d), but the colour coding was chosen for best visual effect. The images should only be analysed qualitatively. Seven smaller areas discussed in the text are also marked in the P-band images.

Chapter 3

Summary of Appended Papers

In this chapter, the five papers appended to this thesis are summarised.

3.1 Paper A: Biomass Retrieval from P-band SAR Backscatter

In this paper, a new biomass retrieval model for boreal forest using polarimetric P-band SAR backscatter is presented. The model is based on two main SAR quantities: the HV backscatter gamma nought and the HH/VV backscatter ratio. It also includes a topographic correction based on the ground slope. The model is developed from analysis of stand-wise data from two airborne P-band SAR campaigns: BioSAR 2007 [43] (test site: Remningstorp, southern Sweden, stand-wise biomass range: 10–287 tons/ha slope range: 0–4°) and BioSAR 2008 [44] (test site: Krycklan, northern Sweden, stand-wise biomass range: 8–257 tons/ha, slope range: 0–19°). The new model is compared to five other models in a set of tests to evaluate its performance in different conditions.

All models are first tested on data sets from Remningstorp with different moisture conditions, acquired during three periods in the spring of 2007. Thereafter, the models are tested in topographic terrain using SAR data acquired for different flight headings in Krycklan. The models are also evaluated across sites, i.e. training on one site followed by validation on the other site. Using the new model with parameters estimated on Krycklan data, biomass in Remningstorp is retrieved with RMSE of 40–59 tons/ha, or 22–32 % of the mean biomass, which is lower compared to the other models. In the inverse scenario, the examined site is not well represented in the training data set and the results are therefore not conclusive. Biomass maps for Remningstorp and Krycklan are created using the new model, and compared to reference maps based on lidar scanning. The differences are pointed out and explained based on basic physics of scattering and observed conditions at the site.

Major part of the work presented in this paper was done within the feasibility study for the ESA BIOMASS mission.

3.2 Papers B, C, and D: Modelling of P-band SAR Data of Forests

In Paper B, a forward model for extended covariance matrix prediction for hemi-boreal and boreal forest in P-band SAR is presented. The main product is the extended covariance matrix scaled to sigma nought on the diagonal. The input parameters consist of basic radar setup, topography, forest biome, biomass, and some model parameters. Backscatter intensities for HH, VV, and HV channels are predicted from biomass using regression based on BioSAR 2007 campaign data. The phase of the correlation between the HH and VV channels is found to be proportional to biomass and is also modelled by a regression based on BioSAR 2007 data. The coherence of HH and VV channels is found to be unrelated to biomass and is chosen to be modelled as a stochastic variable. The correlation of any co-polarised channel with HV is set to 0. The interferometric correlation values for the three channels are modelled using volume over ground (VoG) model, which is a combination of random volume over ground (RVoG), oriented volume over ground (OVoG), and elevated random volume over ground (ERVoG) models.

The forward model is also evaluated against SAR data from the BioSAR 2007 campaign [44]. Three intensity images and one complex polarimetric correlation image are created for Remningstorp (site of BioSAR 2007) from existing biomass map, DEM, and flight path information. These images are compared with the images acquired with ESAR during the BioSAR 2007 campaign and the similarities and differences are discussed. The presented forward model is able to predict backscatter with an RMSE of 1.4 dB (HV), 1.8 dB (VV), and 1.9 dB (HH). Polarimetric correlation can be predicted with magnitude and phase RMSE equal to 0.1 and 16°, respectively. A qualitative evaluation of the interferometric part is also done and it is concluded that a good setup of model parameters is necessary to get satisfactory results.

In Paper C, the forward model from Paper B is revised. Interferometric modelling is improved by the inclusion of suitable ground-to-volume ratios in the RVoG model. The ground-to-volume ratios are computed using the generalised Freeman-Durden polarimetric decomposition.

In Paper D, a tropical scenario is added to the forward model from Papers B and C. The tropical scenario is based on analysis of the data from the TropiSAR 2009 campaign [45].

The work presented in these papers was done within the feasibility study for the ESA BIOMASS mission. The forward model was integrated into the scene generation module, which was a part of the BIOMASS End-to-End Simulator [46].

3.3 Paper E: Detection of Wind-Thrown Forest and Clear-Cuts with L-, C-, and X-band SAR

A controlled experiment simulating wind-thrown forest was carried out at a hemi-boreal test site in Sweden. The simulation was done by manual felling of trees in September 2009. The trees were left on the ground until November 2009 to ensure image acquisitions after the simulated storm. SAR data from the satellites TerraSAR-X (X-band), RADARSAT-2 (C-band), and ALOS PALSAR (L-band) were acquired before, during and after this period. The backscatter signatures were analysed to evaluate possibilities to detect wind-thrown forest and clear-cuts. TerraSAR-X HH-polarised backscatter showed a significant increase when the trees were felled and the difference to selected reference forest stands was 1.2 dB to 2.0 dB. The corresponding differences for RADARSAT-2 were 0.2 dB to 1.2 dB for HH-polarisation and 0.1 to 1.1 dB for HV-polarisation. When the trees were felled, the ALOS PALSAR backscatter decreased to 1.6 dB below the reference forest for HH-polarisation and 0.4 dB to 0.8 dB for HV-polarisation. Shadowing effects in fine resolution TerraSAR-X and RADARSAT-2 data showed a high potential for detection of wind-throw with separation to the reference forest backscatter of between 4.9 dB and 9.2 dB. For clear-cut detection ALOS PALSAR proved to give the most suitable data.

Chapter 4

Conclusions and Future Work

4.1 Conclusions

The main scope of the work described in this thesis was to develop algorithms for extraction of valuable information from SAR data. As shown in Paper A, biomass could be extracted from airborne SAR with good results using an algorithm fitted to data from a different test site. By using two separate test sites, the robustness of the algorithm was tested. The use of the HH/VV-ratio together with the surface slope angle made the model significantly more stable compared to the other models.

In Papers B, C, and D, interferometric and polarimetric P-band SAR modelling for boreal and tropical forests was studied. Extended covariance matrix was predicted from a few parameters such as biomass, forest height, and the basic radar setup. The presented model was used to synthesise SAR images from biomass and height maps, and it showed good results.

In Paper E, SAR data from three satellites were used to evaluate the possibilities of storm damage and clear cut detection from space at different frequencies. A consistent change in backscatter could be observed at X-band when the threes were felled, possibly due to more specular reflections from the trunk. Also, when the trees were removed, a consistent change in backscatter could be observed at L-band. The study showed, that there are detectable changes at both X- and L-band.

4.2 Future work

Retrieval of forest biomass using P-band SAR should be further studied. Recently collected data from the BioSAR 2010 campaign, acquired in September 2010 in Remningstorp by the SETHI-platform should be studied together with the data from the first two BioSAR campaigns. Also, the algorithm should be studied on data from tropical forests, such as from the TropiSAR 2009 campaign conducted in French Guyana. A further development of the presented algorithm is desired. Inclusion of the slope aspect angle is a first step, but also the addition of some relevant polarimetric and interferometric indicators should be considered.

Modelling of the extended covariance matrix at P-band should be improved by the inclusion of topographic and temporal influence. The modelling of ground-to-volume ratios should be examined on more data. An extension of the low-frequency physical optics model presented in [47] for fully polarimetric data is also planned. This would not only aid forward modelling, but also improve the knowledge necessary for correct compensation of topographic effects in biomass retrieval models.

The study of storm damage and clear cut detection should be extended to polarimetry and/or interferometry. Also, an examination of both ascending and descending orbits, incident angles, and polarisations should be done in the future.

References

[1] World Wide Fund for Nature (WWF). (2012) Forests, jungles, woods & their trees. [Online, viewed 01 April 2012]. Available: http://wwf.panda.org/about_our_earth/about_forests/.

[2] IPCC, *Climate Change 2007: Mitigation of Climate Change. Contribution of Working Group III to the Fourth Assessment Report of the Intergovernmental Panel on Climate Change*, B. Metz, O. R. Davidson, P. R. Bosch, R. Dave, and L. A. Meyer, Eds. Cambridge, United Kingdom and New York, NY, USA: Cambridge University Press, 2007.

[3] P. Tans and R. Keeling. (2012) Trends in atmospheric carbon dioxide. [Online, viewed 29 March 2012]. Available: http://www.esrl.noaa.gov/gmd/ccgg/trends/.

[4] IPCC, *Climate Change 2007: The Physical Science Basis. Contribution of Working Group I to the Fourth Assessment Report of the Intergovernmental Panel on Climate Change*, S. Solomon, M. M. Dahe Qin, M. Marquis, K. Averyt, M. M. B. Tignor, and H. L. Miller, Eds. Cambridge, United Kingdom and New York, NY, USA: Cambridge University Press, 2007.

[5] C. Parker, A. Mitchell, M. Trivedi, and N. Mardas, *The Little REDD Book: A guide to governmental and non-governmental proposals for reducing emissions from deforestation and degradation.* Global Canopy Programme, John Krebs Field Station, Oxford OX2 8QJ, UK, November 2008.

[6] "Candidate Earth Explorer Core Mission: BIOMASS, Report for Assessment," European Space Agency (SP-1212/2), Tech. Rep., 2008.

[7] E. Næsset, T. Gobakken, S. Solberg, T. G. Gregoire, R. Nelson, G. Ståhl, and D. Weydahl, "Model-assisted regional forest biomass estimation using LiDAR and InSAR as auxiliary data: A case study from a boreal forest area," *Remote Sensing of Environment*, vol. 115, no. 12, pp. 3599–3614, 2011.

[8] T. Le Toan, A. Beaudoin, J. Riom, and D. Guyon, "Relating Forest Biomass to SAR Data," *IEEE Transactions on Geoscience and Remote Sensing*, vol. 30, no. 2, pp. 403–411, 1992.

[9] A. Beaudoin, T. L. Le Toan, S. Goze, E. Nezry, A. Lopes, E. Mougin, C. C. Hsu, H. C. Han, J. A. Kong, and R. T. Shin, "Retrieval of Forest Biomass from SAR Data," *International Journal of Remote Sensing*, vol. 15, no. 14, pp. 2777–2796, 1994.

[10] H. Israelsson, J. Askne, and R. Sylvander, "Potential of SAR for forest bole volume estimation," *International Journal of Remote Sensing*, vol. 15, no. 14, pp. 2809–2826, 1994.

[11] K. J. Ranson and G. Sun, "Mapping biomass of a northern forest using multifrequency SAR data," *IEEE Transactions on Geoscience and Remote Sensing*, vol. 32, no. 2, pp. 388–396, 1994.

[12] Y. Rauste, T. Häma, J. P. ans K. Heiska, and M. Hallikainen, "Radar-based forest biomass estimation," *International Journal of Remote Sensing*, vol. 15, pp. 1797–2808, 1994.

[13] M. L. Imhoff, "Radar backscatter and biomass saturation: ramifications for global biomass inventory," *IEEE Transactions on Geoscience and Remote Sensing*, vol. 33, no. 2, pp. 511–518, 1995.

[14] E. J. Rignot, R. Zimmermann, and J. J. van Zyl, "Spaceborne Applications of P Band Imaging Radars for Measuring Forest Biomass," *IEEE Transactions on Geoscience and Remote Sensing*, vol. 33, no. 5, pp. 1162–1169, 1995.

[15] D. H. Hoekman and M. J. Quiñones, "Land cover type and biomass classification using AirSAR data for evaluation of monitoring scenarios in the Colombian Amazon," *IEEE Transactions on Geoscience and Remote Sensing*, vol. 38, no. 2, pp. 685–696, 2000.

[16] S. Saatchi, K. Halligan, D. Despain, and R. Crabtree, "Estimation of Forest Fuel Load from Radar Remote Sensing," *IEEE Transactions on Geoscience and Remote Sensing*, vol. 45, pp. 1726–1740, 2007.

[17] G. Sandberg, L. M. H. Ulander, J. E. S. Fransson, J. Holmgren, and T. Le Toan, "L- and P-band backscatter intensity for biomass retrieval in hemiboreal forest," *Remote Sensing of Environment*, vol. 115, no. 11, pp. 2874–2886, 2011.

[18] S. Saatchi, M. Marlier, R. L. Chazdon, D. B. Clark, and A. E. Russell, "Impact of spatial variability of tropical forest structure on radar estimation of aboveground biomass," *Remote Sensing of Environment*, vol. 115, no. 11, pp. 2836–2849, 2011.

[19] T. Le Toan, S. Quegan, M. W. J. Davidson, H. Balzter, P. Paillou, K. Papathanassiou, S. Plummer, F. Rocca, S. Saatchi, H. Shugart, and L. Ulander, "The BIOMASS mission: Mapping global forest biomass to better understand the terrestrial carbon cycle," *Remote Sensing of Environment*, vol. 115, no. 11, pp. 2850–2860, 2011.

[20] M. J. Soja, G. Sandberg, and L. M. H. Ulander, "Biomass Retrieval for Boreal Forests in Sloping Terrain using P-band SAR Backscatter," Submitted to IEEE Transactions on Geoscience and Remote Sensing, February 2012.

[21] K. Folkesson, G. Smith-Jonforsen, and L. M. H. Ulander, "Model-Based Compensation of Topographic Effects for Improved Stem-Volume Retrieval From CARABAS-II VHF-Band SAR Images," *IEEE Transactions on Geoscience and Remote Sensing*, vol. 47, no. 4, pp. 1045–1055, April 2009.

[22] M. Moghaddam, Y. Rahmat-Samii, E. Rodriguez, D. Entekhabi, J. Hoffman, D. Moller, L. E. Pierce, S. Saatchi, and M. Thomson, "Microwave Observatory of Subcanopy and Subsurface (MOSS): A Mission Concept for Global Deep Soil Moisture Observations," *IEEE Transactions on Geoscience and Remote Sensing*, vol. 45, no. 8, pp. 2630–2643, August 2007.

[23] K. Scipal, M. Arcioni, J. Chave, J. Dall, F. Fois, T. Le Toan, C. Lin, K. Papathanassiou, S. Quegan, F. Rocca, S. Saatchi, H. Shugart, L. Ulander, and M. Williams, "The BIOMASS mission – An ESA Earth Explorer candidate to measure the BIOMASS of the Earth's forests," in *IEEE International Geoscience and Remote Sensing Symposium (IGARSS)*, Honolulu, HI, USA, July 2010, pp. 52–55.

[24] M. Arcioni, P. Bensi, J.-L. Bézy, B. Carnicero, M. Davidson, M. Drinkwater, F. Fois, A. Gabriele, R. Haagmans, F. Hélière, P. Ingmann, V. Kangas, M. Kern, S. Kraft, J. Langen, A. Lecuyot, C.-C. Lin, R. Meynart, K. Scipal, and P. Silvestrin, "Biomass, CoReH2O, PREMIER: ESA's candidate 7th Earth Explorer Missions," in *IEEE International Geoscience and Remote Sensing Symposium (IGARSS)*, Honolulu, HI, USA, July 2010, pp. 673–676.

[25] M. I. Skolnik, *Radar Handbook*, 2nd ed. McGraw-Hill, 1990.

[26] S. Kingsley and S. Quegan, *Understanding Radar Systems.* McGraw-Hill, 1992.

[27] W. G. Rees, *Physical Principles of Remote Sensing*, 2nd ed. Cambridge University Press, 2001.

[28] "IEEE Standard Letter Designations for Radar-Frequency Bands," *IEEE Std 521-2002 (Revision of IEEE Std 521-1984)*, 2003.

[29] R. J. Sullivan, *Radar Foundations for Imaging and Advanced Concepts.* Scitech Publishing, 2004.

[30] C. Oliver and S. Quegan, *Understanding Synthetic Aperture Radar Images.* Artech House, 1998.

[31] W. G. Carrara, R. S. Goodman, and R. M. Majewski, *Spotlight Synthetic Aperture Radar: Signal Processing Algorithms.* Artech House, 1995.

[32] I. G. Cumming and F. H. Wong, *Digital Processing of Synthetic Aperture Radar Data: Algorithms and Implementation.* Artech House, 2005.

[33] J.-S. Lee and E. Pottier, *Polarimetric Radar Imaging: From Basics to Applications.* CRC Press, 2009.

[34] F. T. Ulaby, C. Elachi, Y. Kuga, K. C. McDonald, K. Sarabandi, T. B. A. Senior, J. J. van Zyl, M. W. Whitt, and H. A. Zebker, *Radar Polarimetry for Geoscience Applications*, F. T. Ulaby and C. Elachi, Eds. Artech House, 1990.

[35] L. M. H. Ulander, "Radiometric Slope Correction of Synthetic Aperture Radar Images," *IEEE Transactions on Geoscience and Remote Sensing*, vol. 34, no. 5, pp. 1115–1122, 1996.

[36] S. R. Cloude, *Polarisation Applications in Remote Sensing.* Oxford University Press, 2010.

[37] T. G. Farr, P. A. Rosen, E. Caro, R. Crippen, R. Duren, S. Hensley, M. Kobrick, M. Paller, E. Rodriguez, L. Roth, D. Seal, S. Shaffer, J. Shimada, J. Umland, M. Werner, M. Oskin, D. Burbank, and D. Alsdorf, "The Shuttle Radar Tomography Mission," *Reviews of Geophysics*, vol. 45, 2007.

[38] M. Rodriguez-Cassola, P. Prats, D. Schulze, N. Tous-Ramon, U. Steinbrecher, L. Marotti, M. Nannini, M. Younis, P. Lopez-Dekker, M. Zink, A. Reigber, G. Krieger, and A. Moreira, "First Bistatic Spaceborne SAR Experiments With TanDEM-X," *IEEE Geoscience and Remote Sensing Letters*, vol. 9, no. 1, pp. 33–37, January 2012.

[39] E. Attema, G. Duchossois, and G. Kohlhammer, "ERS-1/2 SAR land applications: overview and main results," in *IEEE International Geoscience and Remote Sensing Symposium (IGARSS)*, Seattle, WA, USA, July 1998, pp. 1796–1798.

[40] A. Torre and P. Capece, "COSMO-SkyMed: The advanced SAR instrument," in *5th International Conference on Recent Advances in Space Technologies (RAST), 2011*, June 2011, pp. 865–868.

[41] L. M. H. Ulander, A. Gustavsson, P. Dubois-Fernandez, X. Depuis, J. E. S. Fransson, J. Holmgren, J. Wallerman, L. E. B. Eriksson, G. Sandberg, and M. J. Soja, "BioSAR 2010 - A SAR Campaign in Support to the BIOMASS Mission," in *IEEE International Geoscience and Remote Sensing Symposium (IGARSS)*, Vancouver, BC, Canada, July 2011, pp. 1528–1531.

[42] L. M. H. Ulander, A. Gustavsson, B. Flood, D. Murdin, P. Dubois-Fernandez, X. Depuis, G. Sandberg, M. J. Soja, L. E. B. Eriksson, J. E. S. Fransson, J. Holmgren, and J. Wallerman, "BioSAR 2010 Technical Assistance for the Development of Airborne SAR and Geophysical Measurements during the BioSAR 2010 Experiment: Final Report," ESA contract no. 4000102285/10/NL/JA/ef, Tech. Rep., 2011.

[43] I. Hajnsek, R. Scheiber, L. Ulander, A. Gustavsson, G. Sandberg, S. Tebaldini, A. M. Guarnieri, F. Rocca, F. Bombardini, and M. Pardini, "BioSAR 2007 technical assistance for the development of airborne SAR and geophysical measurements during the BioSAR 2007 experiment: Final report without synthesis," ESA contract no. 20755/07/NL/CB, Tech. Rep., 2008.

[44] I. Hajnsek, R. Scheiber, M. Keller, R. Horn, S. Lee, L. M. H. Ulander, A. Gustavsson, G. Sandberg, T. Le Toan, S. Tebaldini, A. M. Guarnieri, and F. Rocca, "BioSAR 2008 Technical Assistance for the Development of Airborne SAR and Geophysical Measurements during the BioSAR 2008 Experiment: Final Report - BioSAR Campaign," ESA contract no. 22052/08/NL/CT, Tech. Rep., 2009.

[45] P. Dubois-Fernandez, T. Le Toan, J. Chave, L. Blanc, S. Daniel, H. Oriot, A. Arnaubec, M. Rejou-Mechain, L. Villard, Y. Lasne, and T. Koleck, "TropiSAR 2009: Technical Assistance for the Development of Airborne SAR and Geophysical Measurements during the TropiSAR 2009 Experiment: Final Report," ESA contract no. 22446/09, CNES contract no. 9292903/08/09, Tech. Rep., 2011.

[46] P. Lopez-Dekker, F. De Zan, T. Borner, M. Younis, K. Papathanassiou, T. Guardabrazo, V. Bourlon, S. Ramongassie, N. Taveneau, L. Ulander, D. Murdin, N. Rogers, S. Quegan, and R. Franco, "BIOMASS end-to-end mission performance simulator," in *IEEE International Geoscience and Remote Sensing Symposium (IGARSS), Vancouver, BC, Canada*, July 2011, pp. 4249–4252.

[47] B. Hallberg, G. Smith-Jonforsen, L. M. H. Ulander, and G. Sandberg, "A physical-optics model for double-bounce scattering from tree stems standing on an undulating ground surface," *IEEE Transactions on Geoscience and Remote Sensing*, vol. 46, no. 9, pp. 2607–2621, 2008.

Paper A

Biomass Retrieval for Boreal Forests using P-band SAR Backscatter

Authors:

M. J. Soja, G. Sandberg, and L. M. H. Ulander

Status:

Submitted to *IEEE Transactions on Geoscience and Remote Sensing*, February 2012

Biomass Retrieval for Boreal Forests in Sloping Terrain using P-band SAR Backscatter

Maciej Jerzy Soja, Gustaf Sandberg, and Lars M. H. Ulander, *Senior Member, IEEE*

Abstract

A new biomass retrieval model for boreal forest using polarimetric P-band SAR backscatter is presented. The model is based on two main SAR quantities: the HV backscatter and the HH/VV backscatter ratio. It also includes a topographic correction based on the ground slope. The model is developed from analysis of stand-wise data from two airborne P-band SAR campaigns: BioSAR 2007 (test site: Remningstorp, southern Sweden, biomass range: 10–287 tons/ha, slope range: 0–4°) and BioSAR 2008 (test site: Krycklan, northern Sweden, biomass range: 8–257 tons/ha, slope range: 0–19°). The new model is compared to five other models in a set of tests to evaluate its performance in different conditions.

All models are first tested on data sets from Remningstorp with different moisture conditions, acquired during three periods in the spring of 2007. Thereafter, the models are tested in topographic terrain using SAR data acquired for different flight headings in Krycklan. The models are also evaluated across sites, i.e. training on one site followed by validation on the other site. Using the new model with parameters estimated on Krycklan data, biomass in Remningstorp is retrieved with RMSE of 40–59 tons/ha, or 22–32 % of the mean biomass, which is lower compared to the other models. In the inverse scenario, the examined site is not well represented in the training data set and the results are therefore not conclusive.

Index Terms

Biomass retrieval, boreal forest, P-band, synthetic aperture radar (SAR), topographic correction

I. Introduction

Facing the threat of global warming one of the most important topics in climate research is understanding the terrestrial carbon cycle and predicting future climate changes. One of the major uncertainties in the current carbon cycle models lies in terrestrial ecosystems, in particular forests [1]. Moreover, up to 20 % of the global emissions of carbon dioxide are estimated to come from deforestation [2]. Accurate, global-scale forest mapping is therefore

M. J. Soja, G. Sandberg and L. M. H. Ulander are with the Department of Earth and Space Sciences, Chalmers University of Technology, 412 96 Gothenburg, Sweden.

L. M. H. Ulander is also with the Radar Systems Unit, Swedish Defence Research Agency, 581 11 Linköping, Sweden.

For correspondence, please contact M. J. Soja at soja@chalmers.se

Manuscript received N/A; revised N/A. This work was supported by the Swedish National Space Board (SNSB) and the European Space Agency (ESA).

one of the most important elements of climate modelling. Current global forest maps are simply too inaccurate for this task, creating a demand for the development of new tools.

The most relevant quantity directly related to the forestal carbon stock is aboveground dry biomass (further on simply called ”biomass”). Biomass is the dry weight of aboveground forest, including stem, bark, branches, and needles/leaves, but excluding stump and roots. Biomass is usually measured in metric tons per hectare (1 ton/ha = 0.1 kg/m^2).

Currently, the most accurate technique for remote biomass mapping is small-footprint lidar scanning (see [3] and references therein). However, accurate lidar-based biomass estimation requires high-quality plot-level measurements for training. Biomass tends also to be underestimated as small trees may be covered by large trees blocking the laser beam. As with all optical methods, measurement accuracy is dependent on weather conditions. In reality, small-footprint lidar scanning is inefficient for global biomass mapping. Spaceborne lidar has been considered a possible alternative, but complications arise due to large footprint, low coverage, etc, and there are currently no ongoing spaceborne lidar missions.

Synthetic Aperture Radar (SAR) is a high-resolution, microwave imaging sensor which is weather-independent and provides its own illumination. Moreover, SAR systems can be customised to fit a particular task through the choice of imaging frequencies, incident angles, imaging modes, etc.

SAR imaging at low frequencies (here: below L-band) has proven itself especially useful for biomass mapping due to its superior penetration capabilities and sensitivity to a wide range of biomass levels. Due to transmission restrictions, there neither are, nor have been, any satellites in Earth’s orbit operating below L-band. Therefore, all low-frequency studies have been performed using data acquired with airborne platforms. The low VHF-band (20–90 MHz) SAR system CARABAS-II, run by the Swedish Defence Research Agency (FOI), has previously proven itself useful for accurate stem volume estimation (see [4] and references therein). Also, several P-band (approximately 0.20–0.45 GHz) studies have been performed using airborne SAR systems [5]–[14]. All these studies conclude that biomass and radar backscatter are correlated, but the presented functions and their regions of validity differ (due to differences in test site, biome, forest structure, acquisition platforms, surface topography, moisture conditions, etc). This means that the models derived in these papers usually have little or no application outside the studied test site. This is an obvious disadvantage when global biomass mapping is concerned.

At low frequencies, radio waves are generally scattered from larger objects such as tree trunks and primary branches. The increased temporal stability (as compared to e.g. X-band) makes it possible to perform repeat-pass polarimetric SAR interferometry (PolInSAR), which produces forest height estimates [15]–[17]. However, both PolInSAR-based height estimation and allometric height-to-biomass conversion are sensitive to parameters such as vertical structure, species composition, management procedures, etc [18]. Since it is not likely that these parameters can be estimated accurately with radar, accurate biomass estimation from PolInSAR is aggravated. Possible improvements include multi-baseline PolInSAR [19], [20] and different tomographic techniques [21]–[23]. However, these techniques require the acquisition of high-quality multi-baseline data, which is a very costly and time consuming process.

Although the temporal stability and biomass sensitivity are both improved at low frequencies, a different problem occurs instead: ground topography. The double-bounce effect (scattering between ground and trunk, or vice versa) is very prominent at low frequencies and ground tilt has an obvious influence. This issue has been addressed in [24], where a physical-optics model was successfully used to describe the influence of topography on radar backscatter from forests (at both VHF- and P-band). In [4], [25], a simplified approach based on electromagnetic models like those described in [26]–[31] was used at VHF-band to reduce topography influence, giving stem volume retrieval results comparable to those for flat ground. In this text, an even simpler approach will be used. The influence of topography will be examined as the change in model parameters for some reference models and the most prominent factors will be included.

Due to the recent opening of the P-band at frequencies 432–438 MHz for spaceborne use (World Radiocommunications Conference 2003 [32]), a fully polarimetric P-band SAR satellite system called BIOMASS has been proposed to European Space Agency (ESA) for the 7$^{\text{th}}$ Earth Explorer mission [32]–[35]. It is currently undergoing a feasibility study. The system is planned to employ both intensity-based biomass retrieval and PolInSAR-based height retrieval. The two methods show different performance in different environments and are complementary, thus extending the capability of the proposed satellite.

In this paper, a new model for biomass retrieval from polarimetric SAR backscatter is presented. The model is developed and tested for its sensitivity to site topography and for temporal change. Also, the model is compared to previously published models, and evaluated using two sets of test data. The data were acquired within two BioSAR campaigns performed in 2007 and 2008 in the two test sites Remningstorp and Krycklan, respectively, both situated in Sweden. The test sites are located 720 km apart, and represent two different cases of boreal forest. In previous papers dealing with biomass retrieval from BioSAR data, the two test sites were treated separately [13], [36]–[38]. In this paper, models fitted to data from one test site are evaluated on the other. In this manner, the model is validated independently of the training data set. An excerpt of the results presented here has been published in [39].

This paper begins with a brief description of the experimental data (Sec. II). Next, in Sec. III, the previously published models are presented and the new model is introduced. Thereafter, the models are evaluated with respect to temporal change, topographic change, and across-site retrieval (Sec. IV). The results are summarised and conclusions are drawn in Sec. V.

II. Experimental Data

The experimental data used in this paper were acquired within two BioSAR campaigns conducted by the airborne Experimental SAR (ESAR) platform from the German Aerospace Center (DLR). Ground-truth data data were collected and processed by Swedish University of Agricultural Sciences (SLU).

A. Test Sites

BioSAR 2007 was conducted in Remningstorp (58° 28’ N, 13° 38’ E) situated in southern Sweden, see Fig. 1. Remningstorp is fairly flat with ground slopes at stand level less than 5° (computed from a 50 m × 50 m digital elevation model, DEM). The test site covers approximately 1200 ha of productive forest land and the dominating

TABLE I

SUMMARY OF AVAILABLE BIOMASS REFERENCE DATA. ONLY STANDS COMPLETELY COVERED BY P-BAND SAR DATA ARE INCLUDED. **SID** STANDS FOR "SITE ID" (RE FOR REMNINGSTORP, KR FOR KRYCKLAN). **GID** STANDS FOR "GROUP ID" AND REFERS TO TYPE OF STAND-WISE DATA SET (BASED ON **MAIN DATA SOURCE**). **N** IS THE SIZE OF EACH DATA SET. **TYPE** REFERS TO THE CORRECT DENOMINATION OF THE DATA POINTS, AS IT WOULD BE REFERRED TO IN FORESTRY. **MEAN** $\mathcal{B}$ AND $\mathcal{B}$ **RNG** REFER TO THE MEAN BIOMASS AND BIOMASS RANGE FOR EACH DATA SET. **AREA** REFERS TO THE STAND AREA (OR AREA RANGE) IN HECTARES. **ERROR** REFERS TO THE ESTIMATED STANDARD BIOMASS ERROR (IF IN %, THEN RELATIVE **MEAN** $\mathcal{B}$, IF A PERCENTAGE INTERVAL, THEN DIFFERENT PERCENTAGE FOR EACH STAND RELATIVE ITS MEAN BIOMASS).

SID:	**GID:**	**N:**	**Type:**	**Main data source:**	**Mean** $\mathcal{B}$	$\mathcal{B}$ **rng:**	**Area:**	**Error:**
Re	*INS*	10	plots	plot-level measurements	185	52–267	0.66–0.69	up to 5 %
	LID	58	stands	stem volume map, species stratification info	129	10–287	0.50–9.4	25 tons/ha
Kr	*INS*	29	stands	plot-level measurements	94	23–183	1.5–22	4–21 %
	LID	97	plots	biomass map	76	8–257	0.79	16 %

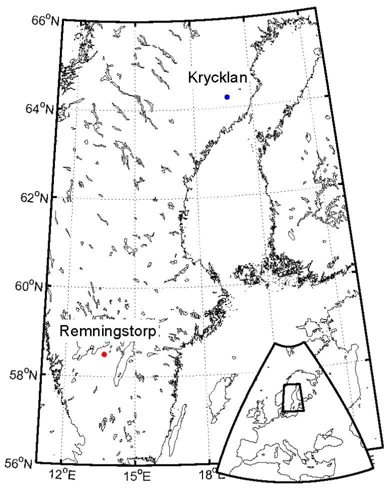

Fig. 1. The two test sites used in BioSAR 2007 and BioSAR 2008 campaigns are shown here. The test area in Remningstorp was covered by SAR imagery in the spring of 2007, whereas Krycklan was covered in October 2008. The distance between the two sites is 720 km.

species are Norway spruce (*Picea abies*), Scots pine (*Pinus sylvestris*), and birch (*Betula*). For a thorough description of the campaign, see [13], [40].

BioSAR 2008 was conducted in Krycklan (64° 14' N, 19° 46' E) located in northern Sweden, see Fig. 1. Krycklan is situated 720 km north-north-east of Remningstorp. Unlike Remningstorp, Krycklan has a strongly undulating topography with ground slopes on stand level up to 19° (again, computed from a 50 m × 50 m DEM). The forest is dominated by Norway spruce and Scots pine. For a thorough description of the campaign, see [41].

It is worth mentioning that a third BioSAR campaign has been conducted in Remningstorp in October 2010,

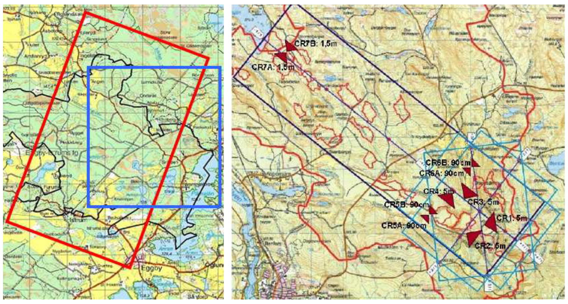

Fig. 2. Acquisitions scenarios for BioSAR 2007 (Remningstorp, left) and BioSAR 2008 (Krycklan, right). In Remningstorp, two headings were flown. In Krycklan, four distinct headings were flown.

aiming at the detection of long-term temporal changes in Remningstorp, see [42], [43]. However, data processing and analysis were not finished at the time of writing of this text and this campaign is thus not included.

In the following text, the two test sites will sometimes be referred to as Re (Remningstorp) and Kr (Krycklan).

B. In-situ and Laser Scanning Data

In conjunction with both BioSAR campaigns, plot-level *in-situ* data and airborne lidar scanning data were collected for the estimation of biomass. Species stratification information extracted from aerial photography was also used to aid biomass estimation. Biomass maps with $10\,\mathrm{m} \times 10\,\mathrm{m}$ pixels were produced for both Remningstorp and Krycklan. Slightly different data collection strategies and estimation procedures were used for the two campaigns, and campaign reports should be consulted for a thorough description [40], [41].

Table I summarises the available reference biomass data sets together with their approximate error levels and their origin. In forestry, a distinction between "plots" and "stands" is made. Stands are relatively homogenous forest regions with similar species composition, biophysical characteristics (e.g. height and tree number density), management procedures, etc. They can vary in size and shape, and they are the main unit used for forest mapping and management [44]. Plots are usually smaller stand subsets of regular shape, which are used as within-stand samples. They are usually distributed in a regular pattern.

In Table I, the four reference data sets used in this text are presented. All data sets except the 97 plots in Krycklan are thoroughly described in their corresponding campaign reports [40], [41]. The 97 plots in Krycklan have been introduced in [37]. These plots are circular with a radius of 50 m, and their biomass was obtained from the lidar-derived biomass map. They were selected to minimise within-stand deviations from a constant slope, and they were required to be covered by all four flight headings (see Sec. II-C and Fig. 2). The error levels presented in Table I have already been described for both data sets in Remningstorp in [13]. For the 29 stands in Krycklan, the errors were computed based on the number of plots within each stand and the variation between these plots within each stand [41], [45]. For the 97 plots in Krycklan, the error is estimated to be equal to the error of the corresponding biomass map, for which it was computed by cross-validation against the previously mentioned 29 stands, see page 20 in [41].

TABLE II

SUMMARY OF AVAILABLE STAND-WISE SAR DATA. **SID** STANDS FOR "SITE ID" (RE FOR REMNINGSTORP, KR FOR KRYCKLAN). **DID** STANDS FOR "DATE ID" AND REFERS TO THE ACQUISITION DATE. **DIR** IS THE AVERAGE FLIGHT HEADING RELATIVE NORTH. **N** IS THE NUMBER OF GEOCODED IMAGES FOR THE GIVEN SITE-DATE-HEADING SETUP. **GID** STANDS FOR "GROUP ID" AND REFERS TO TYPE OF STAND-WISE DATA SET (ACCORDING TO TABLE I). **CN** REFERS TO THE NUMBER OF STANDS REPRESENTED IN EACH DATA SET (OF TOTAL **TN**). IF MORE THAN ONE IMAGE IS AVAILABLE, CORRESPONDING NUMBERS ARE SEPARATED BY COMMAS. $\mathcal{B}$ **RNG** REFERS TO THE AVAILABLE BIOMASS RANGE (IN TONS/HA).

SID:	**DID:**	**Dir:**	**N:**	**GID:**	**CN of TN:**	$\mathcal{B}$ **rng**:
Re	Mar	179°	1	INS	9 of 10	52–267
				LID	46 of 58	10–287
		200°	2	INS	10, 10 of 10	52–267
				LID	58, 58 of 58	10–287
	Apr	179°	1	INS	9 of 10	52–267
				LID	46 of 58	10–287
		200°	2	INS	10, 10 of 10	52–267
				LID	58, 58 of 58	10–287
	May	179°	1	INS	9 of 10	52–267
				LID	46 of 58	10–287
		200°	2	INS	10, 10 of 10	52–267
				LID	58, 58 of 58	10–287
Kr	Oct	43°	1	INS	10 of 29	27–167
				LID	97 of 97	8–257
		134°	3	INS	9, 10, 28 of 29	23–183
				LID	97, 97, 97 of 97	8–257
		314°	2	INS	10, 27 of 29	27–183
				LID	97, 97 of 97	8–257
		358°	1	INS	9 of 29	27–167
				LID	97 of 97	8–257

As it can be observed, biomass estimates for the data sets based on plot-level measurements generally are more accurate than for those based on maps. In this text, the available reference data will therefore be divided in two groups. The stands and plots with biomass estimated only from plot-level *in-situ* measurements will be referred to as INS-stands, while the other data sets will be referred to as LID-stands, see Table I. Also, to avoid confusion, from this point on both "plots" and "stands" will be referred to as "stands", and treated equally.

C. SAR Data

In Remningstorp, P-band SAR data were collected during three different periods of spring 2007: 3$^{\text{rd}}$ of March, 31$^{\text{st}}$ March to 2$^{\text{nd}}$ of April, and 2$^{\text{nd}}$ of May. At each occasion, two flight headings were used for P-band: 179° and 200° relative north, see the map to the left in Fig. 2. The first track features steeper incident angles for all stands, close to those expected for a spaceborne scenario (all stands lie in near range with nominal incident angles between 26° and 35°). The second track features a wider range of incident angles (between 30° and 50°). It was flown several times at each occasion at different baselines in order to provide PolInSAR and tomographic data.

In Krycklan, P-band SAR data were acquired during two days only: 14^{th} and 15^{th} of October 2008. The first day, the main flight track (134°) was flown several times at different baselines for PolInSAR use. The same area was also covered from the opposite direction (314°). The second day, SAR data of a smaller area were collected from four directions (headings: 43°, 134°, 314°, and 358° relative north). These additional flight tracks were selected in such a way, that the regions with strongest topographic variability were covered by data from all flight tracks. The direction of SAR acquisitions in Krycklan can be seen in the map to the right in Fig. 2.

Averaged, stand-wise backscatter data were extracted from the geocoded SAR images for each stand in both Remningstorp and Krycklan. A buffer zone was also added to avoid border effects. In some cases, there were several geocoded SAR images acquired in the same scenario (same site, same imaging geometry, and same acquisition occasion). Also, not all stands were covered by all images, and thus the number of available stands was different for different scenarios. In Table II, the number of stands and the number of geocoded SAR images available for each scenario are shown.

Henceforth, the different data sets will in some cases be referred to using shorter notation:

- **Site ID (SID)**: Re for Remningstorp and Kr for Krycklan,
- **Group ID (GID)**: INS for *in-situ* based stand-wise data, and LID for lidar based stand-wise data,
- **Date ID (DID)**: Mar, Apr, and May for the acquisitions in Remningstorp in 2007, and Oct for the acquisitions in Krycklan in 2008.

III. Biomass Retrieval Models

In the following section, the models evaluated in this paper will be described. A motivation for the selection of the models introduced in this paper will be given.

In this paper, the following convention will be used:

$$[X]_{\mathrm{dB}} = 10\log_{10}(X), \tag{1}$$

where X is a power ratio. Also,

$$\widehat{\mathcal{W}}_{\mathrm{Mn}} = \log_{10}(\widehat{\mathcal{B}}_{\mathrm{Mn}}), \tag{2}$$

where $\widehat{\mathcal{B}}_{\mathrm{Mn}}$ is a biomass estimate from model Mn in tons/ha.

In Fig. 3, the basic geometry is defined.

The basic measurable from a SAR system is brightness β^0, which is the radar cross section (RCS) per unit slant range area. A system-independent quantity is obtained by projection of β^0 to the ground, i.e. by a normalisation to unit ground range area. This can be done as described in [46]:

$$\sigma^0_{\mathrm{PQ}} = \beta^0_{\mathrm{PQ}} \cdot \cos\psi_i, \tag{3}$$

where the subscript PQ refers to polarisation mode, and

$$\cos\psi_i = \hat{n} \cdot \left(\hat{x} \times \hat{k}_i\right), \tag{4}$$

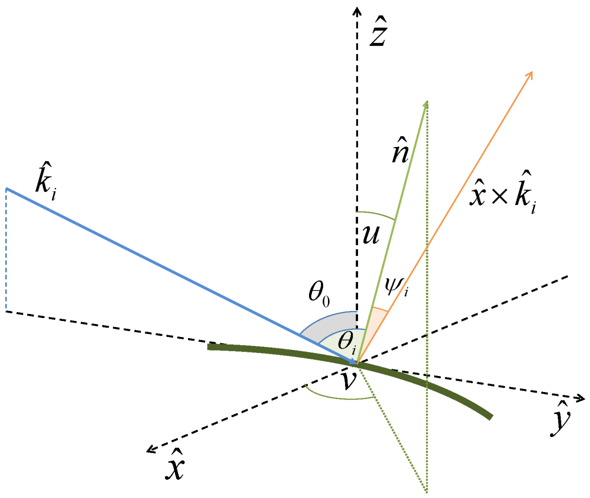

Fig. 3. Basic acquisition geometry. The ground normal is $\widehat{n}$ and the ground slope is defined by the two angles u and v. The incident unit wavevector $\widehat{k_i}$ is assumed to lie in the y-z-plane.

see Fig. 3. Thus, ψ_i is the angle between the image plane normal and the ground surface normal. This procedure reduces the range dependence of β^0 caused by variations in the angle of incidence.

However, some range dependence can still be observed in σ^0, mostly in volumes due to different penetration length at different incident angles [47]. To compensate for that, a quantity called γ^0 is used:

$$\gamma^0_{\mathrm{PQ}} = \frac{\sigma^0_{\mathrm{PQ}}}{\cos\theta_i}, \tag{5}$$

where θ_i is the local incident angle.

A. *Topographic and Temporal Effects*

In Fig. 4, scattering coefficients for HH, HV, and VV, and the ratio HH/VV are plotted against biomass for all data from Remningstorp and Krycklan. The x-axes are the same for all four plots. The y-axes have the same scale (spacing between grid lines), but the values are shifted for better viewing. Colour coding refers to the acquisition time. Running average curves are also plotted in order to simplify trend investigation.

Looking at the three polarisations HH, HV, and VV in Fig. 4, the following observations can be made:

1) VV backscatter is poorly correlated with biomass in all cases,
2) HH backscatter shows much higher variability in Krycklan than in Remningstorp,
3) backscatter at all polarisations is typically several dB lower in Krycklan than in Remningstorp,
4) reduced sensitivity can be observed in Krycklan at all polarisations above approximately 100 tons/ha,
5) an average backscatter shift by around 0–2 dB can be seen from March to May in the Remningstorp data.

Following point 1) it can be concluded that, of all polarisations, VV is least sensitive to biomass, making it a potential indicator of other properties, such as topography, moisture conditions, forest structure, etc. The observation

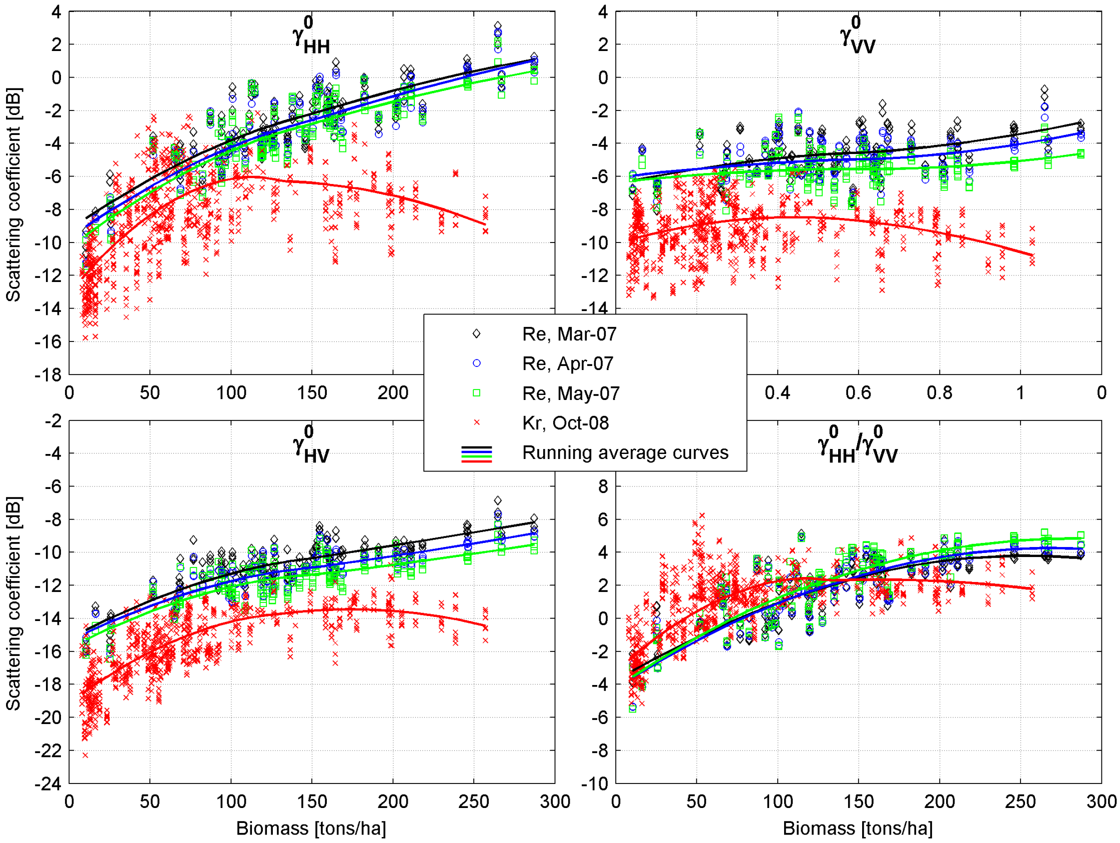

Fig. 4. Backscatter gamma nought for HH, HV and VV, as well as HH/VV backscatter ratio are here plotted in dB for both Krycklan and Remningstorp. Also, the HH/VV-ratio is here plotted in dB. Data points are plotted in different colours and markers if they represent different acquisition time and site. Four running average curves are also plotted to simplify trend investigation. Their colours correspond to the colours of the data points. The grid spacing in y-direction is 2dB in all four plots.

from point 2) can be explained with the influence of topography. Krycklan data feature higher slopes and better directional representation for each stand (acquisitions from multiple headings). The backscatter shift referred to in 3) may have different explanations, such as different forest structure, moisture change, etc. Also, the problem described in 4) is most certainly an effect of topography (most of the high-biomass LID-stands in Krycklan are located in topographic terrain, see Fig. 6 and Sec. III-C). Finally, the backscatter shift in 5) is most likely due to moisture change. Radiometric calibration has been carefully evaluated using trihedral corner reflectors (see [40]) and the maximal measured variation is only 0.8 dB. It is thus concluded that the measured backscatter shift cannot be explained by a radiometric calibration error.

When trying to define a model suitable for both Remningstorp and Krycklan, the five points mentioned above need to be taken into consideration. It is apparent that biomass retrieval from one curve fitted to all (or parts of) the data may often give very poor results when applied on (parts of) the rest of the data.

One possible way to avoid the aforementioned problems is by finding a biomass indicator less susceptible to temporal and topographic variations. This can be partly achieved by using the ratio of HH- and VV-backscatter, the co-polar ratio. This observable has been plotted against biomass in the bottom plot to the right in Fig. 4. By creating the HH- to VV-backscatter ratio, common factors are eliminated. Biophysical forest parameters such as forest structure, ground surface roughness, and moisture will to some degree have similar impact on both HH and VV, and their contribution in biomass estimation can be decreased by the use of HH/VV-ratio. Whereas the temporal and site-to-site change has been reduced, the variability is still high. Therefore, instead of using the ratio on its own, it will be combined with HV-backscatter, which has previously shown the most consistent correlation with biomass [35], at least in areas with modest topographic variations.

As mentioned, the influence of topography has been decreased by the inclusion of the HH/VV-ratio, but not fully suppressed. A complementary way of improving the retrieval is by finding a way to compensate for topographic variations using explicit functions, derived either from experimental data, from models, or from both.

An additional important factor to be considered is the number of regression parameters. With too many regression parameters (too many predictors), the risk of overfitting increases, and the model may lack generality. Moreover, the demand on training data increases as more points are needed for stable fitting. On the other hand, with too few regression parameters, the chosen predictors may not be sufficient for accurate modelling. It is thus important to optimise the number of model parameters.

B. Basic Model

The first approach for a biomass retrieval model is based on a linear function of backscatter in three polarisation channels (based on [10], [12]–[14]):

$$\begin{aligned}\widehat{W}_{\mathrm{M1}} &= a_0 + a_1 \left[\gamma^0_{\mathrm{HV}}\right]_{\mathrm{dB}} + \\ &+ a_2 \left[\gamma^0_{\mathrm{HH}}\right]_{\mathrm{dB}} + a_3 \left[\gamma^0_{\mathrm{VV}}\right]_{\mathrm{dB}}, \end{aligned} \tag{M1}$$

where a_0 to a_3 are model parameters and γ^0_{PQ} is the normalised scattering coefficient gamma nought for polarisation PQ. The model (M1) makes use of three observables, and thus four parameters need to be estimated. The results show, that a_3 has very high uncertainty making γ^0_{VV} not suitable for retrieval (as already observed in Fig. 4). Furthermore, earlier studies indicate that a model based on both HH and HV may not be significantly better than one based on HV alone [13]. Thus, a simpler model using only one polarisation will be evaluated (also used in [35]):

$$\widehat{W}_{\mathrm{M2}} = a_0 + a_1 \left[\gamma^0_{\mathrm{HV}}\right]_{\mathrm{dB}}. \tag{M2}$$

Following the observations about the co-polar ratio made in Fig. 4 and Sec. III-A, i.e. setting

$$a_3 = -a_2,$$

in (M1), a new model including the HH/VV-ratio is constructed:

$$\widehat{\mathcal{W}}_{\mathrm{M3}} = a_0 + a_1 \left[\gamma^0_{\mathrm{HV}}\right]_{\mathrm{dB}} + a_2 \left(\left[\gamma^0_{\mathrm{HH}}\right]_{\mathrm{dB}} - \left[\gamma^0_{\mathrm{VV}}\right]_{\mathrm{dB}}\right), \tag{M3}$$

which makes use of all three observables but only three parameters need to be estimated. A similar model was presented in [10].

C. New Model with Topographic Correction

Although the topographic correction introduced in [4], [25] has shown good results at VHF-band, its functional form is too complicated for this work. Instead, a different approach is chosen. In order to find one single, most important topographic indicator, the following reference functions were fitted to the experimental data:

$$\widehat{\mathcal{W}}_1 = C_{1,0} + C_{1,1} \left[\gamma^0_{\mathrm{HV}}\right]_{\mathrm{dB}}, \tag{6}$$

$$\widehat{\mathcal{W}}_2 = C_{2,0} + C_{2,1} \left(\left[\gamma^0_{\mathrm{HH}}\right]_{\mathrm{dB}} - \left[\gamma^0_{\mathrm{VV}}\right]_{\mathrm{dB}}\right), \tag{7}$$

being the two main elements of (M3). The experimental data were divided into smaller groups with similar ground slope, and the fitting was done separately for each group. This way, each model parameter could be studied against the mean value of the topographic indicator for each group.

Three other topographic indicators were also studied: the local incident angle θ_i, the difference between local and nominal incident angles $\theta_i - \theta_0$, and the surface slope direction angle v. However, qualitative examinations showed that none of these indicators gave conclusive results. Therefore, only the surface slope angle u was chosen to be used in this study.

In the topmost plot in Fig. 5, results from grouping by similar u-angle are shown. The data points are LID-stands from Krycklan with upper biomass limit set to 120 tons/ha. This was done in order to avoid bias introduced by the nonuniform slope-biomass distribution shown in Fig. 6. Each group has approximately the same number of members and the number of groups was chosen manually to give the best possible fitting (small uncertainty intervals).

In the two plots in the bottom part of Fig. 5, the values of the second parameters $C_{1,1}$ and $C_{2,1}$ in Eq. (6) and Eq. (7) are plotted against u. The constant parameters $C_{1,0}$ and $C_{2,0}$ depend not only on u, but also on other effects that cannot be predicted from the observables. They are thus not studied here. Whereas $C_{1,1}$ seems to be quite uncorrelated with u (due to the large variability of the estimated parameters), $C_{2,1}$ shows a clear dependence on u. The first approximation of this dependence is a linear function, which suggests an additional term in (M3) consisting of the product of the surface slope u and the HH/VV-ratio:

$$\begin{aligned}\widehat{\mathcal{W}}_{\mathrm{M4}} =& a_0 + a_1 \left[\gamma^0_{\mathrm{HV}}\right]_{\mathrm{dB}} + a_2 \left(\left[\gamma^0_{\mathrm{HH}}\right]_{\mathrm{dB}} - \left[\gamma^0_{\mathrm{VV}}\right]_{\mathrm{dB}}\right) + \\ &+ a_3 \cdot u \left(\left[\gamma^0_{\mathrm{HH}}\right]_{\mathrm{dB}} - \left[\gamma^0_{\mathrm{VV}}\right]_{\mathrm{dB}}\right).\end{aligned} \tag{M4}$$

D. Reference Models

As reference, models presented in previous works by other researchers will be used. First, a single polarisation model:

$$\widehat{\mathcal{W}}_{\mathrm{R1}} = C_0 + C_1(\left[\gamma^0_{\mathrm{HV}}\right]_{\mathrm{dB}} - b_0), \tag{R1}$$

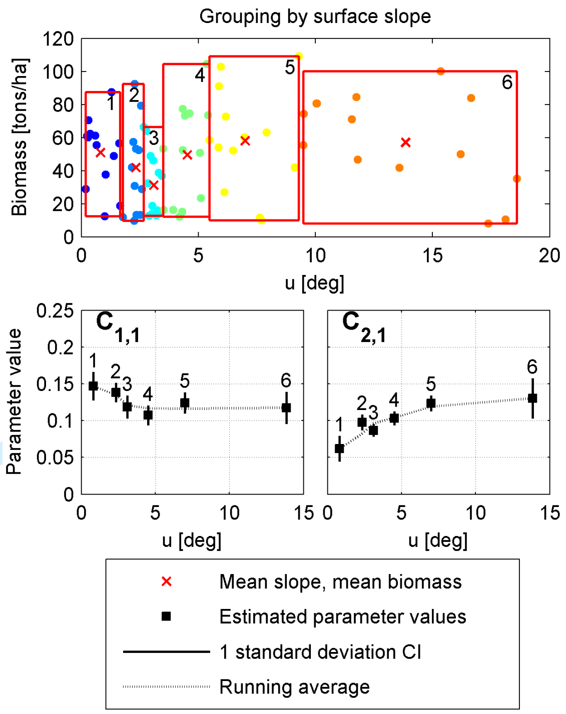

Fig. 5. Results of topographic investigation on LID-stands from Krycklan with upper biomass limit of 120 tons/ha. The topmost plot shows clustering of the data points in groups with similar u-angle and good biomass representation. The groups are delineated with red bounding boxes showing the variability in u and biomass of each group. The red crosses represent the mean slope-mean biomass points for each group. Each group has a number appointed to it in the upper right corner of the corresponding bounding box. The two plots in the bottom show the how the second parameter of the fitted model varies with u for two models. Running average curves are shown for easier trend investigation. One standard deviation confidence intervals for the estimated parameters are also shown.

with constants $C_0 = 3.8914$ and $C_1 = 0.1301$ as presented in [48]. The parameter b_0 is not explicitly included in [48], but is needed, and can be estimated from training data.

Also, a seven-parameter model is used:

$$\begin{aligned}\widehat{W}_{\mathrm{R2}} = a_0 + a_1 \left[\sigma^0_{\mathrm{HV}}\right]_{\mathrm{dB}} + a_2 \left[\sigma^0_{\mathrm{HV}}\right]^2_{\mathrm{dB}} + \\ + a_3 \left[\sigma^0_{\mathrm{HH}}\right]_{\mathrm{dB}} + a_4 \left[\sigma^0_{\mathrm{HH}}\right]^2_{\mathrm{dB}} + \\ + a_5 \left[\sigma^0_{\mathrm{VV}}\right]_{\mathrm{dB}} + a_6 \left[\sigma^0_{\mathrm{VV}}\right]^2_{\mathrm{dB}} .\end{aligned} \tag{R2}$$

This model was described, but not thoroughly studied in [12]. The main model presented in [12] was not used in this study because a comparison with (R2) showed that the latter model was in fact more suitable for BioSAR data, and also had fewer parameters (7 instead of 14). Note, that in (R2), σ^0 is used instead of γ^0.

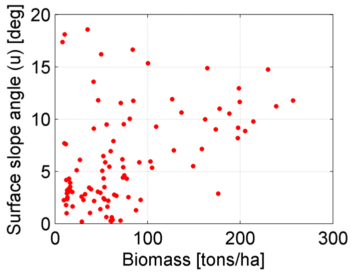

Fig. 6. The distribution of biomass and surface slope for all 91 LID-stands in Krycklan. Note, that above approximately 120 tons/ha, most stands are located in sloping terrain.

IV. Model Validation and Discussion

In this section, the models presented in Sec. III will first be tested on data sets from Remningstorp to evaluate the influence of temporal change, mainly in terms of moisture conditions (Sec. IV-B). Thereafter, the models will be tested on data sets from Krycklan to evaluate the influence of topography (Sec. IV-C). In Sec. IV-D, the models will be evaluated across sites, i.e. models with parameters fitted to one test site will be used for biomass retrieval in the other test site. Next, in Sec. IV-E model errors will be studied against biomass for the three models that showed the best performance in the first three tests. Finally, in Sec. IV-F biomass maps will be produced using the best model, and mapping errors will be pointed out and discussed.

Define the estimation error as:

$$\widehat{R}(i) = \widehat{\mathcal{B}}(i) - \mathcal{B}_{\text{ref}}(i), \tag{8}$$

where $\widehat{\mathcal{B}}(i)$ is the estimated biomass using SAR observation i, $\mathcal{B}_{\text{ref}}(i)$ is the corresponding reference biomass, and N is the number of observations. Note, that one single observation index i sweeps both thorough all stands *and* all acquisitions, and the number of observations N refers to the *total* number of observations. The accuracy of the models will be evaluated using several quantitative measures:

- **Root-mean-square error** (RMSE) is defined as:

$$\text{RMSE} = \sqrt{\frac{1}{N}\sum_i \widehat{R}(i)^2}. \tag{9}$$

- **Bias** is defined as the mean of the estimation error:

$$\text{bias} = \frac{1}{N}\sum_i \widehat{R}(i). \tag{10}$$

With this notation, positive bias means overestimation, and negative bias means underestimation.

- **Standard deviation of the estimation error** can be computed from Eq. (9) and Eq. (10) as:

$$\text{standard deviation} = \sqrt{(\text{RMSE})^2 - (\text{bias})^2}. \tag{11}$$

- The **coefficient of determination** R^2 is a measure of how well a linear model fits the data in comparison with a simple average [49]. It is computed according to:

$$R^2 \quad = \quad 1 - \frac{\sum_i \left(\mathcal{B}_{\mathrm{ref}}(i) - \widehat{\mathcal{B}}(i)\right)^2}{\sum_i \left(\mathcal{B}_{\mathrm{ref}}(i) - \overline{\mathcal{B}}_{\mathrm{ref}}\right)^2}, \tag{12}$$

where

$$\overline{\mathcal{B}}_{\mathrm{ref}} = \frac{1}{N}\sum_i \mathcal{B}_{\mathrm{ref}}(i)$$

is the mean reference biomass. For accurate modelling, R^2 should be as close to one as possible. Values below zero indicate that better modelling results would be achieved with an average of the reference data.

- The **relative error** is defined as:

$$\text{relative error} = 100\,\% \cdot \frac{\widehat{\mathcal{B}} - \mathcal{B}_{\mathrm{ref}}}{\mathcal{B}_{\mathrm{ref}}}. \tag{13}$$

A. Data Selection and Model Training

Since the model performance depends on the reliability of model parameter estimation (model training), the choice of the data used for training demands care.

First, the training data need to cover a large parameter range and have a reasonable accuracy. Lidar-based measurements present a good compromise between accuracy and coverage. Therefore, LID-stands presented in Table I will be used as training data.

The number of SAR measurements is not equal for all stands (see Table II), and not all stands are always covered. Also, in some cases more than one geocoded SAR image is available for each scenario (same site, same imaging geometry, same acquisition date). A bias problem may thus occur. To minimise that problem, only one measurement per stand from each site, each date, and each heading was chosen to be used, and only the LID-stands covered by all images were used for training. The following images were used:

- **Remningstorp**:
  - heading 200°: one image for each date (0109, 0306, and 0411),
  - heading 179°: one image for each date (0110, 0206, and 0412)
- **Krycklan**:
  - heading 314°: one image (0103),
  - heading 134°: one image (0104),
  - heading 358°: one image (0301),
  - heading 43°: one image (0304).

The numbers in parentheses refer to the acquisition numbers of each image, as described in [40] for Remningstorp, and in [41] for Krycklan.

In total, Remningstorp data suitable for training were limited to a maximum of 46 LID-stands (out of 58) and 6 acquisitions for each stand (out of 9, see Table II). For Krycklan, data suitable for training were limited to a maximum of 97 LID-stands and 4 acquisitions for each stand (out of 7, see Table II). Note, that in many cases, smaller subsets of these data sets were used for training. In cases when more than one acquisition per stand was used, different observations in the training data set were not entirely independent of each other, which might cause problems in the statistical analysis. In Sec. IV-E, this issue is pointed out and discussed.

Since all the models used in this text are linear, least-squares as implemented in Matlab function `regress` was used for parameter estimation.

For best quantitative validation, high-accuracy INS-stands were used. For temporal validation in Remningstorp, the same restrictions as for training data applied to validation data in order to be able to make fair comparison between headings. For the other validation scenarios, all available SAR acquisitions for each stand were used for biomass prediction, giving up to 9 biomass values for some stands in Remningstorp and up to 7 biomass values for some stands in Krycklan. This approach increases the influence of the well-represented stands during validation.

B. *Temporal Validation*

In this part, the models were trained using LID-stands in Remningstorp and validated using INS-stands from the same test site. Only the stands fully covered by both 179- and 200-degree acquisitions were used. Each combination of dates was examined, as well as the results of training and validation on all three dates. Root-mean-square errors (RMSE) are presented in Table IV in tons/ha together with the coefficients of determination R^2. The mean biomass for validation data is 185 tons/ha. In this comparison, model (M4) was not included since topography is not significant in Remningstorp.

Looking at same date retrieval (training and validation on the same date), all models show reasonable performance with root-mean-square errors ranging between 35 and 60 tons/ha (19–32 % of mean biomass). However, as the retrieval scenario becomes more difficult, and the training and validation dates are further apart, the single polarisation models (R1) and (M2) often show significantly higher errors compared to models including all polarisations.

Comparing the two headings (and keeping in mind that the 179-degree heading features steeper incident angles) it can be observed that for models (R1) and (M2), the retrieval is more stable across dates for the 179-degree heading (however, it gives in general worse results). Moreover, the data set used for training seems to affect the results much more for the 179-degree heading than for the 200-degree heading, for which only the temporal distance between training and validation data seems of an importance (the error is lowest on the diagonal and higher off-diagonal). This is clearly visible for models (M1) and (M3) at the 179-degree heading, where training on May data gives RMSE around 40 tons/ha, no matter which date is used for validation. For training on April data, the same values lie over 60 tons/ha.

Also when trained and validated using all temporal acquisitions, full polarisation models (R2), (M1), and (M3) show better results, especially for the 200-degree heading with retrieval error as low as 39 tons/ha (21 %).

TABLE III

PARAMETER VALUES FOR THE SIX TESTED MODELS. TRAINING DATA CONSISTS OF ALL AVAILABLE LID-STANDS IN RESPECTIVE TEST SITE COVERED BY EXACTLY ONE IMAGE FROM EACH HEADING AND EACH DATE, SEE SEC. IV-A. THE PARAMETERS ARE COLOURED IN RED IF THEY ARE FOUND VERY UNCERTAIN (THEIR UNCERTAINTY INTERVALS INCLUDE ZERO).

Model:	Parameters estimated in Remningstorp	
(R1)	$b_0 = 2.827 \pm 0.138$	
(R2)	$a_0 = 0.842 \pm 0.650$	$a_1 = 0.065 \pm 0.022$
	$a_2 = -0.206 \pm 0.111$	$a_3 = -0.122 \pm 0.094$
	$a_4 = -0.001 \pm 0.002$	$a_5 = -0.010 \pm 0.004$
	$a_6 = -0.006 \pm 0.007$	
(M1)	$a_0 = 2.886 \pm 0.146$	$a_1 = 0.078 \pm 0.016$
	$a_2 = 0.072 \pm 0.010$	$a_3 = -0.056 \pm 0.015$
(M2)	$a_0 = 3.632 \pm 0.136$	$a_1 = 0.140 \pm 0.012$
(M3)	$a_0 = 2.933 \pm 0.138$	$a_1 = 0.089 \pm 0.011$
	$a_2 = 0.068 \pm 0.009$	
(M4)	$a_0 = 2.967 \pm 0.137$	$a_1 = 0.093 \pm 0.011$
	$a_2 = 0.056 \pm 0.011$	$a_3 = 0.713 \pm 0.411$

Model:	Parameters estimated in Krycklan	
(R1)	$b_0 = 0.766 \pm 0.190$	
(R2)	$a_0 = 2.507 \pm 1.246$	$a_1 = 0.029 \pm 0.059$
	$a_2 = 0.061 \pm 0.144$	$a_3 = -0.105 \pm 0.115$
	$a_4 = -0.001 \pm 0.003$	$a_5 = -0.002 \pm 0.004$
	$a_6 = 0.001 \pm 0.005$	
(M1)	$a_0 = 3.280 \pm 0.203$	$a_1 = 0.138 \pm 0.014$
	$a_2 = 0.049 \pm 0.012$	$a_3 = -0.113 \pm 0.016$
(M2)	$a_0 = 4.087 \pm 0.191$	$a_1 = 0.149 \pm 0.012$
(M3)	$a_0 = 3.402 \pm 0.222$	$a_1 = 0.109 \pm 0.013$
	$a_2 = 0.063 \pm 0.013$	
(M4)	$a_0 = 3.129 \pm 0.211$	$a_1 = 0.093 \pm 0.013$
	$a_2 = 0.020 \pm 0.015$	$a_3 = 0.605 \pm 0.134$

C. *Topographic Validation*

In this part, the models were trained and validated using different heading combinations in Krycklan. The RMSE and R^2 are shown for all training-validation combinations in Table V. The mean biomass level for Krycklan INS-stands is 94 tons/ha. The models which include all three polarisations, (R2), (M1), (M3), and (M4), show slightly better performance than the two single polarised models (R1) and (M2), but the improvement is small. Perhaps surprisingly, the correction in (M4) does not improve the retrieval results in this case because the variability in backscatter from one stand is not reduced by the model (since only the slope angle u is included in the model and this angle is constant for all acquisition geometries).

In general, all models give errors higher than approximately 28 % (26 tons/ha). Validation results are more conclusive for the two main headings (134° and 314°) because the number of validation points is 27 and 28, compared to 9 and 10 for the other two headings. Also, the distribution of slopes for different biomass levels is nonuniform in the training data. The high-biomass stands are situated in sloping terrain, see Fig. 6.

D. Across-Site Validation

The across-site test was done in two steps: training in Remningstorp and validation in Krycklan, and vice versa. These two tests will be evaluated separately.

1) Flat-to-Topographic: A problem occurs when the models are trained using Remningstorp data and validated using Krycklan data: Remningstorp data do not include enough topographic variations for reliable training; the retrieval models perform poorly if only Remningstorp data are used, see Table VI. Retrieval errors are at minimum 37 % (35 tons/ha), but the variability of the data is large, and the coefficient of determination is low. In terms of RMSE, model (M4) performs best here. However, R^2-values are low.

In Fig. 7, scatter plots showing estimation results for all six models are shown. Acquisitions from all three dates and both headings in Remningstorp were used for training (model parameters as in Table III). Retrieval results for all Krycklan data are shown in the plots, in red for LID-stands and in black for INS-stands. For all models except (M4), biomass in Krycklan is underestimated. For (M4), the variability in data is larger compared to the rest of the models, but the bias is reduced.

2) Topographic-to-Flat: Here, LID data from the topographic area of Krycklan, featuring a variety of stands in different slope conditions, were used for training of the models. In Table VII, the resulting RMSE values are shown together with the coefficient of determination R^2. The mean biomass for Remningstorp INS-stands is 185 tons/ha. It can be observed that retrieval errors as low as 22 % (40 tons/ha) can be achieved with (M4). Single-polarisation models (R1) and (M2), and model (M3) show all extremely high errors going above 100 % of mean biomass level. This validation scenario shows clearly the advantage of models (R2), (M1), and (M4). For (M4), the R^2-values are also high, see Table VII.

In Fig. 8, scatter plots showing estimation results for all six models are shown. Acquisitions from all four headings in Krycklan were used for training (model parameters as in Table III). Retrieval results for all Remningstorp data are shown in the plots, in blue for LID-stands and in black for INS-stands. For all models except (M4) and (R2), biomass in Remningstorp is overestimated. For (M4), the variability in data is larger compared to (R2), but the bias (underestimation) observed above 200 tons/ha is reduced.

E. Error Analysis

Looking at the results presented in the previous three sections, it can be observed that models (R2), (M1), and (M4) show best overall performance of the six studied models. Models (M1) and (M4) have the advantage of having less parameters and showing better results in flat-to-topographic retrieval. Although (R2) gives less variability (improved precision) in the higher biomass levels, a loss of sensitivity (reduced accuracy, higher bias) can be observed for biomass values above 200 tons/ha. Whereas the precision of a model can be improved using spatial averaging, it is difficult to improve the accuracy. Therefore, a limited increase in variability is an acceptable trade-off for lower bias.

As mentioned in Sec. IV-A, all observations used for training are not completely independent, since several observations from the same stand but with different imaging geometry and/or acquisition date are used simultaneously for parameter estimation. This breach of independence can be observed in Fig. 4 as clustering of observations from the same stand. This might induce slightly different parameter estimates compared to the estimates, which would be obtained if the full dependence structure of the observations was known. However, since the majority of pairs of observations are independent, these differences are likely to be small. Moreover, small differences in parameter estimates compared to ”true” parameter values are not of concern in this study. The main focus of this paper is not the parameter estimation, but rather the performance analysis and the comparison of different models. The only real concern is the estimation of confidence intervals, which will be affected by the presence of unknown correlation between observations.

With the above discussion in mind, some conclusions can nevertheless be drawn from Table III containing the estimated regression parameters. In particular, some of the coefficients for (R2) are not significantly different from zero (their confidence intervals include zero). This indicates that the model contains too many predictors. Note also, that the parameters of model (M4) are similar for both Remningstorp and Krycklan. This is an indication that the coefficients of this model are stable over a broad range of forest conditions.

In Fig. 9, bias (mean of the estimation error), standard deviation of the estimation error, and RMSE are plotted against biomass for models (R2), (M1), and (M4). These quantities have been defined in Eq. (9)-Eq. (11). For this study, the model parameters were those specified in Table III. Statistics were computed for LID-stands in both Remningstorp and Krycklan, and the averaging was done in three intervals: low biomass (0–100 tons/ha), medium biomass (100–200 tons/ha), and high biomass (200–300 tons/ha).

It can be observed that all three models perform almost equally well when both trained and evaluated in Remningstorp (solid lines in the top three plots in Fig. 9). Model (R2) shows higher bias in the high-biomass group (underestimation with approximately 40 tons/ha), but the variability is quite small (standard deviation up to 30 tons/ha). When training and validation are both done in Krycklan (solid lines in the bottom three plots in Fig. 9), one can observe a strong underestimation occurring for stands with biomass above 100 tons/ha and a high variability. The origin of this bias can probably be related to the nonuniform biomass-slope distribution mentioned earlier and shown in Fig. 6, but a clear conclusion is difficult to be made as the number of independent data points is low. Also, the fact that none of the models compensates for variability with angle v contributes to the observed large variability. All three models perform similarly.

It is during across-site validation that (M4) proves itself better than the other two models. Lower bias is observed when training on Remningstorp and applying to Krycklan (dashed lines in the bottom three plots in Fig. 9). In the opposite case, (R2) shows lower bias for low-biomass stands, but higher in the two other groups (dashed lines in the top three plots in Fig. 9). Although (M4) shows in some cases slightly higher standard deviation of residuals, this effect can be reduced by spatial averaging. Bias is more difficult to reduce and should thus be kept as low as possible. Altogether, (M4) is observed as the best of the six models examined in this paper. Note, that in Krycklan, there is a lack of stands with high biomass and low slopes, whereas in Remningstorp these types of stands are common. An extrapolation is made for such stands when the model (M4) is trained in Krycklan and evaluated in Remningstorp. The exact influence of this effect on the retrieval is unclear.

F. Biomass Mapping Performance Analysis

In order to evaluate mapping performance of the new model, biomass maps were created from SAR images using (M4). In Fig. 10, a set of biomass maps is shown. To the left, biomass maps based on lidar scanning are shown. In the middle and to the right, two biomass maps extracted from SAR using (M4) are shown. For both Remningstorp and Krycklan, the same SAR images as used for training were used (those described in Sec. IV-A, 6 images for Remningstorp and 4 images for Krycklan). Geocoded images with pixel size $2\,\mathrm{m} \times 2\,\mathrm{m}$ were first filtered using an average filter with a 5×5 window to match the resolution of the lidar-based biomass maps. Next, the filtered SAR images were re-sampled using linear interpolation to the same grid as the lidar-based biomass maps ($10\,\mathrm{m} \times 10\,\mathrm{m}$). Thereafter, all biomass maps were filtered with a 7×7 average filter in order to reduce resolution to approximately $70\,\mathrm{m} \times 70\,\mathrm{m}$ to match the size of the smallest stand in the data sets used for training (0.5 ha). Biomass maps were then produced from all SAR images and averaged. In Fig. 10, only the regions covered by all acquisitions in the respective test sites are shown. The parameters used for map creation can be found in Table III.

The SAR-based biomass maps show good qualitative agreement with the lidar-based maps. However, in some regions there are distinct differences between the maps. Three such examples are marked with black contours in Fig. 10.

In the large, irregular region ”A” in the central-left part of Remningstorp, an overestimation with 100–150 tons/ha is observed. One INS-stand (here called #5, biomass: 167 tons/ha) is located within this region. A careful cross-check with reference *in-situ* and lidar data does not indicate any major issues related to the biomass map itself. However, according to Table 8.1 in [40], stand #5 consists to 50 % of pine, which contributes to 95 % of the total biomass in this stand. The remaining 5 % is concentrated in a layer of understorey vegetation. This fact has been observed during field visits, and it can also be seen in the lidar height data. The understorey layer makes a large contribution to the HV-backscatter through the increased number of vegetation scatterers. An investigation in the original SAR data shows, that HV is more affected by this vegetation layer than HH.

In the oblong region ”B”, a disagreement of the order of 100–150 tons/ha between lidar and SAR biomass maps is observed in Fig. 10. One forest stand is located within region ”B”. This stand is shown in Figure 6.17 in [40] as #11 (biomass: 273 tons/ha, not used in this study due to its small size, $20\,\mathrm{m} \times 50\,\mathrm{m}$). An investigation of the lidar height data shows, that the high-biomass area containing stand #11 is small and surrounded by sparser forest with lower trees. Therefore, filtering of the lidar map will lead to underestimation of biomass around stand #11. Also, the DEM shows, that region ”B” is located on a slope, which increases the HV-backscatter. This leads to an overestimation of biomass in the SAR-based biomass map. Summarising, the disagreement between lidar and SAR in region ”B” is both due to an overestimation in the SAR map, and an underestimation in the lidar map.

Also in region ”C”, another disagreement is observed. The region consists of a group of tall trees situated on plane ground, with virtually no forest between them and the SAR. This increases the difference between HH- and VV-backscatter through the double-bounce effect, thus increasing the ratio. Moreover, smoothing of biomass map decreases the reference biomass level in a similar way as in region ”B”.

In Fig. 11 and Fig. 12, histograms and cumulative distributions for the relative error defined in Eq. (13) are shown. Here, the lidar-based biomass map was used as $\mathcal{B}_{ref}$ and the estimated SAR biomass maps were used as $\widehat{\mathcal{B}}$. The data have been divided in three biomass groups: 0–100 tons/ha, 100–200 tons/ha, and 200 tons/ha and above. In the upper left corner of each subplot, the size of each group relative the total number of pixels in percent is shown (in parentheses, corresponding percentage of the training data in each group is shown). In black dashed lines, the corresponding distributions for the whole image are plotted.

In general, between 35 and 50 % of all pixels are estimated with relative error smaller than 25 %. In Remningstorp, especially good estimation results are obtained for pixels with lidar biomass higher than 200 tons/ha (80–90 % pixels showed relative error smaller than 25 %). There is also a group of pixels with low lidar biomass, for which biomass is overestimated with more than 100 %. However, in terms of biomass error (measured in tons per hectare) this overestimation is not large.

In Krycklan, a general underestimation is observed for pixels with biomass larger than 100 tons/ha, especially when Remningstorp-based parameters are used. However, since only 12 % of all pixels in the Krycklan map correspond to lidar biomass lower than 100 tons/ha, and the topography in Remningstorp is not strong, these results are less conclusive.

V. SUMMARY AND CONCLUSIONS

A new biomass retrieval model for boreal forest using polarimetric P-band SAR backscatter is presented in this paper. The model is based on two main SAR quantities: the HV backscatter and the HH/VV backscatter ratio, and it also includes a first order topographic correction, the ground slope angle u.

The paper is based on analysis of data from two airborne P-band SAR campaigns, BioSAR 2007 and 2008, conducted in the two Swedish test sites Remningstorp and Krycklan, separated by 720 km. The examined stand-level biomass interval is 0–300 tons/ha and the surface slope goes up to 19°, measured on a 50 m × 50 m posting DEM. Only forest stands with areas greater than 0.5 ha are used in this work. An average difference between the data from Remningstorp and Krycklan is observed in all polarisation channels, and more work is needed to fully understand and model it in terms of seasonal, topographic, and forest structure differences.

Compared to previously published models, the new model shows less bias induced by temporal change and topographic variability. Also, it gives reliable biomass retrieval results during across-site validation, that is when biomass estimation in one test site is evaluated using a model developed using data from the other test site.

Firstly, all relevant models were tested on data sets coming from Remningstorp, acquired at three occasions during the spring of 2007, each separated by roughly one month. This test showed, that the use of multiple polarisations significantly improves the performance. Also, the use of the HH/VV-ratio instead of HH- and VV-channels separately simplifies the model without sacrificing any performance.

The models were also tested for bias due to topographic variability using SAR data acquired from different directions in topographic terrain in Krycklan. The new model gave errors of 27–40 tons/ha (corresponding to 29–43 % of the the mean biomass in Krycklan, 94 tons/ha), whereas all the other models gave comparable or worse results. The results of this test were not conclusive, due to non-uniform biomass-slope distribution in the training data.

Thereafter, the across-site retrieval performance was evaluated. The test site used for training was thus distinctly different from the test site used for validation. With model parameters estimated on Krycklan data, biomass in Remningstorp could be estimated with root-mean-square errors of 40–59 tons/ha, or 22–32 % of the mean biomass. The other models produced errors that were at least 50 % higher. In the inverse scenario, the Krycklan site was not well represented in the training data set (too small topographic variability in Remningstorp), and errors of 35–51 tons/ha were measured (37–54 % of the mean biomass in Krycklan). In terms of RMSE, the new model showed better results than the other models. The coefficient of determination R^2 was however low, and it was concluded that the training set was not sufficiently representative in terms of ground surface slopes.

Lastly, biomass maps estimated using the new model with two parameter sets (one for each test site) were compared to lidar-based biomass maps. Compared to the lidar-based biomass maps, the new model presented qualitatively similar results. In some areas, however, biomass was overestimated with SAR which could be explained based on basic scattering properties of forest in connection to observations made in field and in the lidar data.

In general, between 35 and 45 % of all pixels in the maps were estimated with relative difference between the maps smaller than 25 %. In Remningstorp, especially good agreement were obtained for pixels with lidar-estimated biomass higher than 200 tons/ha (80–90 % pixels showed relative difference smaller than 25 %). In Krycklan, a general underestimation was observed for pixels with biomass larger than 100 tons/ha, especially when Remningstorp-based parameters were used. However, since only 12 % of all pixels in the Krycklan map correspond to lidar biomass lower than 100 tons/ha, and the topography in Remningstorp is not strong, these results are not conclusive.

ACKNOWLEDGMENT

The authors would like to thank both the Swedish National Space Board (SNSB) and the European Space Agency (ESA) for funding of this project, the German Aerospace Center (DLR) for the ESAR data, and Swedish University of Agricultural Sciences (SLU) for the field data.

REFERENCES

[1] IPCC, *Climate Change 2007: The Physical Science Basis. Contribution of Working Group I to the Fourth Assessment Report of the Intergovernmental Panel on Climate Change*, S. Solomon, M. M. Dahe Qin, M. Marquis, K. Averyt, M. M. B. Tignor, and H. L. Miller, Eds. Cambridge, United Kingdom and New York, NY, USA: Cambridge University Press, 2007. [Online]. Available: http://www.ipcc.ch/publications_and_data/publications_ipcc_fourth_assessment_report_wg1_report_the_physical_science_basis.htm

[2] C. Parker, A. Mitchell, M. Trivedi, and N. Mardas, "The little REDD book: A guide to governmental and non-governmental proposals for reducing emissions from deforestation and degradation," November 2008. [Online]. Available: http://www.amazonconservation.org/pdf/redd_the_little_redd_book_dec_08.pdf

[3] E. Næsset, T. Gobakken, S. Solberg, T. G. Gregoire, R. Nelson, G. Ståhl, and D. Weydahl, "Model-assisted regional forest biomass estimation using lidar and InSAR as auxiliary data: A case study from a boreal forest area," *Remote Sensing of Environment*, vol. 115, no. 12, pp. 3599–3614, 2011. [Online]. Available: http://www.sciencedirect.com/science/article/pii/S0034425711003257

[4] K. Folkesson, G. Smith-Jonforsen, and L. M. H. Ulander, "Model-based compensation of topographic effects for improved stem-volume retrieval from CARABAS-II VHF-band SAR images," *IEEE Transactions on Geoscience and Remote Sensing*, vol. 47, no. 4, pp. 1045–1055, April 2009. [Online]. Available: http://ieeexplore.ieee.org/xpls/abs_all.jsp?arnumber=4799122

[5] T. Le Toan, A. Beaudoin, J. Riom, and D. Guyon, "Relating forest biomass to SAR data," *IEEE Transactions on Geoscience and Remote Sensing*, vol. 30, no. 2, pp. 403–411, 1992. [Online]. Available: http://ieeexplore.ieee.org/xpls/abs_all.jsp?arnumber=134089&tag=1

[6] A. Beaudoin, T. L. Le Toan, S. Goze, E. Nezry, A. Lopes, E. Mougin, C. C. Hsu, H. C. Han, J. A. Kong, and R. T. Shin, "Retrieval of forest biomass from SAR data," *International Journal of Remote Sensing*, vol. 15, no. 14, pp. 2777–2796, 1994. [Online]. Available: http://www.tandfonline.com/doi/abs/10.1080/01431169408954284

[7] H. Israelsson, J. Askne, and R. Sylvander, "Potential of SAR for forest bole volume estimation," *International Journal of Remote Sensing*, vol. 15, no. 14, pp. 2809–2826, 1994. [Online]. Available: http://www.tandfonline.com/doi/abs/10.1080/01431169408954286

[8] K. J. Ranson and G. Sun, "Mapping biomass of a northern forest using multifrequency SAR data," *IEEE Transactions on Geoscience and Remote Sensing*, vol. 32, no. 2, pp. 388–396, 1994. [Online]. Available: http://ieeexplore.ieee.org/xpls/abs_all.jsp?arnumber=295053&tag=1

[9] M. L. Imhoff, "Radar backscatter and biomass saturation: ramifications for global biomass inventory," *IEEE Transactions on Geoscience and Remote Sensing*, vol. 33, no. 2, pp. 511–518, 1995. [Online]. Available: http://ieeexplore.ieee.org/xpls/abs_all.jsp?arnumber=377953

[10] E. J. Rignot, R. Zimmermann, and J. J. van Zyl, "Spaceborne applications of P band imaging radars for measuring forest biomass," *IEEE Transactions on Geoscience and Remote Sensing*, vol. 33, no. 5, pp. 1162–1169, 1995. [Online]. Available: http://ieeexplore.ieee.org/xpls/abs_all.jsp?arnumber=469480

[11] D. H. Hoekman and M. J. Quiriones, "Land cover type and biomass classification using AirSAR data for evaluation of monitoring scenarios in the Colombian Amazon," *IEEE Transactions on Geoscience and Remote Sensing*, vol. 38, no. 2, pp. 685–696, 2000. [Online]. Available: http://ieeexplore.ieee.org/xpls/abs_all.jsp?arnumber=841998

[12] S. Saatchi, K. Halligan, D. Despain, and R. Crabtree, "Estimation of forest fuel load from radar remote sensing," *IEEE Transactions on Geoscience and Remote Sensing*, vol. 45, pp. 1726–1740, 2007. [Online]. Available: http://ieeexplore.ieee.org/xpls/abs_all.jsp?arnumber=4215087

[13] G. Sandberg, L. M. H. Ulander, J. E. S. Fransson, J. Holmgren, and T. L. Toan, "L- and P-band backscatter intensity for biomass retrieval in hemiboreal forest," *Remote Sensing of Environment*, vol. 115, no. 11, pp. 2874–2886, 2011. [Online]. Available: http://www.sciencedirect.com/science/article/pii/S0034425711001350

[14] S. Saatchi, M. Marlier, R. L. Chazdon, D. B. Clark, and A. E. Russell, "Impact of spatial variability of tropical forest structure on radar estimation of aboveground biomass," *Remote Sensing of Environment*, vol. 115, no. 11, pp. 2836–2849, 2011. [Online]. Available: http://www.sciencedirect.com/science/article/pii/S0034425711001313

[15] S. R. Cloude and K. P. Papathanassiou, "Polarimetric SAR interferometry," *IEEE Transactions on Geoscience and Remote Sensing*, vol. 36, no. 5, pp. 1551–1565, 1998. [Online]. Available: http://ieeexplore.ieee.org/xpls/abs_all.jsp?arnumber=718859

[16] K. P. Papathanassiou and S. R. Cloude, "Single-baseline polarimetric SAR interferometry," *IEEE Transactions on Geoscience and Remote Sensing*, vol. 39, pp. 2352–2363, 2001. [Online]. Available: http://ieeexplore.ieee.org/xpls/abs_all.jsp?arnumber=964971

[17] S. R. Cloude and K. P. Papathanassiou, "Three-stage inversion process for polarimetric SAR interferometry," *IEE Proceedings on Radar, Sonar & Navigation*, vol. 150, no. 3, pp. 125–134, 2003. [Online]. Available: http://ieeexplore.ieee.org/xpls/abs_all.jsp?arnumber=1222372

[18] I. H. Woodhouse, "Predicting backscatter-biomass and height-biomass trends using a macroecology model," *IEEE Transactions on Geoscience and Remote Sensing*, vol. 44, no. 4, pp. 871–877, April 2006. [Online]. Available: http://ieeexplore.ieee.org/xpls/abs_all.jsp?arnumber=1610823

[19] M. Neumann, L. Ferro-Famil, and A. Reigber, "Multibaseline polarimetric SAR interferometry coherence optimization," *IEEE Geoscience and Remote Sensing Letters*, vol. 5, no. 1, pp. 93–97, January 2008. [Online]. Available: http://ieeexplore.ieee.org/xpls/abs_all.jsp?arnumber=4382931

[20] ——, "Estimation of forest structure, ground, and canopy layer characteristics from multibaseline polarimetric interferometric SAR data," *IEEE Transactions on Geoscience and Remote Sensing*, vol. 48, no. 3, pp. 1086–1104, March 2010. [Online]. Available: http://ieeexplore.ieee.org/xpls/abs_all.jsp?arnumber=5299063

[21] A. Reigber and A. Moreira, "First demonstration of airborne SAR tomography using multibaseline L-band data," *IEEE Transactions on Geoscience and Remote Sensing*, vol. 38, no. 5, pp. 2142–2152, September 2000. [Online]. Available: http://ieeexplore.ieee.org/xpls/abs_all.jsp?arnumber=868873

[22] S. R. Cloude, "Polarization coherence tomography," *Radio Science*, vol. 41, 2006. [Online]. Available: http://www.agu.org/pubs/crossref/2006/2005RS003436.shtml

[23] S. Tebaldini, "Single and multipolarimetric SAR tomography of forested areas: A parametric approach," *IEEE Transactions on Geoscience and Remote Sensing*, vol. 48, no. 5, pp. 2375–2387, May 2010. [Online]. Available: http://ieeexplore.ieee.org/xpls/abs_all.jsp?arnumber=5406055

[24] B. Hallberg, G. Smith-Jonforsen, L. M. H. Ulander, and G. Sandberg, "A physical-optics model for double-bounce scattering from tree stems standing on an undulating ground surface," *IEEE Transactions on Geoscience and Remote Sensing*, vol. 46, no. 9, pp. 2607–2621, 2008. [Online]. Available: http://ieeexplore.ieee.org/xpls/abs_all.jsp?arnumber=4599195

[25] G. Smith-Jonforsen, L. M. H. Ulander, and X. Luo, "Low VHF-band backscatter from coniferous forests on sloping terrain," *IEEE Transactions on Geoscience and Remote Sensing*, vol. 43, no. 10, pp. 2246–2260, 2005. [Online]. Available: http://ieeexplore.ieee.org/xpls/abs_all.jsp?arnumber=1512396

[26] J. J. van Zyl, "The effect of topography on radar scattering from vegetated areas," *IEEE Transactions on Geoscience and Remote Sensing*, vol. 31, no. 1, pp. 153–160, 1993. [Online]. Available: http://ieeexplore.ieee.org/xpls/abs_all.jsp?arnumber=210456

[27] Y.-C. Lin and K. Sarabandi, "Electromagnetic scattering model for a tree trunk above a tilted ground plane," *IEEE Transactions on Geoscience and Remote Sensing*, vol. 33, no. 4, pp. 1063–1070, July 1995. [Online]. Available: http://ieeexplore.ieee.org/xpls/abs_all.jsp?arnumber=406692

[28] Y. Dong and J. A. Richards, "Studies of the cylinder-ground double bounce scattering mechanism in forest backscatter models," *IEEE Transactions on Geoscience and Remote Sensing*, vol. 33, no. 1, pp. 229–231, January 1995.

[29] J. Lopez-Sanchez, H. Esteban-Gonzalez, M. Baquero-Escudero, and J. Fortuny-Guasch, "An electromagnetic scattering model for multiple tree trunks above a tilted rough ground plane," *IEEE Transactions on Geoscience and Remote Sensing*, vol. 37, no. 2, pp. 659–667, March 1999. [Online]. Available: http://ieeexplore.ieee.org/xpls/abs_all.jsp?arnumber=752183

[30] G. Smith and L. M. H. Ulander, "A model relating VHF-band backscatter to stem volume of coniferous boreal forest," *IEEE Transactions on Geoscience and Remote Sensing*, vol. 38, no. 2, pp. 728–740, March 2000. [Online]. Available: http://ieeexplore.ieee.org/xpls/abs_all.jsp?arnumber=842002

[31] M. L. Williams, *PolSARproSim: A Coherent, Polarimetric SAR Simulation of Forests for PolSARPro; Design Document and Algorithm Specification (u1.0)*, December 2006. [Online]. Available: http://envisat.esa.int/polsarpro/Manuals/PolSARproSim_Design.pdf

[32] T. Le Toan, H. Baltzer, P. Paillou, K. Papathanassiou, S. Plummer, S. Quegan, F. Rocca, and L. Ulander, "ESA SP-1313/2 candidate Earth Explorer core missions - reports for assessment: BIOMASS," European Space Agency, Tech. Rep., 2008. [Online]. Available: http://esamultimedia.esa.int/docs/SP1313-2_BIOMASS.pdf

[33] M. Arcioni *et al.*, "Biomass, CoReH2O, PREMIER: ESA's candidate 7th Earth Explorer missions," in *IEEE International Geoscience and Remote Sensing Symposium (IGARSS)*, Honolulu, July 2010, pp. 673–676. [Online]. Available: http://ieeexplore.ieee.org/xpls/abs_all.jsp?arnumber=5651853

[34] K. Scipal *et al.*, "The BIOMASS mission – an ESA Earth Explorer candidate to measure the biomass of the Earth's forests," in *IEEE International Geoscience and Remote Sensing Symposium (IGARSS)*, Honolulu, July 2010, pp. 52–55. [Online]. Available: http://ieeexplore.ieee.org/xpls/abs_all.jsp?arnumber=5653944

[35] T. Le Toan *et al.*, "The BIOMASS mission: Mapping global forest biomass to better understand the terrestrial carbon cycle," *Remote Sensing of Environment*, vol. 115, no. 11, pp. 2850–2860, 2011. [Online]. Available: http://www.sciencedirect.com/science/article/pii/S0034425711001362

[36] M. J. Soja, G. Sandberg, and L. M. H. Ulander, "Topographic correction for biomass retrieval from P-band SAR data in boreal forests," in *IEEE International Geoscience and Remote Sensing Symposium (IGARSS)*, Honolulu, 2010. [Online]. Available: http://ieeexplore.ieee.org/xpls/abs_all.jsp?arnumber=5653944

[37] G. Sandberg, M. J. Soja, and L. M. H. Ulander, "Impact and modeling of topographic effects on P-band SAR backscatter from boreal forests," in *IEEE International Geoscience and Remote Sensing Symposium (IGARSS)*, Vancouver, 2011. [Online]. Available: http://ieeexplore.ieee.org/xpls/abs_all.jsp?arnumber=6049981

[38] M. Neumann, S. S. Saatchi, L. M. H. Ulander, and J. E. S. Fransson, "Parametric and non-parametric forest biomass estimation from PolInSAR data," in *IEEE International Geoscience and Remote Sensing Symposium (IGARSS)*, Vancouver, July 2011, pp. 420–423. [Online]. Available: http://ieeexplore.ieee.org/xpls/abs_all.jsp?arnumber=6049154

[39] L. M. H. Ulander, G. Sandberg, and M. J. Soja, "Biomass retrieval algorithm based on P-band BioSAR experiments of boreal forest," in *IEEE International Geoscience and Remote Sensing Symposium (IGARSS)*, Vancouver, July 2011, pp. 4245–4248. [Online]. Available: http://ieeexplore.ieee.org/xpls/abs_all.jsp?arnumber=6050168

[40] I. Hajnsek, R. Scheiber, L. Ulander, A. Gustavsson, G. Sandberg, S. Tebaldini, A. M. Guarnieri, F. Rocca, F. Bombardini, and M. Pardini, "BioSAR 2007 technical assistance for the development of airborne SAR and geophysical measurements during the BioSAR 2007 experiment: Final report without synthesis," ESA contract no. 20755/07/NL/CB, Tech. Rep., 2008. [Online]. Available: http://earth.esa.int/campaigns/DOC/biosar_finalreports_nosynthesis.pdf

[41] I. Hajnsek *et al.*, "BIOSAR 2008 Technical Assistance for the Development of Airborne SAR and Geophysical Measurements during the BioSAR 2008 Experiment: Final Report BIOSAR Campaign," ESA contract no. 22052/08/NL/CT, Tech. Rep., 2009. [Online]. Available: http://earth.esa.int/campaigns/DOC/BIOSAR2_final_report.pdf

[42] L. M. H. Ulander, A. Gustavsson, P. Dubois-Fernandez, X. Depuis, J. E. S. Fransson, J. Holmgren, J. Wallerman, L. E. B. Eriksson, G. Sandberg, and M. J. Soja, "BioSAR 2010 - a SAR campaign in support to the BIOMASS mission," in *IEEE International Geoscience and Remote Sensing Symposium (IGARSS)*, Vancouver, July 2011, pp. 1528–1531. [Online]. Available: http://ieeexplore.ieee.org/xpls/abs_all.jsp?arnumber=6049359

[43] L. M. H. Ulander *et al.*, "BioSAR 2010 Technical Assistance for the Development of Airborne SAR and Geophysical Measurements during the BioSAR 2010 Experiment: Final Report," ESA contract no. 4000102285/10/NL/JA/ef, Tech. Rep., 2011. [Online]. Available: http://earth.esa.int/campaigns/DOC/BioSAR_2010_final_report_v1.0.pdf

[44] J. E. S. Fransson, F. Walter, and L. M. H. Ulander, "Estimation of forest parameters using CARABAS-II VHF SAR data," *IEEE Transactions on Geoscience and Remote Sensing*, vol. 38, no. 2, pp. 720–727, March 2000. [Online]. Available: http://ieeexplore.ieee.org/xpls/abs_all.jsp?arnumber=842001

[45] J. E. S. Fransson, M. Magnusson, G. Sandberg, L. M. H. Ulander, and A. Gustavsson, "Forest database for single trees in Remningstorp, Västergötland, Sweden, version 2.0," 2008, Swedish University of Agricultural Sciences, Umeå (unpublished).

[46] L. M. H. Ulander, "Radiometric slope correction of synthetic aperture radar images," *IEEE Transactions on Geoscience and Remote Sensing*, vol. 34, no. 5, pp. 1115–1122, 1996. [Online]. Available: http://ieeexplore.ieee.org/xpls/abs_all.jsp?arnumber=536527

[47] E. P. W. Attema and F. T. Ulaby, "Vegetation modeled as a water cloud," *Radio Science*, vol. 13, no. 2, pp. 357–364, 1978. [Online]. Available: http://www.agu.org/pubs/crossref/1978/RS013i002p00357.shtml

[48] T. Le Toan *et al.*, "P-band SAR wave interaction and information retrieval: Analysis and inversion of P-band SAR data for forest biomass and height mapping," Final Report, ESA Contract No. 20290/06/NL/LvH, Tech. Rep., 2011.

[49] N. R. Draper and H. Smith, *Applied Regression Analysis*, 3rd ed. John Wiley & Sons Inc., 1998.

Maciej Jerzy Soja was born in 1985 in Warsaw, Poland. He received the B.Sc. and M.Sc. degree in engineering physics from Chalmers University of Technology, Gothenburg, Sweden, in 2008 and 2009, respectively. Since 2009, he is pursuing his Ph.D. degree in remote sensing in the Radar Remote Sensing Group at the Department of Earth and Space Sciences at Chalmers University of Technology. His main research topic is synthetic aperture radar in forestry.

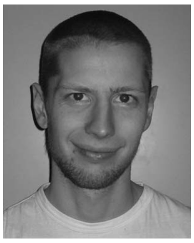

Gustaf Sandberg received the M.Sc. degree in engineering physics from the Chalmers University of Technology, Gothenburg, Sweden, in 2006, where he is currently working toward the Ph.D. degree in the Department of Earth and Space Sciences. His main research interests lie in synthetic aperture radar analysis, with emphasis on ionospheric effects as well as L- and P-band measurements of forests.

Lars M. H. Ulander (S'86-M'90-SM'04) received the M.Sc. degree in engineering physics in 1985 and the Ph.D. degree in electrical and computer engineering in 1991, both from Chalmers University of Technology. Since 1995 he has been with the Swedish Defence Research Agency (FOI) in Linköping where he is Director of Research in radar signal processing. He is also Adjunct Professor in radar remote sensing at Chalmers University of Technology. His research areas are synthetic aperture radar (SAR), electromagnetic scattering models and remote sensing applications. He is the author or co-author of over 250 professional publications, of which more than 50 are in peer-reviewed scientific journals. He is the holder of five patents and is also a member of the Remote Sensing Committee at the Swedish National Space Board.

TABLE IV

RESULTS OF **TEMPORAL VALIDATION** OF MODELS 1–5 IN TERMS OF RMSE (TONS/HA, FIRST ROW) AND R^2 (SECOND ROW). COLOUR CODING BY RMSE RELATIVE MEAN BIOMASS (185 TONS/HA): WHITE FOR 20 % AND BELOW, BLACK FOR 100 % AND ABOVE.

Heading: 179° — TRAINING

Model:		R1			R2			M1			M2			M3		
VALIDATION		Mar	Apr	May	Mar	Apr	May	Mar	Apr	May	Mar	Apr	May	Mar	Apr	May
Mar	RMSE	50	61	71	42	46	82	55	84	41	55	89	85	51	78	38
	R^2	0.43	0.14	-0.16	0.6	0.53	-0.53	0.32	-0.59	0.61	0.31	-0.81	-0.67	0.4	-0.4	0.66
Apr	RMSE	65	53	52	41	39	71	49	65	41	64	59	56	47	59	39
	R^2	0.04	0.37	0.39	0.62	0.65	-0.16	0.44	0.05	0.62	0.07	0.21	0.3	0.5	0.21	0.66
May	RMSE	75	58	53	32	31	48	43	60	37	73	57	53	43	60	37
	R^2	-0.27	0.23	0.35	0.76	0.78	0.47	0.57	0.17	0.68	-0.22	0.26	0.35	0.58	0.17	0.69
		All			All			All			All			All		
All	RMSE	58			44			50			60			46		
	R^2	0.24			0.55			0.43			0.19			0.51		

Heading: 200° — TRAINING

Model:		R1			R2			M1			M2			M3		
VALIDATION		Mar	Apr	May	Mar	Apr	May	Mar	Apr	May	Mar	Apr	May	Mar	Apr	May
Mar	RMSE	35	49	69	45	54	63	45	55	73	42	90	151	38	53	68
	R^2	0.72	0.45	-0.09	0.54	0.32	0.1	0.55	0.31	-0.22	0.59	-0.85	-4.2	0.67	0.36	-0.06
Apr	RMSE	54	40	42	39	45	50	42	42	54	50	51	85	39	41	51
	R^2	0.34	0.64	0.59	0.64	0.54	0.42	0.6	0.59	0.33	0.44	0.41	-0.63	0.65	0.61	0.41
May	RMSE	75	55	46	43	40	42	51	40	45	71	51	53	49	40	43
	R^2	-0.27	0.3	0.51	0.58	0.64	0.61	0.41	0.63	0.55	-0.16	0.41	0.35	0.46	0.64	0.57
		All			All			All			All			All		
All	RMSE	49			45			41			55			39		
	R^2	0.46			0.53			0.61			0.3			0.65		

Colour coding by RMSE_{INS} [tons/ha]: ≤ 37 ⟷ ≥ 185

TABLE V

RESULTS OF **TOPOGRAPHIC VALIDATION** OF MODELS 1–6 IN TERMS OF RMSE (TONS/HA) AND R^2 (IN PARENTHESES). COLOUR CODING BY RMSE RELATIVE MEAN BIOMASS (94 TONS/HA): WHITE FOR 20 % AND BELOW, BLACK FOR 100 % AND ABOVE.

	Model:	R1	R2	M1	M2	M3	M4
TRAINING HEADING: 43°							
VALID.:	43°	**36 (0.37)**	**30 (0.56)**	**30 (0.58)**	**34 (0.45)**	**31 (0.55)**	**33 (0.48)**
	134°	**35 (0.31)**	**31 (0.48)**	**29 (0.53)**	**37 (0.23)**	**29 (0.52)**	**33 (0.39)**
	314°	**35 (0.26)**	**36 (0.22)**	**31 (0.42)**	**37 (0.19)**	**34 (0.34)**	**37 (0.2)**
	358°	**40 (0.3)**	**32 (0.55)**	**32 (0.56)**	**40 (0.32)**	**38 (0.37)**	**39 (0.36)**
	All	**36 (0.3)**	**33 (0.41)**	**30 (0.5)**	**37 (0.25)**	**32 (0.45)**	**35 (0.34)**
TRAINING HEADING: 134°							
VALID.:	43°	**43 (0.1)**	**37 (0.33)**	**30 (0.58)**	**43 (0.11)**	**30 (0.57)**	**30 (0.56)**
	134°	**38 (0.18)**	**31 (0.47)**	**29 (0.52)**	**38 (0.18)**	**30 (0.51)**	**30 (0.48)**
	314°	**40 (0.07)**	**35 (0.26)**	**34 (0.33)**	**39 (0.08)**	**35 (0.26)**	**34 (0.3)**
	358°	**45 (0.11)**	**42 (0.25)**	**38 (0.36)**	**45 (0.11)**	**40 (0.3)**	**39 (0.35)**
	All	**40 (0.13)**	**34 (0.36)**	**32 (0.45)**	**40 (0.14)**	**33 (0.41)**	**33 (0.42)**
TRAINING HEADING: 314°							
VALID.:	43°	**37 (0.35)**	**31 (0.55)**	**27 (0.67)**	**34 (0.46)**	**26 (0.67)**	**27 (0.64)**
	134°	**35 (0.31)**	**35 (0.31)**	**31 (0.47)**	**44 (-0.08)**	**37 (0.25)**	**28 (0.57)**
	314°	**36 (0.25)**	**29 (0.52)**	**28 (0.55)**	**44 (-0.14)**	**42 (-0.03)**	**30 (0.47)**
	358°	**41 (0.29)**	**31 (0.59)**	**31 (0.57)**	**42 (0.25)**	**42 (0.24)**	**40 (0.31)**
	All	**36 (0.29)**	**32 (0.44)**	**29 (0.53)**	**43 (0)**	**38 (0.2)**	**30 (0.51)**
TRAINING HEADING: 358°							
VALID.:	43°	**37 (0.35)**	**32 (0.52)**	**31 (0.53)**	**35 (0.43)**	**33 (0.47)**	**34 (0.43)**
	134°	**35 (0.31)**	**32 (0.42)**	**31 (0.47)**	**37 (0.23)**	**32 (0.44)**	**33 (0.39)**
	314°	**36 (0.25)**	**38 (0.16)**	**32 (0.38)**	**37 (0.18)**	**34 (0.31)**	**36 (0.22)**
	358°	**41 (0.29)**	**33 (0.53)**	**32 (0.55)**	**40 (0.32)**	**39 (0.36)**	**39 (0.34)**
	All	**36 (0.29)**	**34 (0.36)**	**32 (0.46)**	**37 (0.25)**	**33 (0.39)**	**35 (0.34)**
TRAINING HEADING: All							
VALID.:	43°	**38 (0.3)**	**31 (0.53)**	**30 (0.56)**	**36 (0.37)**	**31 (0.54)**	**32 (0.53)**
	134°	**36 (0.29)**	**30 (0.51)**	**29 (0.52)**	**36 (0.27)**	**30 (0.5)**	**31 (0.47)**
	314°	**36 (0.23)**	**35 (0.28)**	**32 (0.4)**	**36 (0.22)**	**34 (0.33)**	**34 (0.31)**
	358°	**42 (0.25)**	**33 (0.52)**	**33 (0.53)**	**40 (0.29)**	**38 (0.37)**	**38 (0.38)**
	All	**37 (0.27)**	**32 (0.44)**	**31 (0.49)**	**37 (0.27)**	**32 (0.44)**	**33 (0.42)**

Colour coding by RMSE_{INS} [tons/ha]: ≤ 19 $\longleftrightarrow$ ≥ 94

TABLE VI

RESULTS OF **FLAT-TO-TOPOGRAPHIC VALIDATION** OF MODELS 1–6 IN TERMS OF RMSE (TONS/HA) AND R^2 (IN PARENTHESES). COLOUR CODING BY RMSE RELATIVE MEAN BIOMASS (94 TONS/HA): WHITE FOR 20 % AND BELOW, BLACK FOR 100 % AND ABOVE.

	Model:	R1	R2	M1	M2	M3	M4
	TRAINING DATA: March, both headings						
VALID.:	43°	68 (-1.19)	75 (-1.69)	62 (-0.81)	71 (-1.41)	60 (-0.69)	48 (-0.12)
	134°	63 (-1.21)	63 (-1.2)	57 (-0.79)	66 (-1.45)	55 (-0.68)	48 (-0.29)
	314°	66 (-1.55)	68 (-1.76)	58 (-0.99)	69 (-1.81)	57 (-0.91)	51 (-0.54)
	358°	69 (-1.05)	74 (-1.39)	61 (-0.63)	72 (-1.24)	60 (-0.53)	51 (-0.1)
	All	65 (-1.3)	67 (-1.45)	58 (-0.83)	68 (-1.53)	56 (-0.74)	49 (-0.33)
	TRAINING DATA: April, both headings						
VALID.:	43°	62 (-0.85)	73 (-1.51)	53 (-0.36)	67 (-1.15)	51 (-0.26)	41 (0.21)
	134°	57 (-0.8)	59 (-0.92)	48 (-0.29)	61 (-1.11)	46 (-0.21)	40 (0.11)
	314°	59 (-1.07)	64 (-1.42)	50 (-0.46)	64 (-1.43)	48 (-0.38)	43 (-0.1)
	358°	63 (-0.73)	72 (-1.23)	54 (-0.24)	68 (-1)	52 (-0.16)	45 (0.13)
	All	59 (-0.88)	63 (-1.18)	50 (-0.35)	64 (-1.2)	48 (-0.26)	42 (0.06)
	TRAINING DATA: May, both headings						
VALID.:	43°	59 (-0.68)	70 (-1.35)	50 (-0.18)	64 (-0.94)	46 (-0.02)	35 (0.43)
	134°	54 (-0.6)	55 (-0.67)	45 (-0.11)	58 (-0.85)	42 (0.02)	35 (0.32)
	314°	56 (-0.85)	61 (-1.2)	46 (-0.26)	60 (-1.14)	44 (-0.14)	38 (0.12)
	358°	60 (-0.57)	70 (-1.1)	51 (-0.1)	64 (-0.8)	48 (0.02)	42 (0.23)
	All	56 (-0.68)	60 (-0.96)	46 (-0.16)	60 (-0.94)	44 (-0.04)	37 (0.26)
	TRAINING DATA: All dates, both headings						
VALID.:	43°	63 (-0.91)	70 (-1.36)	53 (-0.33)	66 (-1.05)	50 (-0.2)	38 (0.3)
	134°	58 (-0.87)	57 (-0.8)	48 (-0.28)	60 (-1.02)	46 (-0.16)	38 (0.18)
	314°	60 (-1.16)	63 (-1.31)	49 (-0.43)	63 (-1.32)	47 (-0.33)	42 (-0.03)
	358°	64 (-0.79)	70 (-1.11)	53 (-0.22)	66 (-0.91)	51 (-0.11)	44 (0.18)
	All	60 (-0.95)	61 (-1.06)	49 (-0.32)	62 (-1.1)	47 (-0.21)	40 (0.12)

Colour coding by RMSE_{INS} [tons/ha]: ≤ 19 $\longleftrightarrow$ ≥ 94

TABLE VII

RESULTS OF **TOPOGRAPHIC-TO-FLAT VALIDATION** OF MODELS 1–6 IN TERMS OF RMSE (TONS/HA) AND R^2 (IN PARENTHESES). COLOUR CODING BY RMSE RELATIVE MEAN BIOMASS (185 TONS/HA): WHITE FOR 20 % AND BELOW, BLACK FOR 100 % AND ABOVE.

	Model:	R1	R2	M1	M2	M3	M4
		TRAINING DATA: All headings					
VAL. 179°:	Mar	>200 (-12.25)	56 (0.29)	100 (-1.28)	>200 (-36.78)	>200 (-12.37)	59 (0.22)
	Apr	157 (-4.61)	59 (0.2)	64 (0.05)	>200 (-15.8)	180 (-6.37)	41 (0.61)
	May	123 (-2.48)	48 (0.48)	86 (-0.7)	>200 (-9.66)	175 (-5.98)	41 (0.62)
	All	181 (-6.45)	55 (0.32)	85 (-0.64)	>200 (-20.75)	>200 (-8.24)	48 (0.48)
		TRAINING DATA: All headings					
VAL. 200°:	Mar	187 (-6.78)	74 (-0.22)	68 (-0.03)	>200 (-21.2)	198 (-7.77)	46 (0.54)
	Apr	137 (-3.2)	71 (-0.11)	58 (0.25)	>200 (-11.6)	178 (-6.06)	40 (0.64)
	May	88 (-0.73)	62 (0.13)	58 (0.26)	157 (-4.48)	147 (-3.78)	41 (0.63)
	All	143 (-3.57)	69 (-0.07)	61 (0.16)	>200 (-12.43)	176 (-5.87)	42 (0.6)
		TRAINING DATA: All headings					
VAL. both:	Mar	>200 (-8.42)	69 (-0.06)	79 (-0.41)	>200 (-25.88)	>200 (-9.15)	50 (0.44)
	Apr	144 (-3.62)	67 (-0.01)	60 (0.19)	>200 (-12.84)	179 (-6.13)	41 (0.63)
	May	100 (-1.26)	58 (0.24)	68 (-0.03)	177 (-6.04)	156 (-4.44)	41 (0.63)
	All	156 (-4.43)	65 (0.05)	70 (-0.08)	>200 (-14.92)	184 (-6.57)	44 (0.57)

Colour coding by RMSE_{INS} [tons/ha]: ≤ 37 $\longleftrightarrow$ ≥ 185

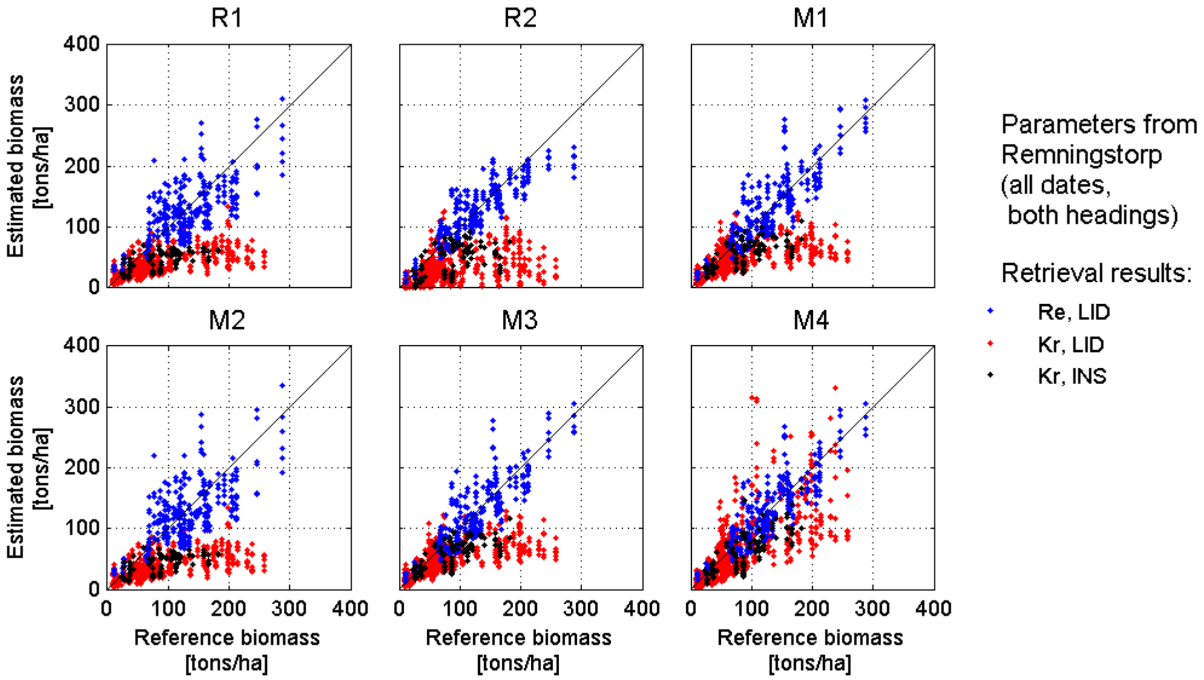

Fig. 7. Comparison of the six evaluated models: training on Remningstorp and validation on Krycklan.

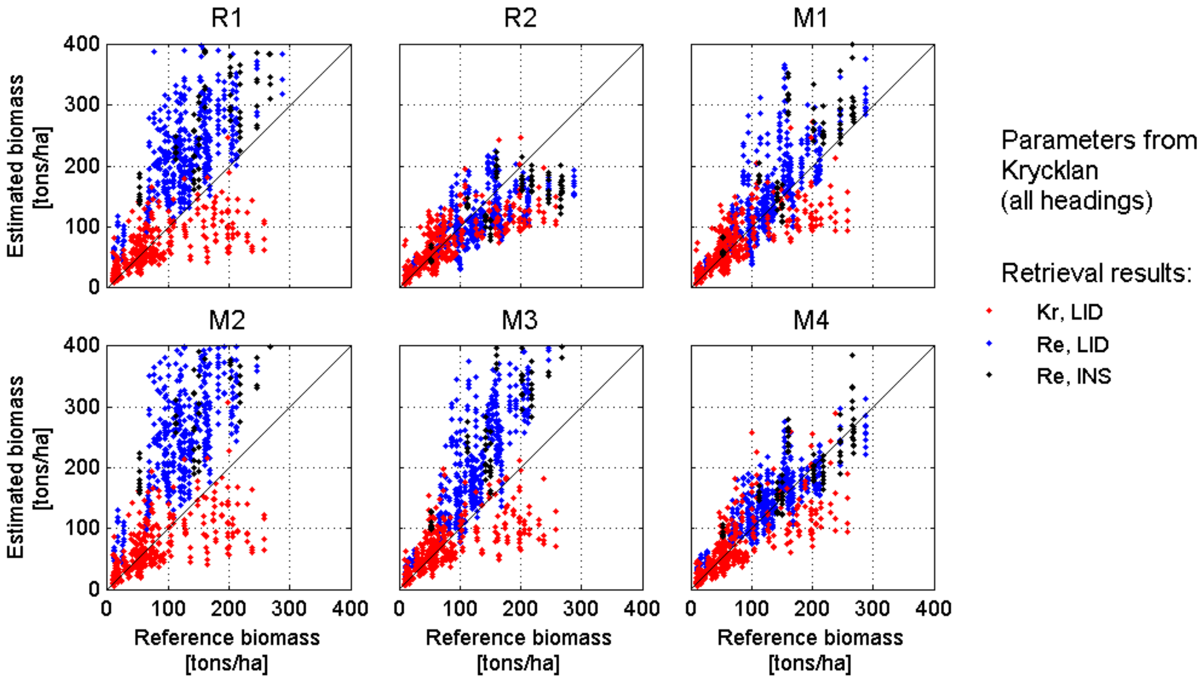

Fig. 8. Comparison of the six evaluated models: training on Krycklan and validation on Remningstorp.

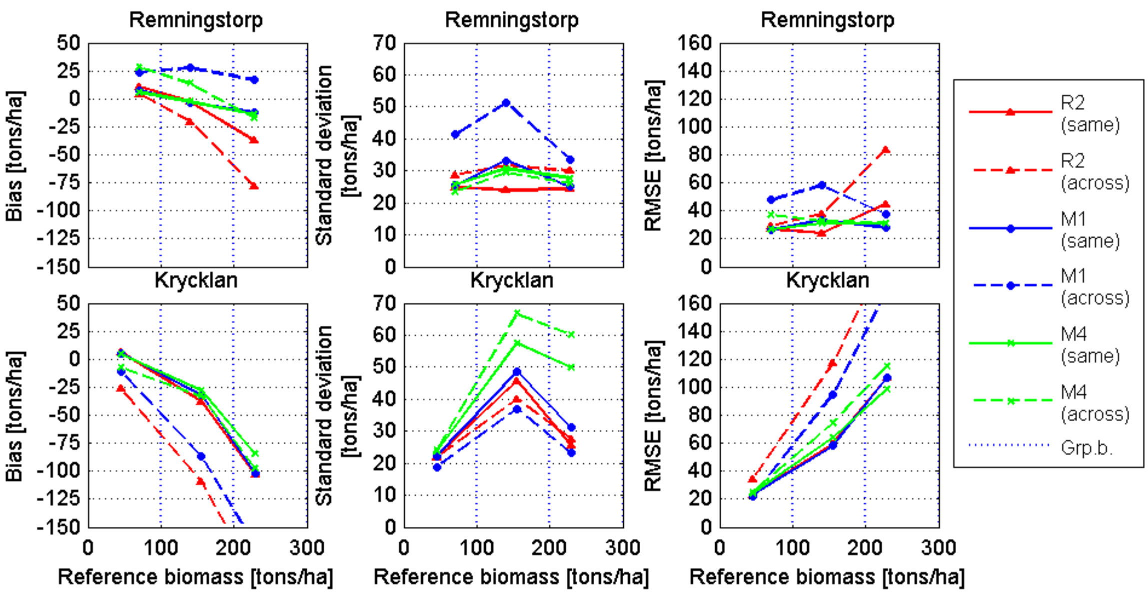

Fig. 9. Three different types of model errors are here plotted versus biomass: bias to the left, standard deviation of the estimation error in the middle, and RMSE to the right, as defined in Eq. (9)–Eq. (11). Only models (R2), (M1), and (M4) are compared. Model parameters as in Table III were used. ”Same” means that the model parameters estimated for the same site were used. ”Across” means that the model parameters estimated for the other site were used. LID-stands were used and averaging was done in three intervals: 0–100 tons/ha, 100–200 tons/ha, and 200–300 tons/ha. The interval borders are plotted in blue dashed lines. The number of data points in each group is at least 50. Note: some lines may cover each other.

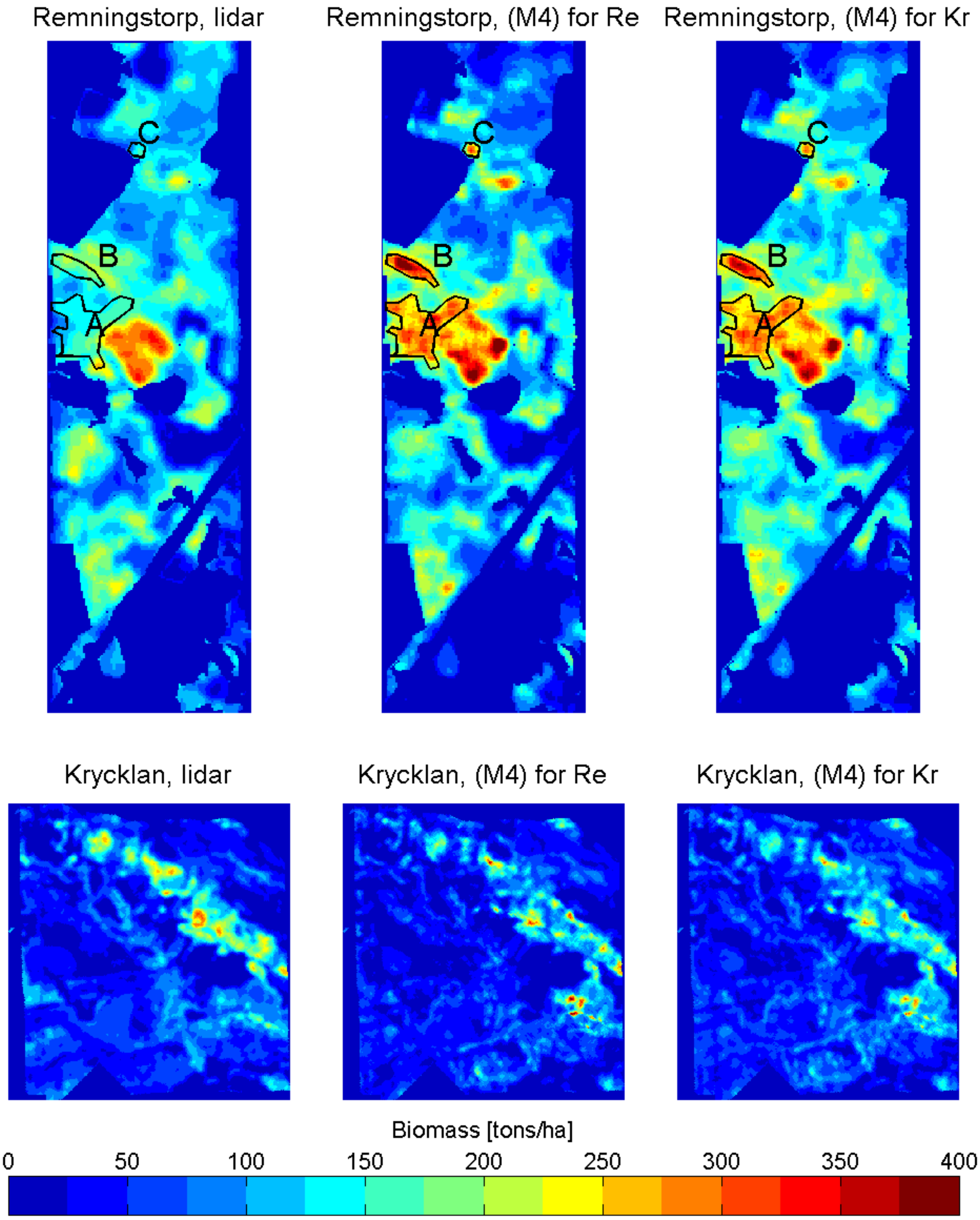

Fig. 10. Extracted biomass maps for Remningstorp and Krycklan. Biomass maps are quantised in intervals of 25 tons/ha. Model (M4) was used to create the maps. For Remningstorp, the north direction is upwards. All Krycklan-maps have been rotated by 45° counter-clockwise for better viewing and the north east direction is upwards. In all images, the resolution is $70\,\text{m} \times 70\,\text{m}$ and the pixel size is $10\,\text{m} \times 10\,\text{m}$. The size of the imaged region is $3700\,\text{m} \times 1130\,\text{m}$ for Remningstorp and $3450\,\text{m} \times 3270\,\text{m}$ for Krycklan. The scales are the same in both x- and y-direction. Three regions of interest discussed in Sec. IV-F are also marked and discussed in Sec. IV-F.

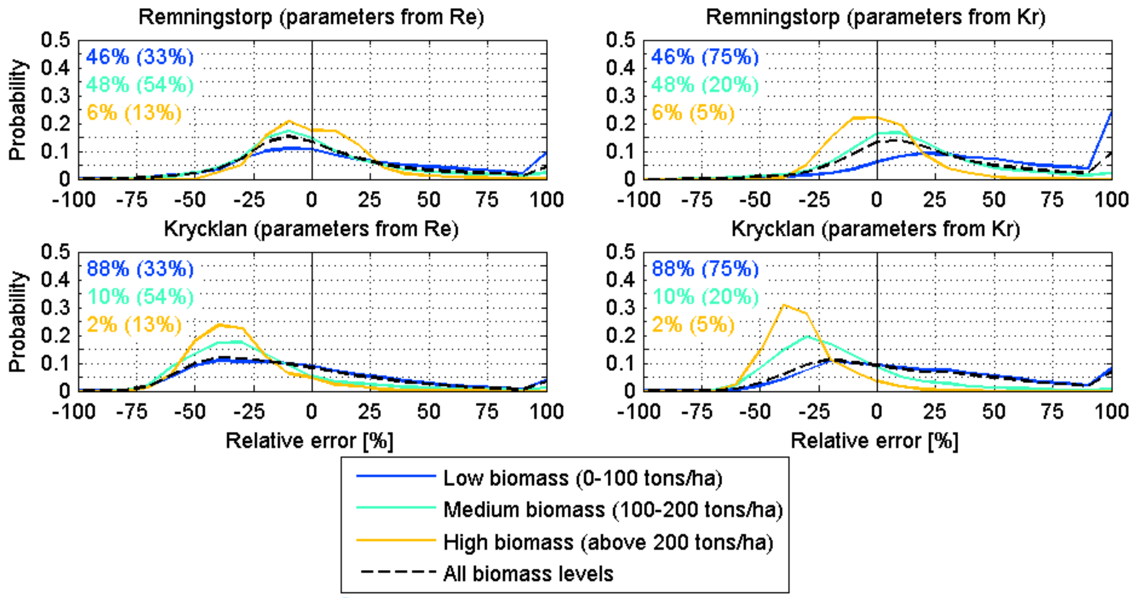

Fig. 11. Probability distributions for the relative difference between the lidar maps and the maps created using (M4) and SAR data are plotted here. Four curves are plotted, one for each biomass group (0–100 tons/ha, 100–200 tons/ha, and above 200 tons/ha), and one for all biomass levels. The distribution of the different groups among the image pixels are shown as percentage values in the upper left corner of each plot. In parentheses, the corresponding values for the training data are shown.

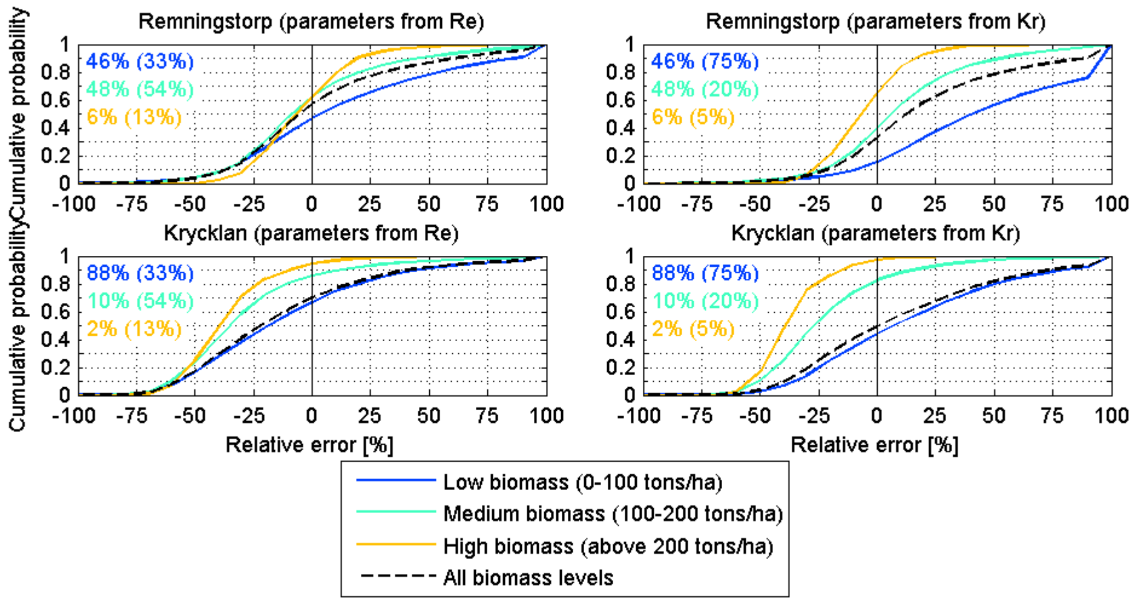

Fig. 12. Cumulative distributions for the relative difference between the lidar maps and the maps created using (M4) and SAR data are plotted here. Four curves are plotted, one for each biomass group (0–100 tons/ha, 100–200 tons/ha, and above 200 tons/ha), and one for all biomass levels. The distribution of the different groups among the image pixels are shown as percentage values in the upper left corner of each plot. In parentheses, the corresponding values for the training data are shown.

Paper B

A Hybrid Model for Interferometric and Polarimetric P-band SAR Imaging of Forests

Authors:

M. J. Soja and L. M. H. Ulander

Status:

In Proceedings for "PolInSAR 5th International Workshop on Science and Applications of SAR Polarimetry and Polarimetric Interferometry", Frascati, Italy, 24–28 January 2011 (ESA SP-695, March 2011).

A HYBRID MODEL FOR INTERFEROMETRIC AND POLARIMETRIC P-BAND SAR IMAGING OF FORESTS

Maciej J. Soja[1] **and Lars M. H. Ulander**[2]

[1]*Chalmers University of Technology, SE-412 96 Göteborg, Sweden*
[2]*Swedish Defence Research Agency, SE-581 11 Linköping, Sweden*

ABSTRACT

In this paper, a forward model for extended covariance matrix prediction for boreal and hemi-boreal forest in P-band SAR is presented. The main product is the extended covariance matrix scaled to sigma nought on the diagonal. The input parameters consist of basic radar setup, topography, forest biome, biomass, and some model parameters. Backscatter intensities for HH, VV, and HV channels are predicted from biomass using regression based on BioSAR 2007 campaign data. The phase of the correlation between the HH and VV channels is found to be proportional to biomass and is also modelled by a regression based on BioSAR 2007 data. The coherence of HH and VV channels is found to be unrelated to biomass and is chosen to be modelled as a stochastic variable. The correlation of any co-polarized channel with HV is set to 0. The interferometric correlation values for the three channels are modelled using volume over ground (VoG) model, which is a combination of random volume over ground (RVoG), oriented volume over ground (OVoG), and elevated random volume over ground (ERVoG) models.

The forward model is also evaluated against SAR data from the BioSAR 2007 campaign. Three intensity images and one complex polarimetric correlation image are created for Remningstorp (site of BioSAR 2007) from existing biomass map, DEM, and flight path information. These images are compared with the images acquired with ESAR during the BioSAR 2007 campaign and the similarities and differences are discussed. The presented forward model is able to predict backscatter with an RMSE of 1.35 dB (HV), 1.77 dB (VV), and 1.92 dB (HH). Polarimetric correlation can be predicted with magnitude and phase RMSE equal to 0.08 and 16.3 deg, respectively. A qualitative evaluation of the interferometric part is also done and it is concluded that a good setup of model parameters is neccessary to get satisfactory results.

1. INTRODUCTION

In view of the proposed ESA Earth Explorer BIOMASS mission, a polarimetric interferometric forward model for P-band forest imaging is developed. The model predicts the 6x6 extended covariance matrix C_6 and requires only a limited number of input variables such as: relevant bio-physical parameters (forest biomass and/or forest height, forest type, surface slopes), instrument parameters (incident angle, etc), and mission parameters (such as temporal and spatial baselines). The model simulates all the mechanisms that are exploited by the different biomass retrieval methods (intensity-based retrieval, PolInSAR height inversion, and polarimetric decomposition-based biomass retrieval).

Three BioSAR campaigns have been carried out as parts of the BIOMASS project: BioSAR 2007 (Hajnsek et al. 2008; Sandberg et al. 2009), BioSAR 2008 (Hajnsek et al. 2009; Soja et al. 2010), and the most recent BioSAR 2010 (at the time of writing, processed SAR data are not yet available). The main goal of these campaigns is to examine issues such as seasonal change and topography variation influence on SAR data in boreal and hemi-boreal forests of Sweden.

This text is structured in the following way: first, a short presentation of the experimental data used in this study is given in Sec. 2. In Sec. 3, the forward model is presented. First, the required product and the specified input variables are defined, and then each separate part of the forward model is described. In Sec. 4, the model is put into work and some sample results are presented, compared with ESAR data, and evaluated. Finally, Sec. 5 evaluates the whole study and pinpoints the most important observations. This text describes the latest implementation of the model. Some features, such as temporal decorrelation, different biome types, and different profile functions, will be described in the text, but not evaluated due to the limited character of this paper. Nevertheless, they will be available for the final delivery of the model. The model is suitable for extended covariance matrix prediction for boreal and hemi-boreal forests with standwise biomass range 0-300 tons/ha with an approximate resolution cell size of 0.5 ha.

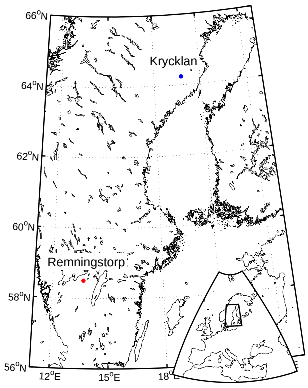

Figure 1. The two test sites in Sweden used for the three BioSAR campaigns.

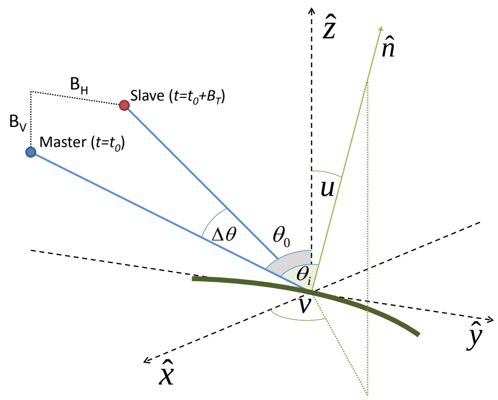

Figure 2. The geometry and nomenclature used throughout this paper. $\vec{n}$ is the normal of the ground surface.

2. EXPERIMENTAL DATA

In this study, P-band SAR data and ground truth data from Remningstorp in southern Sweden is used. A short description of the used data will be given below. A detailed description of the BioSAR 2007 campaign can be found in Hajnsek et al. (2008); Sandberg et al. (2009). Limited stand-wise forest data from Krycklan in Sweden is also used.

2.1. Test Site

Remningstorp is located in southern Sweden (58°30'N, 13°40'E, see Fig. 1) and covers about 1200 ha of productive forest land. The forest is classified as hemi-boreal. The dominant tree species are Norway spruce, Scots pine, and birch. The dominant soil type is till with a field layer consisting of different herbs, blueberry and narrow thinned grass. In denser old spruce stands the field layer is absent. The ground elevation is moderately varying between 120 and 145 m above sea level.

2.2. Field and Laser Scanning Data

There are two sets of field data available for Remningstorp. The first set consists of 10 stands, each of size 80x80 m^2, where every single tree with a diameter at breast height larger than 5 cm was recorded between 2007 and 2008. Stem diameter together with tree species, stem tilt and tree position were also recorded. About 10% of the trees in each stand had also their height measured. The stand biomass was estimated from stem diameter and tree height measurements using suitable allometric formulas with high accuracy.

The second set of Remningstorp ground truth data consists of 58 stands with areas between 0.5 and 9.4 ha. A stem volume map for Remningstorp was created from high-resolution canopy elevation models acquired with lidar scanning. Highly accurate biomass estimates for the 58 stands were computed from the stem volume map with the aid of optical classification of species and well-established conversion factors. A little less accurate biomass map for Remningstorp was also created from the stem volume map using one single conversion factor (see Fig. 7). This map was used as input for the model, see Sec. 4.

2.3. SAR Data

Fully polarimetric and interferometric P-band SAR images of Remningstorp were acquired using DLR's Experimental SAR (ESAR) platform at three dates in 2007: March 9th, March 31st to April 2nd, and May 2nd. For simplicity, the three data sets will be called March, April, and May data, respectively. For each date, geocoded images from two headings: 179° (1 image) and 200° (2 images) were created. In this paper, only the 200-degree heading is used since it is the only one to cover all available stands. Also, a set of polarimetric-interferometric images in slant range geometry were acquired for the 200°-heading at horizontal spatial baselines between 10 and 80 meters and temporal baselines of approximately 0, 1, or 2 months.

3. FORWARD MODEL

3.1. Extended Covariance Matrix

The quantity to be modelled by this forward model is the extended covariance matrix called C_6. Having two scattering vectors (for two geometries, or "master" and "slave" images, as shown in Fig. 2) as in Eq. (1) and Eq.

Table 1. Input variables to the forward model.

Var.:	**Description [unit]:**
General setup	
TRS	training data set used
Radar system setup	
ν_c	centre frequency [Hz]
H	altitude [m]
θ_0	global angle of incidence [deg]
B_H	horizontal baseline [m]
B_V	vertical baseline [m]
B_T	temporal baseline [days]
Ground topography	
h_0	ground height [m]
u	ground slope [deg]
v	slope direction [deg]
Forest parameters	
h_{100}	forest height (optional) [m]
h_c	canopy elevation [% of h_{100}]
$\mathcal{B}$	forest biomass [tons/ha]
RVoG model parameters	
FID	profile type (1: exponential, 2: Gaussian)
μ_{HH}	ground-to-volume ratio for HH
μ_{VV}	ground-to-volume ratio for VV
μ_{HV}	ground-to-volume ratio for HV
Exponential profile setup	
α_{HH}	extinction on top of the layer for HH [dB/m]
α_{VV}	extinction on top of the layer for VV [dB/m]
β	extinction change with height [dB/m^2]
Gaussian profile setup	
δ	scattering center mean elevation [% of h_{100}]
χ	scattering center standard deviation [% of h_{100}]
Temporal decorrelation setup	
τ_v	time constant for temporal decorrelation of volume [days]
τ_s	time constant for temporal decorrelation of surface [days]

(2):

$$\vec{k}_1 = [S_{1,\mathrm{HH}} \;\; S_{1,\mathrm{VV}} \;\; S_{1,\mathrm{HV}}]^T , \tag{1}$$

$$\vec{k}_2 = [S_{2,\mathrm{HV}} \;\; S_{2,\mathrm{VV}} \;\; S_{2,\mathrm{HV}}]^T , \tag{2}$$

where $S_{i,\mathrm{PQ}}$ is the complex scattering amplitude for image i and polarisation mode PQ, and ^{T} is the transpose operator, C_6 can be acquired by creating outer product combinations of these two as shown in Eq. (3):

$$\begin{aligned} C_6 &= 4\pi \begin{bmatrix} \langle \vec{k}_1 \cdot \vec{k}_1^H \rangle & \langle \vec{k}_1 \cdot \vec{k}_2^H \rangle \\ \langle \vec{k}_2 \cdot \vec{k}_1^H \rangle & \langle \vec{k}_2 \cdot \vec{k}_2^H \rangle \end{bmatrix} = \\ &= 4\pi \begin{bmatrix} T_{11} & \Omega_{12} \\ \Omega_{12}^H & T_{22} \end{bmatrix}, \end{aligned} \tag{3}$$

where C_6 has been scaled to give σ^0 on diagonal and ^{H} is the Hermitian transpose (the transpose of the complex conjugate). Using the fact that the covariance of any co-polarised channel with the cross-polarised channel is (ideally) zero, polarimetric and interferometric elements of C_6 can now be re-written as shown in Eq. (4) and Eq. (5):

$$T_{ii} = \begin{bmatrix} \sigma^0_{i,\mathrm{HH}} & \rho_i \cdot A_i & 0 \\ \rho_i^* \cdot A_i & \sigma^0_{i,\mathrm{VV}} & 0 \\ 0 & 0 & \sigma^0_{i,\mathrm{HV}} \end{bmatrix} \tag{4}$$

which is a Hermitian matrix, and

$$\Omega_{12} = \begin{bmatrix} \widetilde{\gamma}_{\mathrm{HH}} \cdot B_{\mathrm{HH}} & \omega_{12} \cdot C & 0 \\ \omega_{21} \cdot C & \widetilde{\gamma}_{\mathrm{VV}} \cdot B_{\mathrm{VV}} & 0 \\ 0 & 0 & \widetilde{\gamma}_{\mathrm{HV}} \cdot B_{\mathrm{HV}} \end{bmatrix}, \tag{5}$$

which is non-Hermitian and where $i = 1, 2$ is the index of the studied image ("master" or "slave" in Fig. 2). The diagonal elements of T_{ii} are scaled to sigma nought:

$$\sigma^0_{i,\mathrm{PQ}} = 4\pi \left\langle |S_{i,\mathrm{PQ}}|^2 \right\rangle ,$$

and they also give the following elements in Eq. (4) and Eq. (5):

$$\begin{aligned} A_i &= \sqrt{\sigma^0_{i,\mathrm{VV}} \cdot \sigma^0_{i,\mathrm{HH}}}, \\ B_{\mathrm{PQ}} &= \sqrt{\sigma^0_{1,\mathrm{PQ}} \cdot \sigma^0_{2,\mathrm{PQ}}}, \\ C &= \sqrt{\sigma^0_{1,\mathrm{HH}} \cdot \sigma^0_{2,\mathrm{VV}}}. \end{aligned}$$

Two complex valued quantities that need to be modelled are:

$$\rho_i = \frac{\langle S_{i,\mathrm{HH}} \cdot S_{i,\mathrm{VV}}^* \rangle}{\sqrt{\left\langle |S_{i,\mathrm{HH}}|^2 \right\rangle \left\langle |S_{i,\mathrm{VV}}|^2 \right\rangle}}, \tag{6}$$

$$\widetilde{\gamma}_{\mathrm{PQ}} = \frac{\langle S_{1,\mathrm{PQ}} \cdot S_{2,\mathrm{PQ}}^* \rangle}{\sqrt{\left\langle |S_{1,\mathrm{PQ}}|^2 \right\rangle \left\langle |S_{2,\mathrm{PQ}}|^2 \right\rangle}}, \tag{7}$$

which represent the polarimetric complex correlation and the interferometric complex correlation, respectively. Note, that $\widetilde{\gamma}_{\mathrm{PQ}}$ is the correlation of two interferometric images acquired in the same polarimetric mode. The symbolism has been minimised for simplicity.

The non-diagonal elements in Eq. (5), ω_{12} and ω_{21}, represent the correlation between HH and VV channels at both ends of the baseline. In this model, they will not be predicted using dedicated functions, but their values will be derived from the expressions for ρ_i and $\widetilde{\gamma}_{\mathrm{PQ}}$. The details will be presented in Sec. 3.6.

3.2. Input Parameters

The parameters which have been chosen to be required from the user are all shown in Tab. 1. Some of the parameters, together with the geometry of the problem, are visually presented in Fig. 2. The forest height indicator used in this text will be the h_{100}-parameter, which is defined as the mean height of the 100 tallest trees per hectare.

3.3. Backscatter Intensity Modelling

Backscatter intensity is chosen to be modelled by the following function:

$$\widehat{[\sigma^0_{\mathrm{PQ}}]}_{dB} = a_{\mathrm{PQ}} + b_{\mathrm{PQ}} \log_{10} \mathcal{B} + \epsilon_{\mathrm{PQ}}, \qquad (8)$$

where PQ is either HH, VV, or HV, and ϵ_{PQ} is a normally distributed additive error with mean 0 and standard deviation ς_{PQ}. In order to obtain suitable parameter values in (8), the functions were fitted to the 200-degree heading BioSAR data in the following constellations:

- $\mathsf{TRS} = 0$: all available data,
- $\mathsf{TRS} = 1$: March data only,
- $\mathsf{TRS} = 2$: April data only,
- $\mathsf{TRS} = 3$: May data only.

The resulting parameter values are presented in Tab. 2. In Fig. 3, the fitted lines are plotted together with the corresponding training data. The same model with the same error representation is used for both “master” and “slave” images.

3.4. Polarimetric Correlation Modelling

The cross-channel complex correlation ρ_i is modelled by the following functions derived from empirical observations in BioSAR 2007 data:

$$\begin{aligned} |\widehat{\rho_i}| &= \overline{\rho} + \epsilon_\rho, , & (9) \\ \arg(\widehat{\rho_i}) &= a_\rho + b_\rho \cdot \mathcal{B} + \epsilon_{\psi_\rho}, & (10) \end{aligned}$$

where $\overline{\rho}$ is the mean value of the cross-channel coherence and the phase changes linearily with biomass $\mathcal{B}$. Both the magnitude and the phase of ρ_i are distorted by zero mean additive errors ϵ_ρ and ϵ_{ψ_ρ} with standard deviations ς_ρ and ς_{ψ_ρ}, respectively.

The model presented in (9) and (10) was derived from observations in BioSAR 2007 data. The model was fitted to the data in the same way as described in Sec. 3.3. In Fig. 4 the resulting curves are plotted together with the original data points. Values of the constant parameters in (9) and (10) can be found in Tab. 2. The same model with the same error representation is used for both “master” and “slave” images.

3.5. Interferometric Correlation Modelling

The interferometric contributions $\widetilde{\gamma}_{\mathrm{PQ}}$ (meaning the complex correlation values of two images with the same polarization mode but different geometries and/or acquisition times) are predicted by a combination of the classical random volume over ground model (RVoG, see Papathanassiou & Cloude (2001); Cloude & Papathanassiou (1998, 2003); Cloude (2010)), the elevated random volume over ground model (ERVoG), and the oriented volume over ground model (OVoG), both in the form presented in Garestier et al. (2008), with all the profile functions described in Garestier & Le Toan (2010). The model presented here will be simply called volume over ground model (VoG), as it includes elements of all the three established models.

The RVoG model predicts the complex correlation of a random volume of particles (of height h_V) situated directly above a coherently scattering ground. In ERVoG, the volume is allowed to have an elevation h_c above the ground, thus imitating a tree crown of thickness $h_V - h_c$. The OVoG model allows the particles inside the volume to have a predetermined orientation, thus allowing the attenuation to be polarization-dependent.

The VoG model presented here also includes exponential functions simulating the temporal decorrelation of volume and surface in a very much simplified manner:

$$\widetilde{\gamma}_{\mathrm{PQ}} = \mathrm{e}^{ik_z h_0} \cdot \frac{\widetilde{\gamma}_{v,\mathrm{PQ}} \cdot \mathrm{e}^{ik_z h_c} \cdot \mathrm{e}^{-\frac{B_T}{\tau_{vol}}} + \mu_{\mathrm{PQ}} \cdot \mathrm{e}^{-\frac{B_T}{\tau_s}}}{1 + \mu_{\mathrm{PQ}}}, \qquad (11)$$

where

$$k_z = \frac{4\pi \cdot \Delta\theta}{\lambda \sin\theta_i}$$

is the vertical wavenumber,

$$\widetilde{\gamma}_{v,\mathrm{PQ}} = \frac{\int_0^{h_V - h_c} f_{\mathsf{FID},\mathrm{PQ}}(z) \cdot \mathrm{e}^{ik_z z} \, \mathrm{d}z}{\int_0^{h_V - h_c} f_{\mathsf{FID},\mathrm{PQ}}(z) \, \mathrm{d}z} \qquad (12)$$

represents the correlation for a volume (“tree crown”) of thickness $h_V - h_c$ and a profile described by $f_{\mathsf{FID}}(z)$, and the other quantities are as defined in Fig. 2 and Tab. 1. Two main profiles presented in Garestier & Le Toan (2010) are:

$$f_{1,\mathrm{PQ}}(z) = \exp\left(\frac{2\sigma_{\mathrm{PQ}}(z) \cdot z}{\cos\theta_i}\right) \qquad (13)$$

and

$$f_{2,\mathrm{PQ}}(z) = \exp\left(-\frac{(z-\delta)^2}{2\chi^2}\right), \qquad (14)$$

where the first one is an exponential profile with height-dependent extinction coefficient $\sigma(z)$, and the second one is a Gaussian curve with mean δ and standard deviation χ. In Garestier & Le Toan (2010) three different types of $\sigma(z)$ are discussed, which all can be summarized as:

$$\sigma_{\mathrm{PQ}}(z) = \alpha_{\mathrm{PQ}} + \beta z, \qquad (15)$$

where polarization dependence of the α-parameter has been introduced as an extension of RVoG to OVoG. Parameter α should be specified among the other input parameters for both HH and VV polarisations, and α_{HV} is then simply:

$$\alpha_{\mathrm{HV}} = \frac{\alpha_{\mathrm{HH}} + \alpha_{\mathrm{VV}}}{2}. \qquad (16)$$

If $\beta = 0$, $\alpha_{\mathrm{HH}} = \alpha_{\mathrm{VV}}$, and $h_c = 0$, the classical RVoG model is used. The standard OVoG model can be obtained when $\beta = 0$ and $h_c = 0$. Likewise, the ERVoG

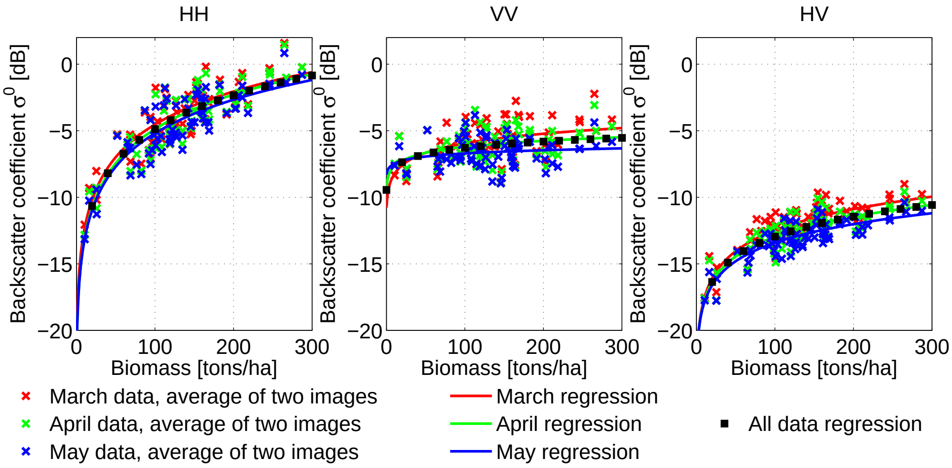

Figure 3. The model presented in (8) *was fitted to BioSAR data for each date separately, and for all dates together. The curves and data points are presented here.*

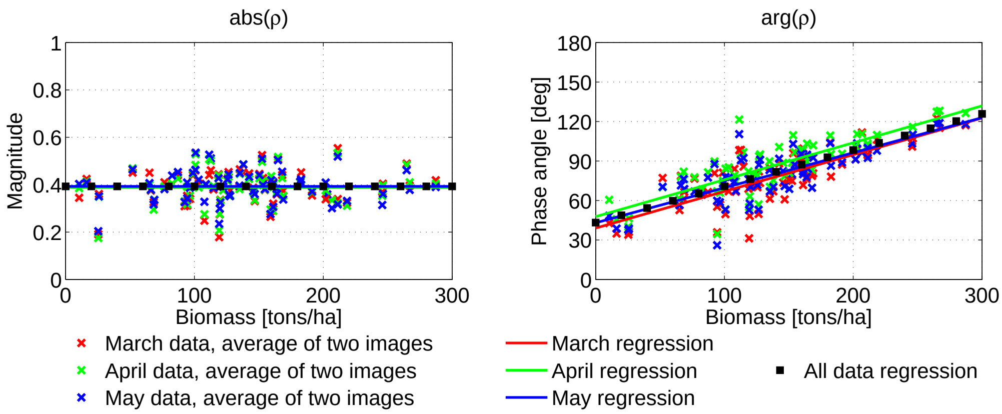

Figure 4. The model presented in (9) *and* (10) *was fitted to BioSAR 2007 data for each date separately and for all dates together. The fitted lines are presented here.*

model is obtained if $\beta = 0$, $h_c > 0$, and $\alpha_{\mathrm{HH}} = \alpha_{\mathrm{VV}}$. The integrals in Eq. (12) can be computed analytically (see Garestier & Le Toan (2010)).

The choice of the parameters h_c, B_T, τ_v, τ_s, and μ_{PQ}, together with the choice between one of the two profiles $f_1(z)$ and $f_2(z)$ (with the parameters α_{PQ} and β, or δ and χ therein) are all left to the user. Also, it is here assumed that

$$h_V \approx h_{100} \tag{17}$$

which has been shown to be quite a reliable approach (see for instance Hajnsek et al. (2008, 2009), where RVoG inversion gives h_V as a good estimate of h_{100}).

3.6. Non-diagonal Elements of Ω_{12}

The non-diagonal elements Ω_{12} will be modelled using the assumption that the combined decorrelation due to different polarizations *and* different acquisition points/time can be seen as a product of the polarimetric decorrelation and the interferometric decorrelation, that is:

$$\frac{\langle S_{i,\mathrm{PP}} \cdot S_{j,\mathrm{QQ}}{}^* \rangle}{\sqrt{\langle |S_{i,\mathrm{PP}}|^2 \rangle \langle |S_{j,\mathrm{QQ}}|^2 \rangle}} \approx \gamma_{pol} \cdot \gamma_{int} \tag{18}$$

which gives:

$$\omega_{12} \approx \gamma_{\mathrm{HH}} \cdot \rho_2 \approx \gamma_{\mathrm{VV}} \cdot \rho_1, \tag{19}$$

$$\omega_{21} \approx \gamma_{\mathrm{VV}} \cdot \rho_2^* \approx \gamma_{\mathrm{HH}} \cdot \rho_1^*, \tag{20}$$

where each ω has been re-written in two equivalent ways using the assumption in Eq. (18). In this forward model, the non-diagonal elements will be modelled in the following way:

$$\omega_{12} = \frac{\gamma_{\mathrm{HH}} \cdot \rho_2 + \gamma_{\mathrm{VV}} \cdot \rho_1}{2}, \tag{21}$$

$$\omega_{21} = \frac{\gamma_{\mathrm{HH}} \cdot \rho_1^* + \gamma_{\mathrm{VV}} \cdot \rho_2^*}{2}. \tag{22}$$

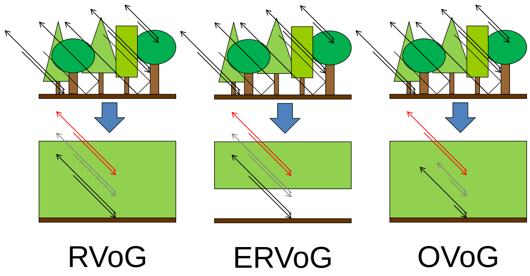

Figure 5. Random volume over ground model simulates complicated forest scattering as a combination of scattering from a random volume of height h_V and a coherently scattering surface. Coherence of different channels is simulated by taking volume and surface scattering in different proportions (different μ-values). Elevated random volume over ground (ERVoG) model allows the existence of a gap of width h_c between the volume and the ground. Oriented volume over ground (OVoG) introduces polarization-dependent attenuation in volume.

3.7. Biomass to Height Conversion

The volume over ground model requests the canopy height h_V as an input parameter. Since the assumption in Eq. (17) is used, h_{100} is going to be used as the volume height. Biomass and h_{100} can be related through the following allometric equation, which has been found valid for Remningstorp and Krycklan data:

$$\log_{10} h_{100} = a_h + b_h \log_{10} \mathcal{B} + \epsilon_h \qquad (23)$$

where a_h and b_h are parameters estimated using least-squares fitting to the available data, and ϵ_h is an additive error with zero mean and standard deviation ς_h. Using ground-measured values for h_{100} and $\mathcal{B}$ for Remningstorp and Krycklan (Hajnsek et al. 2009; Soja et al. 2010), these parameters can be estimated and a curve can be fitted, see Fig. 6. The estimated values for a_h, b_h and ς_h can be found in Tab. 2.

4. EVALUATION OF THE MODEL

The forward model described in this paper was evaluated using SAR data over Remningstorp acquired by the ESAR platform from DLR. One SAR image acquired in May at the 200-degree heading was used as reference. The previously mentioned lidar-based biomass map shown in Fig. 7 was inserted into the model. The ESAR images were down-sampled to fit the grid of the biomass map (pixel size: 10 m by 10 m). All presented maps are geo-coded to UTM33.

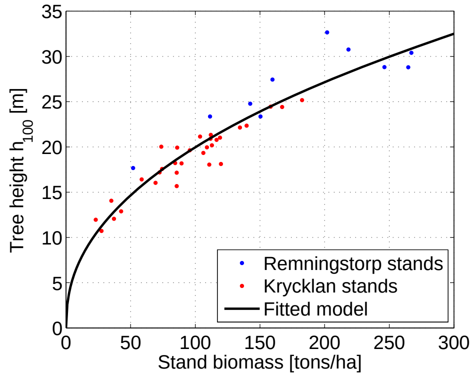

Figure 6. Allometric relation for biomass to height conversion. 10 stands in Remningstorp and 31 stands in Krycklan were used.

Table 2. Values of the parameters in models (8), (9), (10), *and* (23) *found by least-squares fitting to BioSAR data. ς_x is the standard deviation of the error ϵ_x (which has mean 0).*

	Training set used:			
Const.:	March	April	May	All
a_{HH}	-20.7625	-21.8742	-21.7738	-21.4701
b_{HH}	8.1223	8.5064	8.2956	8.3081
ς_{HH}	1.2599	1.3035	1.2748	1.3015
a_{VV}	-10.6582	-9.1717	-8.2603	-9.3634
b_{VV}	2.3590	1.4829	0.7784	1.5401
ς_{VV}	1.2843	1.1850	1.0778	1.2467
a_{HV}	-22.8652	-22.7809	-22.5807	-22.7423
b_{HV}	5.2002	4.9165	4.5876	4.9014
ς_{HV}	0.9088	0.8681	0.7472	0.9347
$\overline{\rho}$	0.3895	0.3886	0.3930	0.3904
ς_ρ	0.0714	0.0698	0.0669	0.0690
a_ρ	0.6815	0.8332	0.7509	0.7552
b_ρ	0.0049	0.0049	0.0046	0.0048
ς_{ψ_ρ}	0.2272	0.2137	0.2135	0.2272
a_h	N/A	N/A	N/A	0.4118
b_h	N/A	N/A	N/A	0.4441
ς_h	N/A	N/A	N/A	1.7213

4.1. Backscatter Intensity

The model was set to only use May data. In Fig. 8, the modelled SAR images are presented side-by-side with the original ESAR images. They are plotted as RGB images with HH as the red channel, VV as the green channel, and HV as the blue channel. Also, there are three bivariate (two-dimensional) histograms plotted to the right (one for each polarization).

The first, most obvious conclusion when comparing the two images is that the ESAR image shows many more small-scale effects such as border effects close to roads, forest boundaries, etc. This is an expected behaviour

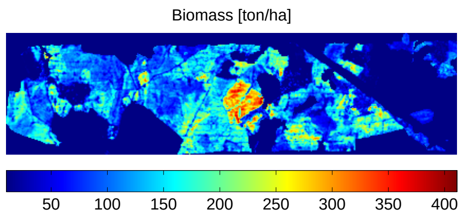

Figure 7. A laser scanning-derived biomass map with pixel size 10 m x 10 m was used as input to the forward model. The map has here been rotated 90° counterclockwise for space-saving reasons. Non-forested areas have been masked out.

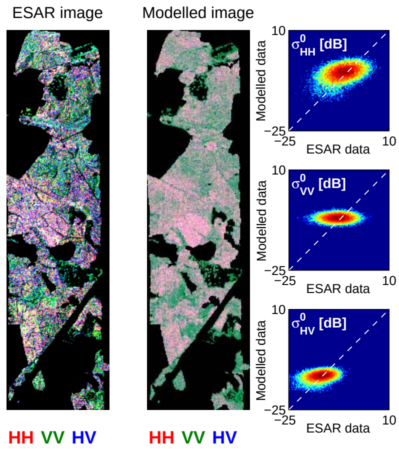

Figure 8. Simulation results for intensity modelling in Remningstorp.

since the model is developed for stand-wise data with stand areas above 0.5 ha. The resolution of the model can thus be approximated to 70 m x 70 m. Since the predicted images are on a grid of 10 m x 10 m, there are many effects unaccounted for. Nevertheless, the prediction of sigma nought backscatter shows good results on the bigger scale, see Fig. 8. Considering the fact that the conversion from stem volume map to biomass map was done in a rather simplified way using one constant only (independent of tree species), the results are certainly good on the stand level. The best prediction occurs for HV with a root-mean-square error of 1.35 dB, which has already been shown to give the best biomass correlation at P-band (Sandberg et al. 2009). HH gives higher error (1.92 dB) but still, both images show the same dynamic ranges. For VV, the knowledge of biomass is apparently not sufficient for satisfactory prediction of sigma nought — the dynamic range observed in ESAR data is far higher than the dynamic range of the model. Although the RMSE (1.77 dB) for VV is lower than for HH, there is no alignment of the data along the $y = x$-line.

Note: the presented RMSE errors were computed for modelled data based on biomass map *downsampled* to 70 m x 70 m pixels, which matches the smallest stand size in training data.

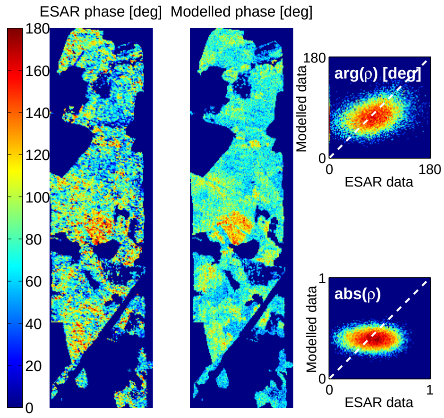

Figure 9. Simulation results for polarimetric correlation modelling.

4.2. Polarimetric Correlation

In Fig. 9 the results for prediction of the HH-VV-correlation are shown. As it was earlier observed, the magnitude of ρ was not found to be biomass-dependent and thus only phase images are shown. There is a good correlation of the ESAR image and the image computed by the forward model. In the histogram for the phase of ρ, good results with no visible bias are observed. The statistics of both images are very much alike. When it comes to the magnitude of ρ, the ESAR image shows higher dynamic range than the predicted image. Even though the magnitude of ρ is seemingly uncorrelated with biomass, there may be some other factors that introduce the dynamic range. One other difference observed in the images is the "graininess" of the ESAR image. This is most likely caused by the effects of downsampling after multilooking in correlation computing, where a window of 17 pixels in azimuth and 9 pixels in range was used for that purpose. This even enhances the earlier mentioned issues connected to different resolutions of the forward model and the available biomass map. Nevertheless, the prediction of ρ_i can be done with an error of approximately 0.08 in magnitude and $16°$ in phase.

4.3. Interferometric Correlation

The interferometric part of the forward model was also tested against ESAR data. As the second ESAR image, an image from the same date, but with an approximate horizontal baseline of 70 m, was used. The exact flight path information was provided to the forward model in form of θ_0 and k_z maps. The other radar and forest parameters were chosen to resemble the ESAR case as well

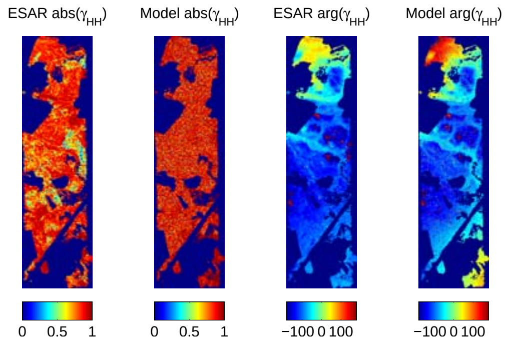

Figure 10. Correlation prediction results for HH.

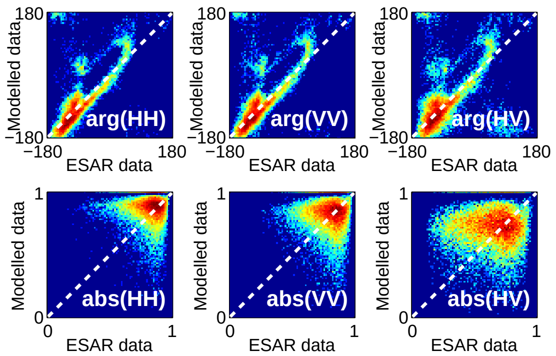

Figure 11. Correlation histograms.

as possible, based on information in Hajnsek et al. (2008). The height h_{100} was computed using Eq. (23). The unknown model parameters, mainly μ_{PQ} and the profile function with the parameters therein, were estimated using repetitive qualified guessing. In Fig. 10, an example of an interferometric correlation prediction is shown. In Fig. 11, histograms comparing modelled images with reference images for all three polarizations are shown. The phase resemblence is very good, mostly thanks to the detailed DEM provided to the model, but there are some issues in the regions corresponding to near and far range. The coherence values are in general well estimated, but the spread is big, and the spatial changes are not well reproduced. In the presented case, $h_c = 50\%$, $\mu_{\mathrm{HH}} = \mathcal{N}(10, 6^2)$, $\mu_{\mathrm{VV}} = \mathcal{N}(7, 4^2)$, $\mu_{\mathrm{HV}} = \mathcal{N}(4, 2^2)$, $\mathsf{FID} = 1$ and $\alpha_{\mathrm{HH}} = \alpha_{\mathrm{VV}} = 0.1$ dB/m. The fact, that the ground-to-volume ratios and the extinction coefficients are constant (or normally distributed), and not related to biomass must be one of the explanations to why the big scale changes are not reproduced. The next planned step to examine these model parameters and see if they can be related to biomass.

5. CONCLUSIONS AND FURTHER WORK

The evaluation of the proposed model shows, that the intensity and polarimetry parts can predict their corresponding quantities with good results. The interferometric part is based on a model that has shown itself to be functional, but the parameter settings still need some trimming.

An interesting observation is that the ground-to-volume ratios (μ_{PQ}) apparently need to be very high ($\mu \gg 1$) for all polarizations. As expected, HH shows highest penetration depth, which also results in higher coherence levels and higher ground-to-volume ratios. While at higher frequencies HV is often assumed to only consist of volume scattering, in P-band it shows high coherence not only due to quite large amount of ground scattering but also due to more stable scatterers in the volume (such as thicker branches).

This model does not simulate incident angle influence nor the influence of extreme ground topography. These effects need to be studied in future. Also, intensity and polarimetric correlation for master and slave images are not differentiated in the presented version of the model.

REFERENCES

Cloude, S. & Papathanassiou, K. 1998, IEEE Transactions on Geoscience and Remote Sensing, 36, 1551

Cloude, S. & Papathanassiou, K. 2003, IEE Proceedings on Radar, Sonar & Navigation, 150, 125

Cloude, S. R. 2010, Polarisation Applications in Remote Sensing (Oxford University Press)

Garestier, F., Dubois-Fernandez, P. C., & Champion, I. 2008, IEEE Transactions on Geoscience and Remote Sensing, 46, 3544

Garestier, F. & Le Toan, T. 2010, IEEE Transactions on Geoscience and Remote Sensing, 48, 1528

Hajnsek, I., Keller, R. S. M., Horn, R., et al. 2009, BioSAR 2008 Technical Assistance for the Development of Airborne SAR and Geophysical Measurements during the BioSAR 2008 Experiment: Draft Final Report - BioSAR Campaign, Tech. rep., European Space Agency, ESA contract no. 22052/08/NL/CT

Hajnsek, I., Scheiber, R., Ulander, L., et al. 2008, BioSAR 2007 Technical Assistance for the Development of Airborne SAR and Geophysical Measurements during the BioSAR 2007 Experiment: Final Report without Synthesis, Tech. rep., European Space Agency, ESA contract no. 20755/07/NL/CB

Papathanassiou, K. & Cloude, S. 2001, IEEE Transactions on Geoscience and Remote Sensing, 39, 2352

Sandberg, G., Ulander, L. M. H., Fransson, J. E. S., Holmgren, J., & Le Toan, T. 2009, Remote Sensing of the Environment, accepted for publication

Soja, M. J., Sandberg, G., & Ulander, L. M. H. 2010, in Proceedings of the 2010 IEEE International Geoscience and Remote Sensing Symposium

Paper C

Forward Model

Authors:

M. J. Soja

Status:

Manuscript submitted to DLR as a part of the WP20 Report for the ESA project *Development of Algorithms for Forest Biomass Retrieval*, June 2011.

3 Forward Model

The Scene Generation Module (SGM) prepares synthesized polarimetric-interferometric SAR images for the End-to-End Simulator (E2ES). Within this module, there are two elements: the Scene Definition Module (SDM) and the Forward Model (FM). The SDM prepares scenes that are inserted into the FM, which predicts the elements of the extended covariance matrix. In this section, the FM will be described in detail, tested, and evaluated. The section starts with the definition of input parameters that will be provided to the FM by the SDM. The extended covariance matrix is then introduced and the basic quantities to be modelled are defined. After that, explicit functions for each modelled quantity are presented. In the last part, each function is evaluated in a series of tests and the prediction errors are quantified.

The FM presented here is suitable for stand-level extended covariance matrix prediction with a resolution of approximately 0.5 ha. An earlier version of the model can also be found in [R5].

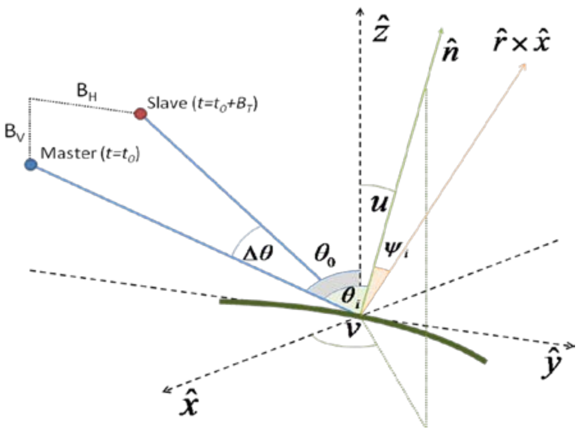

Figure 12 Definition of different angles. The green curve is the ground surface. Angle u is the surface slope, angle v is the slope aspect angle, θ_0 is the global incident angle, and θ_i is the local incident angle.

3.1 Input Parameters

Assume a scene size of $m \times n$ pixels. The FM requires the following parameters (in parentheses: mathematical symbols and sizes of the arrays):

- tree top height map, the mean height of the 100 tallest trees per hectare, H100 (h_{top} , $m \times n \times 1$)
- biomass map (W , $m \times n \times 1$)
- global incident angle map (θ_0 , $m \times n \times 1$)
- number of spatial baselines (n_{sp} , integer)
- vertical wavenumber maps, one for each baseline (k_z , $m \times n \times n_{sp}$)
- temporal baseline maps, one for each baseline (B_T , $m \times n \times n_{sp}$)
- temporal decorrelation scenario maps (1 for fast decorrelation, 2 for medium decorrelation, 3 for slow decorrelation), one for each baseline (D , $m \times n \times n_{sp}$)

- biome ID: 1 for boreal forest, 2 for tropical forest (BID , integer)

Note: only boreal forest has been implemented and is described in the current document.

Also, optionally, a digital elevation model (DEM) may be provided:

- digital elevation model, ground elevation map (h_0 , $m \times n \times 1$)

In the current version of the forward model, the DEM is not used, which means that the ground is assumed flat and there are no slopes. Consequently, the local incident angle and the global incident angle are equal (see Figure 12):

$$\theta_i \approx \theta_0 \tag{1}$$

3.2 The Output

The quantity to be modelled in the FM is the ***extended covariance matrix scaled to σ^0 on the diagonal***, here called $\left[\widehat{C}_6\right]$. However, in this derivation we start with the typical definition and scaling of the extended covariance matrix and $\left[\widehat{C}_6\right]$ will only be introduced in the end. The typically defined extended covariance matrix (scaled to $\left\langle |S|^2 \right\rangle$ on the diagonal) will be referred to as $\left[C_6\right]$.

Define two scattering vectors, one for the master image ($i=1$) and one for the slave image ($i=2$) as in [R8]:

$$\underline{\Omega}_i = \left[S_{i,HH} \quad \sqrt{2}S_{i,HV} \quad S_{i,VV}\right]^T \tag{2}$$

where $S_{i,PQ}$ is the complex scattering amplitude (Sinclair matrix element) for image i and polarization mode PQ, and ^{T} is the transpose operator. $\left[C_6\right]$ can be acquired by creating outer product combinations of these two:

$$[C_6] = \begin{bmatrix} \left\langle \underline{\Omega}_1 \underline{\Omega}_1^H \right\rangle & \left\langle \underline{\Omega}_1 \underline{\Omega}_2^H \right\rangle \\ \left\langle \underline{\Omega}_2 \underline{\Omega}_1^H \right\rangle & \left\langle \underline{\Omega}_2 \underline{\Omega}_2^H \right\rangle \end{bmatrix} = \begin{bmatrix} V_{11} & K_{12} \\ K_{12}^H & V_{22} \end{bmatrix} \tag{3}$$

where

$$[V_{ii}] = \begin{bmatrix} \left\langle |S_{i,HH}|^2 \right\rangle & \sqrt{2}\left\langle S_{i,HH} S_{i,HV}^* \right\rangle & \left\langle S_{i,HH} S_{i,VV}^* \right\rangle \\ \sqrt{2}\left\langle S_{i,HV} S_{i,HH}^* \right\rangle & 2\left\langle |S_{i,HV}|^2 \right\rangle & \sqrt{2}\left\langle S_{i,HV} S_{i,VV}^* \right\rangle \\ \left\langle S_{i,VV} S_{i,HH}^* \right\rangle & \sqrt{2}\left\langle S_{i,VV} S_{i,HV}^* \right\rangle & \left\langle |S_{i,VV}|^2 \right\rangle \end{bmatrix} \tag{4}$$

is the polarimetric covariance matrix for image i ,

$$[K_{12}] = \begin{bmatrix} \left\langle S_{1,HH} S_{2,HH}^* \right\rangle & \sqrt{2}\left\langle S_{1,HH} S_{2,HV}^* \right\rangle & \left\langle S_{1,HH} S_{2,VV}^* \right\rangle \\ \sqrt{2}\left\langle S_{1,HV} S_{2,HH}^* \right\rangle & 2\left\langle S_{1,HV} S_{2,HV}^* \right\rangle & \sqrt{2}\left\langle S_{i,HV} S_{i,VV}^* \right\rangle \\ \left\langle S_{1,VV} S_{2,HH}^* \right\rangle & \sqrt{2}\left\langle S_{1,VV} S_{2,HV}^* \right\rangle & \left\langle S_{1,VV} S_{2,VV}^* \right\rangle \end{bmatrix} \tag{5}$$

is the polarimetric interferometric covariance matrix, and ^{H} is the Hermitian operator (conjugate transpose).

3.3 Definition of the Modelled Quantities

In order to be able to model the covariance matrix, elements of matrices $[V_{ii}]$ and $[K_{12}]$ need to be re-written in terms of quantities which are easier to model. The following three basic quantities will be modelled:

- **Backscatter intensity sigma nought** (for image i, polarization mode PQ):

$$\sigma^0_{i,PQ} = Q_i \cdot \left\langle \left| S_{i,PQ} \right|^2 \right\rangle, \tag{6}$$

where

$$Q_i = \frac{4\pi \cos\psi_i}{A_{SRP}} \tag{7}$$

is a normalization factor with A_{SRP} being the area of a resolution cell in the slant range plane and ψ_i being the angle between the image plane normal and the tangential surface normal, as defined in Figure 12. Note that the subscript i in an angle definition means "incident" and not the image index. The following approximation is very common:

$$\psi_i \approx 90^\circ - \theta_i \tag{8}$$

where θ_i is the local incident angle (the angle between the negative slant range direction vector and the *z*-axis). This approximation is valid if the surface does not slope much in the azimuth direction.

By projecting $\sigma^0_{i,PQ}$ on a plane perpendicular to the wavevector, backscatter can be measured in gamma nought $\gamma^0_{i,PQ}$, which is in general more correlated with biomass and the topography influence is smaller:

$$\gamma^0_{i,PQ} = \frac{\sigma^0_{i,PQ}}{\cos\theta_i}. \tag{9}$$

- **Interferometric complex correlation** (for polarization mode PQ):

$$\tilde{\gamma}_{PQ} = \frac{\left\langle S_{1,PQ} S^*_{2,PQ} \right\rangle}{\sqrt{\left\langle \left| S_{1,PQ} \right|^2 \right\rangle \left\langle \left| S_{2,PQ} \right|^2 \right\rangle}}, \tag{10}$$

- **Polarimetric complex correlation** (image i):

$$\tilde{\rho}_i = \frac{\left\langle S_{i,HH} S^*_{i,VV} \right\rangle}{\sqrt{\left\langle \left| S_{i,HH} \right|^2 \right\rangle \left\langle \left| S_{i,VV} \right|^2 \right\rangle}}. \tag{11}$$

Note: the magnitude of complex correlation is sometimes referred to as coherence.

3.4 Simplified Extended Covariance Matrix

The interferometric (diagonal) elements of $\left[K_{12}\right]$ can be simply re-written in terms of $\sigma^0_{i,PQ}$ and $\tilde{\gamma}_{PQ}$ as follows:

$$\left\langle S_{1,PQ} S^*_{2,PQ} \right\rangle = \frac{\left\langle S_{1,PQ} S^*_{2,PQ} \right\rangle}{\sqrt{\left\langle \left|S_{1,PQ}\right|^2 \right\rangle \left\langle \left|S_{2,PQ}\right|^2 \right\rangle}} \cdot \sqrt{\left\langle \left|S_{1,PQ}\right|^2 \right\rangle \left\langle \left|S_{2,PQ}\right|^2 \right\rangle} = \\ = \tilde{\gamma}_{PQ} \cdot \frac{1}{\sqrt{Q_1 \cdot Q_2}} \cdot \sqrt{\sigma^0_{1,PQ} \cdot \sigma^0_{2,PQ}} \tag{12}$$

Likewise, the polarimetric elements of $\left[V_{ii}\right]$-matrices can be re-written as:

$$\left\langle S_{i,HH} S^*_{i,VV} \right\rangle = \frac{\left\langle S_{i,HH} S^*_{i,VV} \right\rangle}{\sqrt{\left\langle \left|S_{i,HH}\right|^2 \right\rangle \left\langle \left|S_{i,VV}\right|^2 \right\rangle}} \cdot \sqrt{\left\langle \left|S_{i,HH}\right|^2 \right\rangle \left\langle \left|S_{i,VV}\right|^2 \right\rangle} = \\ = \tilde{\rho}_i \cdot \frac{1}{Q_i} \cdot \sqrt{\sigma^0_{i,HH} \cdot \sigma^0_{i,VV}} \tag{13}$$

Theory shows [R15] that for the monostatic case the covariance of each co-polarized channel with the cross-polarized channel is:

$$\left\langle S_{i,HH} S^*_{j,HV} \right\rangle = \left\langle S_{i,VV} S^*_{j,HV} \right\rangle = 0.8 \tag{14}$$

Each non-zero non-diagonal element of $\left[K_{12}\right]$ can be re-written in terms of $\sigma^0_{i,PQ}$, ρ_i and $\tilde{\gamma}_{PQ}$ in two equivalent ways, under the assumption described in Eq. (14) in [R1], for example:

$$\left\langle S_{1,HH} S^*_{2,VV} \right\rangle \approx \\ \approx \frac{\left\langle S_{1,HH} S^*_{2,HH} \right\rangle}{\sqrt{\left\langle \left|S_{1,HH}\right|^2 \right\rangle \left\langle \left|S_{2,HH}\right|^2 \right\rangle}} \cdot \frac{\left\langle S_{2,HH} S^*_{2,VV} \right\rangle}{\sqrt{\left\langle \left|S_{2,HH}\right|^2 \right\rangle \left\langle \left|S_{2,VV}\right|^2 \right\rangle}} \cdot \sqrt{\left\langle \left|S_{1,HH}\right|^2 \right\rangle \left\langle \left|S_{2,VV}\right|^2 \right\rangle} = \\ = \tilde{\gamma}_{HH} \cdot \tilde{\rho}_2 \cdot \frac{1}{\sqrt{Q_1 \cdot Q_2}} \cdot \sqrt{\sigma^0_{1,HH} \cdot \sigma^0_{2,VV}} \tag{15}$$

and

$$\left\langle S_{1,HH} S^*_{2,VV} \right\rangle \approx \\ \approx \frac{\left\langle S_{1,HH} S^*_{1,VV} \right\rangle}{\sqrt{\left\langle \left|S_{1,HH}\right|^2 \right\rangle \left\langle \left|S_{1,VV}\right|^2 \right\rangle}} \cdot \frac{\left\langle S_{1,VV} S^*_{2,VV} \right\rangle}{\sqrt{\left\langle \left|S_{1,VV}\right|^2 \right\rangle \left\langle \left|S_{2,VV}\right|^2 \right\rangle}} \cdot \sqrt{\left\langle \left|S_{1,HH}\right|^2 \right\rangle \left\langle \left|S_{2,VV}\right|^2 \right\rangle} = \\ = \tilde{\rho}_1 \cdot \tilde{\gamma}_{VV} \cdot \frac{1}{\sqrt{Q_1 \cdot Q_2}} \cdot \sqrt{\sigma^0_{1,HH} \cdot \sigma^0_{2,VV}} \tag{16}$$

In order to enforce symmetry, the average of these two results is created as the final expression:

$$\left\langle S_{1,HH} S_{2,VV}^{*} \right\rangle \approx \frac{\tilde{\gamma}_{HH} \cdot \tilde{\rho}_2 + \tilde{\gamma}_{VV} \cdot \tilde{\rho}_1}{2\sqrt{Q_1 \cdot Q_2}} \cdot \sqrt{\sigma^0_{1,HH} \cdot \sigma^0_{2,VV}} \tag{17}$$

and similarly for:

$$\left\langle S_{1,VV} S_{2,HH}^{*} \right\rangle \approx \frac{\tilde{\gamma}_{HH} \cdot \tilde{\rho}_2^{*} + \tilde{\gamma}_{VV} \cdot \tilde{\rho}_1^{*}}{2\sqrt{Q_1 \cdot Q_2}} \cdot \sqrt{\sigma^0_{1,VV} \cdot \sigma^0_{2,HH}} \tag{18}$$

In the presented model topographic and atmospheric effects are omitted, and baselines can be assumed small. This gives:

$$\psi = \psi_1 \approx \psi_2 , \tag{19}$$

from which immediately follows that:

$$Q = Q_1 \approx Q_2 , \tag{20}$$

$$\sigma^0_{PQ} = \sigma^0_{1,PQ} \approx \sigma^0_{2,PQ} , \tag{21}$$

which means that no significant change in backscatter occurs between the two acquisitions, and also

$$\rho = \rho_1 \approx \rho_2 , \tag{23}$$

which means that no significant change in the mechanisms of scattering occurs between the acquisitions. This gives then:

$$V = V_{11} \approx V_{22} . \tag{24}$$

According to the requirements, the modelled matrix has to be scaled to σ^0 on the diagonal. This means that the normalization factor Q can be omitted. The final expression for the covariance matrix is then:

$$\left[\widehat{C}_6\right] \approx \begin{bmatrix} \widehat{V} & \widehat{K}_{12} \\ \widehat{K}_{12}^{H} & \widehat{V} \end{bmatrix} \tag{25}$$

where

$$\left[\widehat{V}\right] = \begin{bmatrix} \sigma^0_{HH} & 0 & \tilde{\rho} \cdot \sqrt{\sigma^0_{HH} \cdot \sigma^0_{VV}} \\ 0 & 2\sigma^0_{HV} & 0 \\ \tilde{\rho}^{*} \cdot \sqrt{\sigma^0_{HH} \cdot \sigma^0_{VV}} & 0 & \sigma^0_{VV} \end{bmatrix}, \tag{26}$$

$$\left[\widehat{K}_{12}\right] = \begin{bmatrix} \tilde{\gamma}_{HH} \cdot \sigma^0_{HH} & 0 & \tilde{\rho} \cdot \frac{\tilde{\gamma}_{HH} + \tilde{\gamma}_{VV}}{2} \cdot \sqrt{\sigma^0_{HH} \cdot \sigma^0_{VV}} \\ 0 & 2\tilde{\gamma}_{HV} \cdot \sigma^0_{HV} & 0 \\ \tilde{\rho}^{*} \cdot \frac{\tilde{\gamma}_{VV} + \tilde{\gamma}_{HH}}{2} \cdot \sqrt{\sigma^0_{VV} \cdot \sigma^0_{HH}} & 0 & \tilde{\gamma}_{VV} \cdot \sigma^0_{VV} \end{bmatrix}, \tag{27}$$

where the quantities to be modelled are: σ^0_{PQ}, $\tilde{\gamma}_{PQ}$, $\tilde{\rho}$. An "arc" above a matrix symbol means that the matrix has been scaled to σ^0 on the diagonal.

3.5 Model Derivation

This subsection deals with the derivation of three models: one for backscatter intensity, one for polarimetric correlation, and one for interferometric correlation. First, the experimental data used for the derivation of the models is described. Thereafter, each model is dealt with one by one. In the next subsection, the models are tested and evaluated and the errors are quantified.

3.5.1 Data Used

In this study, the following simplifications have been introduced:

- topographic surface roughness influence is not modelled,
- soil and canopy moisture influence is not modelled.

Due to the first simplification, data from the BioSAR 2008-campaign (conducted in the topographic area of Krycklan) have been excluded from the forward model. Moreover, from the three acquisition dates in the BioSAR 2007-campaign only one acquisition date – namely from May 2nd – has been chosen to be used for this FM. This was due to the fact that changes in scattering properties were observed between the three acquisition dates. These effects have most certainly been a consequence of change in moisture of the environment. Also, only the main heading (200-degree) was used to get full representation of the in-situ stands. Eventually, the following five slant range images were available: 0406, 0407, 0408, 0409, and 0411. This far, only two images (geocoded versions of 0406 and 0411) have been used for backscatter and polarimetric modelling. For thorough description of both BioSAR 2007 and BioSAR 2008 campaigns, please consult [R9] and [R10].

3.5.2 Backscatter Modelling

The backscatter coefficient gamma nought $\gamma^0_{i,PQ}$ can be plotted against stand-wise in-situ biomass in Remningstorp, see Figure 13. The correlation between $\gamma^0_{i,PQ}$ and biomass can be clearly seen for both the HH- and HV-channel [R12]. For VV there is very little correlation.

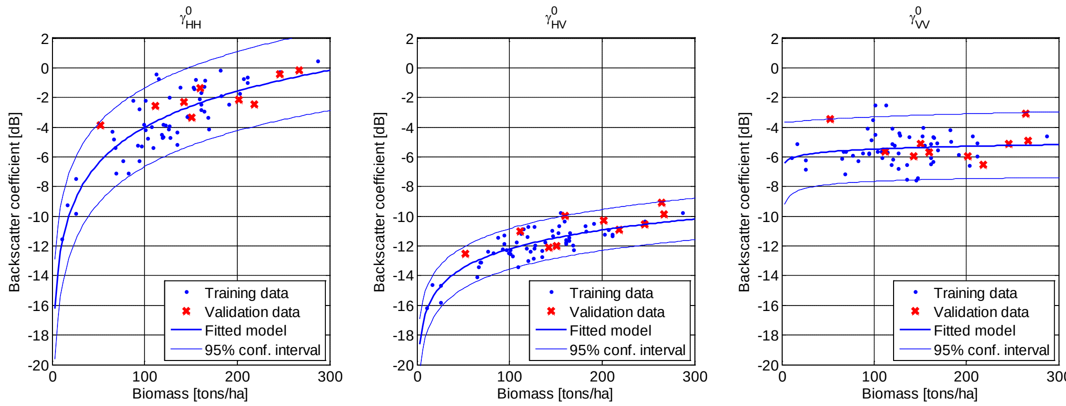

Figure 13 Backscatter gamma nought plotted versus biomass for the 58 training stands and 10 validation stands in Remningstorp. The blue line represents the model presented in (7) and fitted to the training data. Each point is a mean value from two acquisitions (0406 and 0411) and all pixels within a stand.

Table 6 Results from least-squares fitting of Eq. (27) to the data from 58 training stands in Remningstorp. The fitted parameters are shown with their corresponding 95% confidence intervals.

Polarization	a	$\Delta a_{95\%}$	b	$\Delta b_{95\%}$
HH	-20.10	±2.73	8.05	±1.32
HV	-20.65	±1.42	4.23	±0.68
VV	-6.72	±2.24	0.62	±1.08

Following these results, the following function is chosen to model the data:

$$\left[\gamma^0_{PQ}\right]_{dB} = a_{PQ} + b_{PQ} \cdot \log_{10} W \,, \tag{28}$$

where a_{PQ} and b_{PQ} are constants that need to be estimated by least-squares approach. Also, following Eq. (29), backscatter sigma nought can be modelled from biomass by an equivalent expression:

$$\left[\sigma^0_{PQ}\right]_{dB} = a_{PQ} + b_{PQ} \cdot \log_{10} W + 10 \cdot \log_{10}(\cos\theta_i)\,. \tag{29}$$

The parameters a_{PQ} and b_{PQ} have been fitted to the data from the 58 training stands using least-squares approach. In Table 6, the obtained values are shown together with their 95% confidence intervals.

3.5.3 Polarimetric Modelling

Following observations made in experimental data, the correlation between the HH- and VV-channel was chosen to be modelled by a regression function. The phase of $\tilde{\rho}$ was found to be directly proportional to the forest biomass, see Figure 14. Greater forest biomass introduced greater phase difference between the two co-polarized channels. However, the coherence was found virtually uncorrelated to biomass. These two relations can be summarized by the following model:

$$\tilde{\rho} = \overline{\rho} \cdot e^{i(\psi_0 + \eta W)} \tag{30}$$

where the parameter values can be found in 0 together with their 95% confidence intervals.

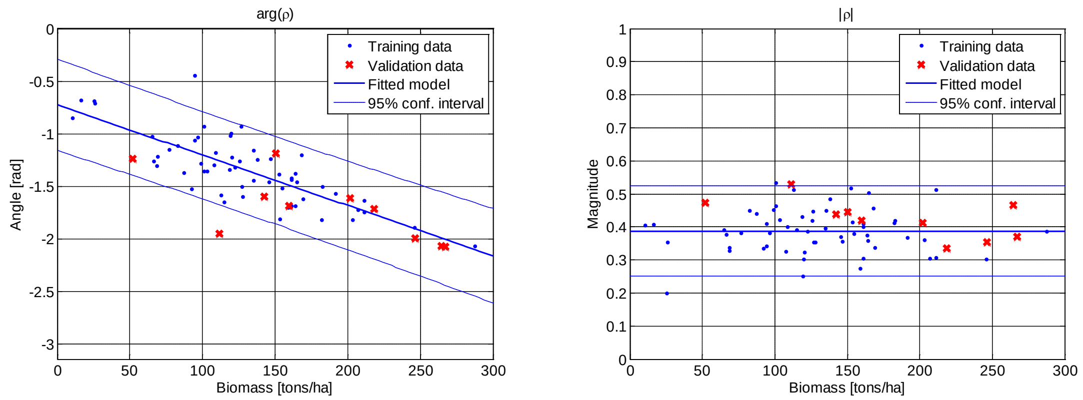

Figure 14 The phase of the polarimetric correlation is found proportional to biomass. The coherence between HH and VV is found to be quite constant between 0.3 and 0.5 for both training and validation stands. Each point is a mean value from two acquisitions (0406 and 0411) and all pixels within a stand.

Table 7 Results of least-squares fitting of Eq. (31) to the training data from Remningstorp. The estimated parameter values are shown together with their corresponding 95% confidence intervals.

$\overline{\rho}$	$\Delta\overline{\rho}_{95\%}$	ψ_0	$\Delta\psi_{95\%}$	η	$\Delta\eta_{95\%}$
0.39	±0.018	-0.72	±0.14	-0.0048	±0.0010

3.5.4 Interferometric Modelling

The interferometric contribution to the extended covariance matrix is modelled by the Random Volume over Ground model (RVoG, see [R2], [R3], [R4] and [R7]). Complicated scattering from forest is modelled as a combination of scattering from a random volume of particles, and an impenetrable ground surface.

Mathematically, the complex correlation of a volume of randomly oriented particles can be modelled as:

$$\tilde{\gamma}_{vol} = \frac{\int_0^{h_V} f(z) \cdot e^{ik_z z} dz}{\int_0^{h_V} e^{ik_z z} dz}, \tag{31}$$

where $f(z)$ is a profile function that describes the attenuation of the wave at different layers of the volume, k_z is the vertical wavenumber and h_V is the volume height. The profile function can take different forms. In the implemented forward model, two functions are included:

$$f_1(z) = \exp\left(\frac{2\sigma(z)\cdot z}{\cos\theta_i}\right), \tag{32}$$

which is an exponential profile function with a height dependent extinction coefficient [R13]:

$$\sigma(z) = \alpha + \beta z \tag{33}$$

where α is the extinction on top of the layer and β is the rate of change of extinction with height, and

$$f_2(z) = \exp\left(-\frac{(z-\delta)^2}{2\chi^2}\right), \tag{34}$$

which is a Gaussian function with mean scattering height δ and standard deviation χ . The Gaussian profile has been used in the past, e.g. in [R14].

The temporal decorrelation of volume will be modelled by a simple exponential function:

$$\gamma_{temp} = \exp\left(-\frac{B_T}{\tau_D}\right) \tag{35}$$

where τ_D is a temporal decorrelation constant for decorrelation scenario D. Adding an impenetrable ground surface described by the height h_0, the overall expression for the interferometric coherence becomes:

$$\tilde{\gamma}_{PQ} = \exp(ih_0 k_z)\cdot\frac{\tilde{\gamma}_{vol}\cdot\gamma_{temp} + \mu_{PQ}}{1+\mu_{PQ}}, \tag{36}$$

where μ_{PQ} is the ground-to-volume amplitude ratio. Polarization dependence is introduced by different ground-to-volume ratios for different channels.

The choice of the fixed parameters in RVoG (such as h_V, α, β, δ, χ, τ_D, and μ_{PQ}) is crucial for good interferometric predictions. However, many of these parameters are not directly related to the biophysical properties of the forest (or to the input variables). The choice of these parameters will now be presented and discussed.

Since many results show that the top canopy height h_{top} can be estimated from polarimetric SAR interferometry (POLInSAR) by direct inversion of the RVoG (see [R4], [R9], [R10], and [R11] for some examples), a good first approach is to set:

$$h_V \approx h_{top}, \tag{37}$$

where h_{top} is the mean height of the 100 tallest trees within a hectare (sometimes called H100).

Previous results [R11] show also that the extinction coefficient σ is poorly related to biomass of forest and more related to the vertical structure of canopy within the resolution cell. Also, the predicted correlation is fairly insensitive to the choice of σ as long as it stays within reasonable limits. Therefore it has been decided that a constant value of

$$\sigma = 0.1\,\text{dB/m}$$

is a good start since it has been estimated from P-band POLInSAR retrieval done by DLR [R11]. This implies $\alpha = 0.1\,\text{dB/m}$ and $\beta = 0$.

The temporal decorrelation constant τ_D can be chosen between one of the following three values:

$$\tau_1 = 50\ \text{days},$$

$$\tau_2 = 500\ \text{days},$$

$$\tau_3 = 5000\ \text{days},$$

which means that the temporal decorrelation is 0.37 after 2, 20, and 200 cycles, respectively (for a repeat cycle of 25 days). This corresponds to fast, medium, and slow temporal decorrelation. This was found to be a reasonable choice.

Since the use of constant ground-to-volume ratios has been shown insufficient for realistic modelling (see [R5]), the ground-to-volume ratios need to be made related to biophysical properties of the forest (as it most certainly is in reality). The ground-to-volume ratios are extracted from experimental data using the generalized Freeman-Durden decomposition theorem as described on pages 198-200 in [R7]:

$$\begin{aligned}[][T] &= [T_{ground}] + [T_{volume}] = \\ &= \begin{bmatrix} m_s\cos^2\alpha + m_d\sin^2\alpha & \cos\alpha\cdot\sin\alpha\cdot(m_d - m_s) & 0 \\ \cos\alpha\cdot\sin\alpha\cdot(m_d - m_s) & m_d\cos^2\alpha + m_s\sin^2\alpha & 0 \\ 0 & 0 & 0 \end{bmatrix} + m_v\begin{bmatrix} 1+\xi & 0 & 0 \\ 0 & 1 & 0 \\ 0 & 0 & 1 \end{bmatrix},\end{aligned} \tag{39}$$

where m_s, m_d, m_v are surface, double bounce, and volume scattering contributions, respectively, α is a parameter describing scattering orientation, and ξ is a parameter describing particle shape. If a certain value of ξ is assumed (here we will use 1/3, which corresponds to dipoles) and if one of the two ground-locked mechanisms is dominating, then the four parameters m_s, m_d, m_v and α can be computed rather easily from the measured values of the coherency matrix, see [R7]:

$$[T_{ii}] = \frac{1}{2}\begin{bmatrix} \left\langle \left|S_{i,HH+VV}\right|^2 \right\rangle & \left\langle S_{i,HH+VV}S^*_{i,HH-VV} \right\rangle & 2\left\langle S_{i,HH+VV}S^*_{i,HV} \right\rangle \\ \left\langle S_{i,HH-VV}S^*_{i,HH+VV} \right\rangle & \left\langle \left|S_{i,HH-VV}\right|^2 \right\rangle & 2\left\langle S_{i,HH-VV}S^*_{i,HV} \right\rangle \\ 2\left\langle S_{i,HV}S^*_{i,HH+VV} \right\rangle & 2\left\langle S_{i,HV}S^*_{i,HH-VV} \right\rangle & 4\left\langle \left|S_{i,HV}\right|^2 \right\rangle \end{bmatrix}. \tag{40}$$

However, the computation of m_s and m_d is ambiguous as there are two combinations of solutions. One way to deal with this is to separate the mechanisms into the stronger one ($m_{\max} = \max(m_d, m_s)$) and the weaker one ($m_{\min} = \min(m_d, m_s)$). The alpha parameter $\alpha_{\max}$ for the dominant scattering mechanism can be computed from $m_{\max}$ as described in [R7], page 199. From there, an expression for computation of ground and volume coherence for an arbitrary polarization **w** can be obtained:

$$\begin{aligned}[][T] &= [T_{ground}] + [T_{volume}] = \\ &= \begin{bmatrix} m_{\max}\cos^2\alpha_{\max} + m_{\min}\sin^2\alpha_{\max} & \cos\alpha_{\max}\cdot\sin\alpha_{\max}\cdot(m_{\min} - m_{\max}) & 0 \\ \cos\alpha_{\max}\cdot\sin\alpha_{\max}\cdot(m_{\min} - m_{\max}) & m_{\max}\cos^2\alpha_{\max} + m_{\min}\sin^2\alpha_{\max} & 0 \\ 0 & 0 & 0 \end{bmatrix} + m_v\begin{bmatrix} 1+\xi & 0 & 0 \\ 0 & 1 & 0 \\ 0 & 0 & 1 \end{bmatrix}.\end{aligned} \tag{41}$$

The ground-to-volume ratio for a certain known polarization **w** can now be computed from:

$$\mu(\mathbf{w}) = \frac{\mathbf{w}^H \langle | T_{ground} | \rangle \mathbf{w}}{\mathbf{w}^H \langle | T_{volume} | \rangle \mathbf{w}}. \tag{42}$$

For this study, four principal polarizations were examined:

- HH:

$$\mathbf{w} = \frac{1}{\sqrt{2}}\begin{bmatrix}1 & 1 & 0\end{bmatrix}^T \quad \rightarrow \quad \mu_{HH} = \frac{[m_{\max} + m_{\min} - \sin(2\alpha_{\max})]\cdot(m_{\max} - m_{\min})}{m_v(F_p + 1)}, \tag{43}$$

- VV:

$$\mathbf{w} = \frac{1}{\sqrt{2}}\begin{bmatrix}1 & -1 & 0\end{bmatrix}^T \quad \rightarrow \quad \mu_{VV} = \frac{[m_{\max} + m_{\min} + \sin(2\alpha_{\max})]\cdot(m_{\max} - m_{\min})}{m_v(F_p + 1)}, \tag{44}$$

- HH+VV:

$$\mathbf{w} = \begin{bmatrix}1 & 0 & 0\end{bmatrix}^T \quad \rightarrow \quad \mu_{HH+VV} = \frac{m_{\max}\cos^2\alpha_{\max} + m_{\min}\sin^2\alpha_{\max}}{m_v F_p}, \tag{45}$$

- HH-VV:

$$\mathbf{w} = \begin{bmatrix}0 & 1 & 0\end{bmatrix}^T \quad \rightarrow \quad \mu_{HH-VV} = \frac{m_{\max}\sin^2\alpha_{\max} + m_{\min}\cos^2\alpha_{\max}}{m_v}. \tag{46}$$

Moreover, approximate maximal and minimal values for ground-to-volume ratios can be extracted using eigenvalue decomposition as described on page 200 in [R7]:

- maximum:

$$\mu_{MAX} = \frac{m_{\max}}{m_v}\left(\sin^2\alpha_{\max} + \frac{1}{F_p}\cos^2\alpha_{\max}\right), \tag{47}$$

- minimum (orthogonal to minimum):

$$\mu_{MIN} = \frac{m_{\min}}{m_v(1 + (F_p - 1)\cdot\sin^2\alpha_{\max})}. \tag{48}$$

Stand averages of the six ground-to-volume ratios presented above were extracted from BioSAR 2007 data (acquisition 0411). The histograms for these values can be seen in Figure 15 (only forested areas are included).

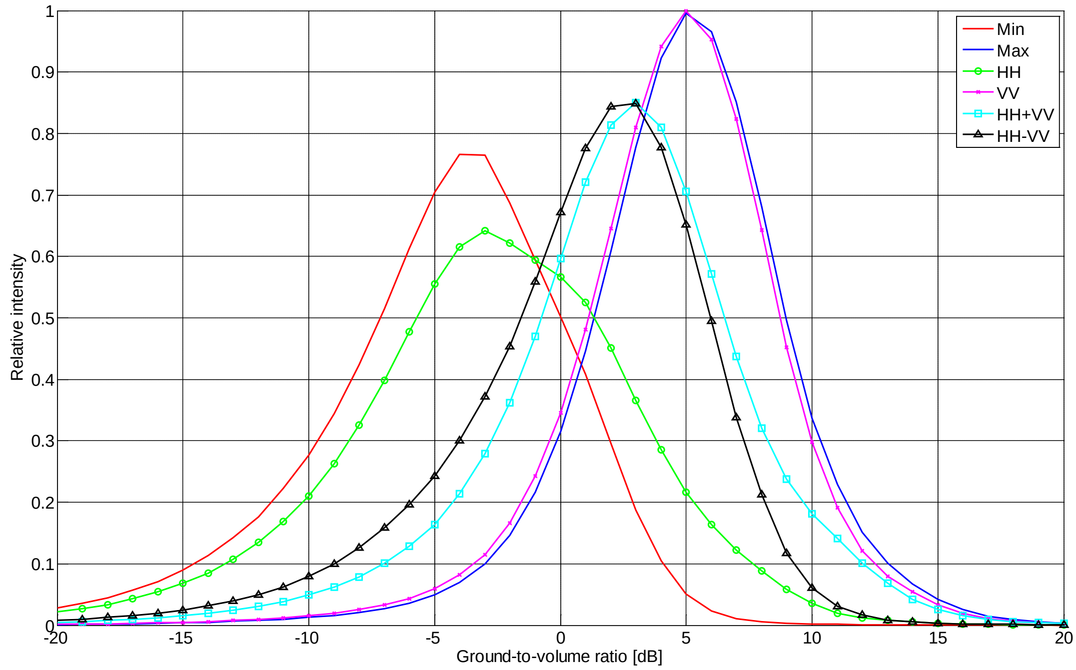

Figure 15 Distribution of ground-to-volume ratios for different polarization channels for forested areas in Remningstorp (biomass>0 tons/ha) and track 0411. Channels referred to as "max" and "min" correspond to the scattering mechanisms that give highest and lowest ground-to-volume ratios. These two mechanisms are assumed orthogonal. The values for the VV channel may be overestimated since VV channel is most prone to attenuation and this effect is not included in the Freeman-Durden model. Also, one can see that HH+VV and HH-VV channels give almost the same ground-to-volume ratios (which is a reasonable conclusion due to the fact that both consist of ground-locked scattering mechanisms).

A study of correlation between the ground-to-volume ratios and the three main input parameters (biomass, incident angle, height) showed rather low values, see Table 8 and it was concluded that no simple relationship between the three main input parameters and the ground-to-volume ratio could be found. Nevertheless, tests showed that even with low correlation values, the following model is still useful when it comes to reproducing different dependencies in the ground-to-volume ratio:

$$[\hat{\mu}]_{dB} = a_\mu + b_\mu \cdot \log_{10}(\cos\theta_i) + c_\mu \cdot \log_{10}(W) + d_\mu \cdot \log_{10}(h_{top}), \qquad (49)$$

where the constants a_μ, b_μ, c_μ, and d_μ has been estimated by fitting to data from the 58 training stands and are shown in Table 9. This model was chosen to predict HH-, HV- and VV-channel ground-to-volume ratios.

By empirical observations it was decided that the forward model performed best when the ground-to-volume ratios were estimated from the following data:

- HH-channel: μ_{MAX} (eq. (47)) was used in (49),
- HV-channel: μ_{MIN} (eq. (48)) was used in (49),
- VV-channel: $\mu_{MEAN} = \dfrac{\mu_{MAX} + \mu_{MIN}}{2}$ was used in (49).

Table 8 Comparison of the correlation between ground-to-volume ratios for six different polarization channels and three main input variables.

Training stands	μ_{MIN} [dB]	μ_{MAX} [dB]	μ_{HH} [dB]	μ_{VV} [dB]	μ_{HH+VV} [dB]	μ_{HH-VV} [dB]
$\cos(\vartheta_i)$	-0.17	0.34	-0.19	0.29	-0.17	0.54
Biomass	-0.27	-0.13	-0.29	-0.14	-0.22	-0.09
Lidar height	-0.31	0.17	-0.36	0.14	-0.18	0.28

Table 9 Estimated parameters for model (49) together with their corresponding 95% confidence intervals.

POL:	a_μ	$\Delta a_{95\%}$	b_μ	$\Delta b_{95\%}$	c_μ	$\Delta c_{95\%}$	d_μ	$\Delta d_{95\%}$
HV	2.39	±3.64	-5.73	±14.30	0.62	±1.65	1.68	±3.40
HH	-1.24	±3.51	-20.6	±13.80	1.51	±1.59	-5.32	±3.29
VV	0.55	±3.44	-7.78	±13.52	0.74	±1.56	0.78	±3.22

3.5.5 Error Modelling

A normally distributed error was added to all quantities modelled as described in the previous sections.

For **backscatter**, zero mean error ε_σ was added as follows:

$$\left[\sigma_{PQ}^{0,\mathrm{mod}}\right]_{dB} = a_{PQ} + b_{PQ} \cdot \log_{10} W + 10 \cdot \log_{10}(\cos\theta_i) + \varepsilon_\sigma \ . \tag{50}$$

The standard deviation of the error was set to the corresponding RMSE for the validation data found in Table 10.

For **polarimetric correlation**, zero mean phase error ε_ψ and zero mean magnitude ε_ρ error were added as follows:

$$\tilde{\rho}^{\mathrm{mod}} = (\bar{\rho} + \varepsilon_\rho) \cdot e^{i(\psi_0 + \eta W + \varepsilon_\psi)} \ . \tag{51}$$

The standard deviation of the error was set to the corresponding RMSE for the validation data found in Table 10.

For **ground-to-volume ratios**, zero mean error ε_μ was added as follows:

$$[\hat{\mu}^{\mathrm{mod}}]_{dB} = a_\mu + b_\mu \cdot \log_{10}(\cos\theta_i) + c_\mu \cdot \log_{10}(W) + d_\mu \cdot \log_{10}(h_{top}) + \varepsilon_\mu \ . \tag{52}$$

The standard deviation of the error was set to the corresponding RMSE for the validation data found in Table 10.

3.6 Model Evaluation

3.6.1 Evaluation Procedure Description

The fitted models were first evaluated against stand-wise data. Predictions of backscatter from biomass were done both for the training stands (58) and the validation stands (10). The first test evaluated the goodness of fit, while the second test evaluated the extrapolation possibilities of the model

A second test performed in order to evaluate the qualities of the forward model was to use the model to synthesize SAR images in order to do a side-by-side comparison with ESAR data. In order to do that, the following maps were used:

- Lidar-acquired biomass map (converted from stem volume map by multiplication with a factor 0.5 ton/m^3),
- Lidar-acquired DEM,
- Lidar-acquired forest height map,
- Vertical wavenumber map (provided by DLR together with the SAR images, geo-coded using provided look-up table, corrected for ground topography using a slope map derived from abovementioned DEM)
- Local incident angle map (computed from the global incident angle map provided by DLR and from a slope map derived from abovementioned DEM).

The first three maps needed to be resampled to radar geometry. This was done using the look-up tables provided with the ESAR data. Whenever synthetic radar images were created, the quantities modelled as different functions of biomass, height, and incident angle were normally distributed with standard error corresponding to the value found during evaluation on validation stands (presented later on in this section). When models were evaluated stand-by-stand, the parameters were constant according to the values found during least-squares fitting. Temporal decorrelation was not modelled. A minor problem occurred during resampling of lidar DEM to slant range geometry. This resulted in a "marbling pattern" consisting of some distributed NaN (Not a Number) values that can be seen in the DEM in Figure 16. This problem was also inherited later on whenever DEM was used.

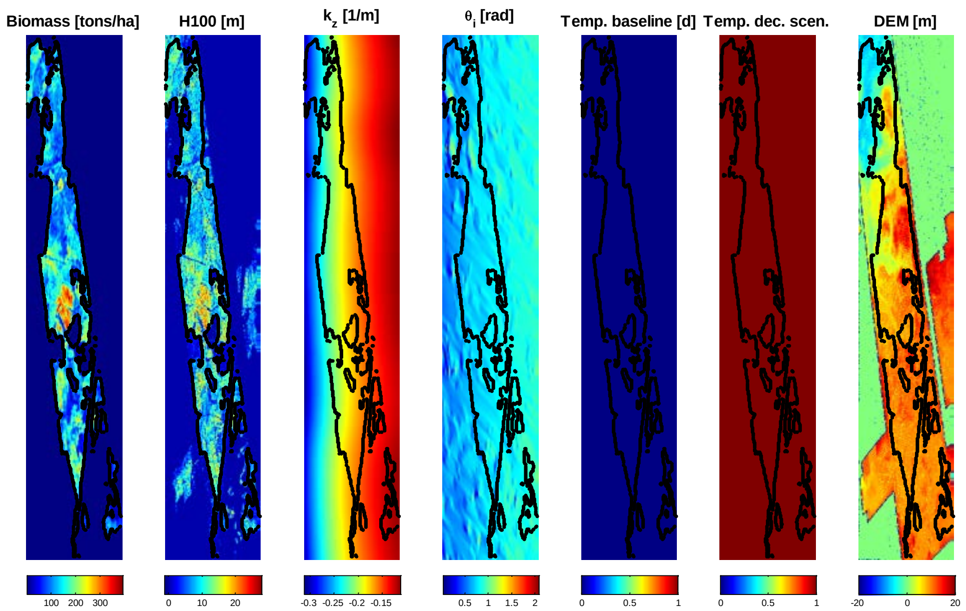

Figure 16 Input parameter setup for Remningstorp test. Biome was chosen to be 1 and the number of spatial baselines was chosen to 1. The spatial baseline corresponding to the shown vertical wavenumber image is approximately 60 meters and corresponds to the POLInSAR pair 0408 (slave) and 0411 (master). Black contours delineate the smallest region where all data are available. Forest height and DEM were acquired using airborne lidar scanning. Biomass map was derived from stem volume map, which was derived from airborne lidar scanning data, field plots, and optical species classification. Incident angle map shows the local incident angle after slope correction. The marbling pattern in the DEM image originates from an unsolved error that occurs during resampling to radar geometry and this error is unfortunately reproduced in all products that use DEM.

3.6.2 Backscatter Prediction Evaluation

The first test was carried out on the stand-wise biomass data. First, sigma nought was predicted for the 58 training stands to verify the fitting. In Figure 17 the results are plotted against the mean backscatter intensity for each training stand. A root-mean-square error of approximately 0.67 dB can be measured for the HV-channel. For HH-channel, the corresponding error is 1.29 dB and for VV-channel it is 1.06 dB. Even though the error for VV is lower than for HH, there is very little correlation with the real backscatter (the coefficient of determination is only 0.08). VV backscatter cannot be predicted from biomass with good results. Low RMSE value comes from the fact that the dynamics of VV are low. Sigma nought error was also evaluated for the ten validation stands, see Figure 18. The RMSE is approximately 0.81 dB for HV and 1.36 for HH, which gives a good idea of what can be expected from the model. For the exact RMSE values, consult Table 8.

In Figure 19, three synthesized images are shown. The estimation of backscatter is good for both HH and HV, but there is a slight underestimation of backscatter especially in sparser forest and the HH-channel. Also, the experimental data show slightly greater dynamics due to the fact that there are other mechanisms controlling backscatter and these mechanisms are unaccounted for in the model. The RMSE for the HV-channel is 1.64 dB and that is the lowest value for the three polarizations. In the HH image, one can see that the modelled image is a little noisier than the original one. This might be caused by the fact, that the fitting parameters were randomized from pixel to pixel using global statistics. The use of local statistics (which take local conditions such as forest density and biomass into consideration) may be used to improve the model in the future. The estimation of model parameters may be more stable in regions with especially high/low biomass.

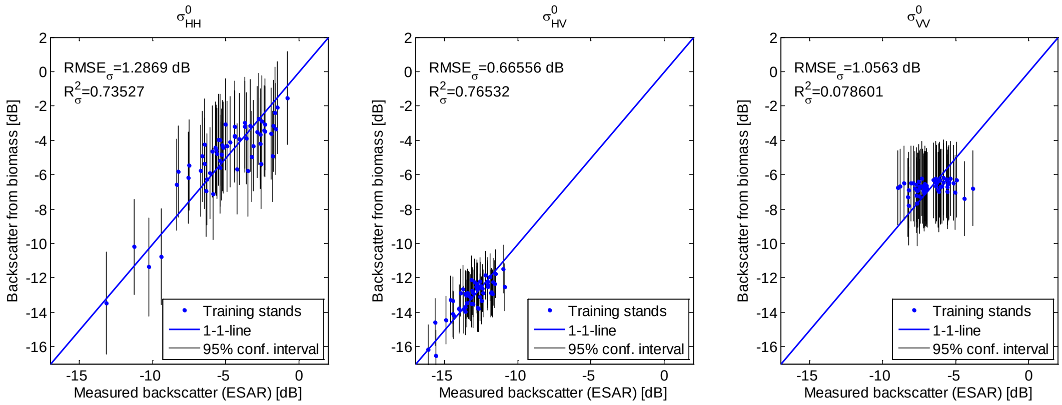

Figure 17 Modelling results for backscatter sigma nought (computed from biomass and the local incident angle θ_i) using the 58 training stands. Vertical lines represent the 95% confidence interval for each prediction.

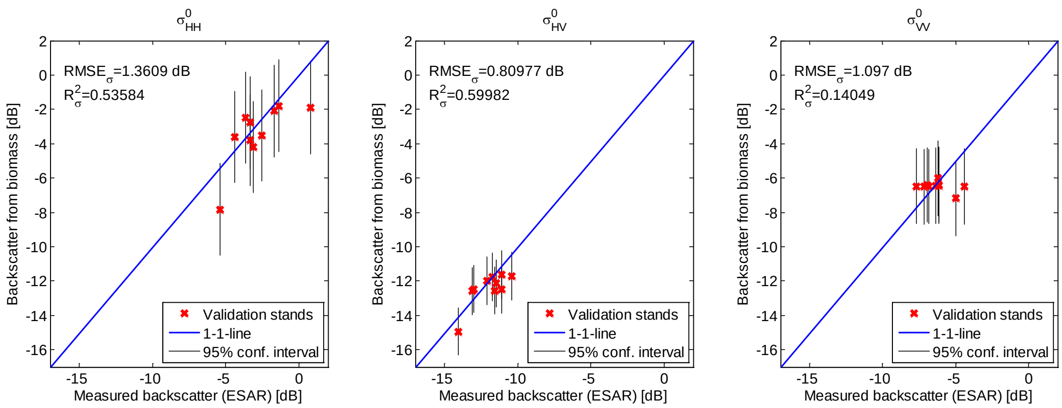

Figure 18 Modelling results for backscatter sigma nought using the 10 validation stands. The results are especially good for the HV channel where the RMSE is around 0.82 dB. HH and VV are estimated with errors a little above 1 dB. Vertical lines represent the 95% confidence interval for each prediction.

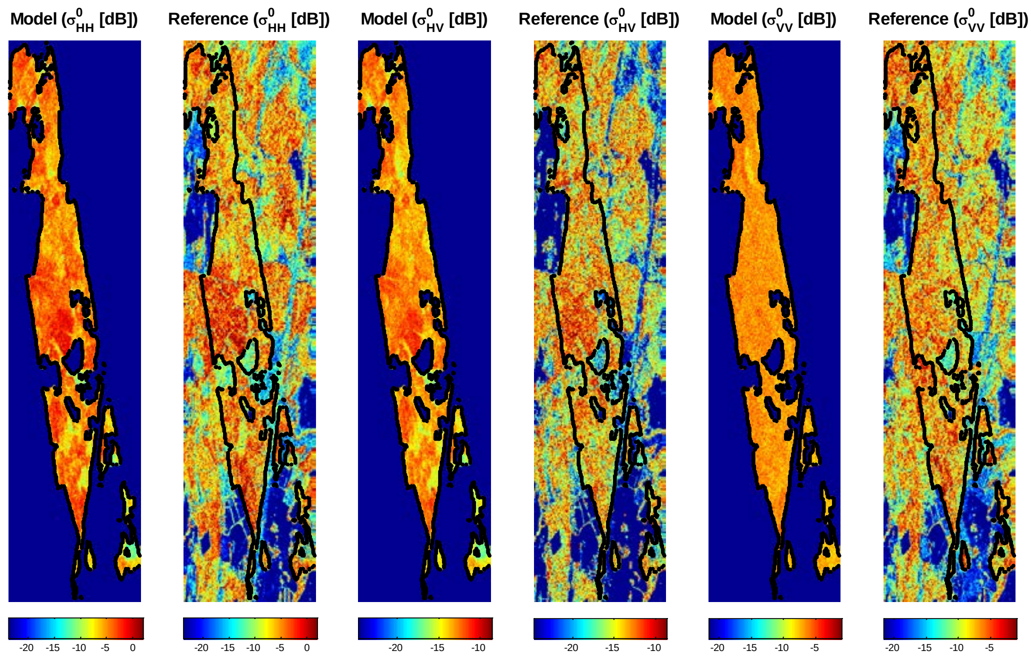

Figure 19 Modelled SAR images for Remningstorp. The black contour delineates the region of known biomass. Outside that region biomass was assumed to be zero. The results for HH and HV channels are generally good. Since almost no correlation with biomass was found for the VV channel, the synthesized VV backscatter image consists only of random variations.

3.6.3 Polarimetric Prediction Evaluation

The evaluation of the polarimetric part of the FM has been performed in the exact same way as for the intensity part. Here, the phase and the magnitude of the polarimetric correlation were evaluated separately. Since the phase was found correlated with biomass, the prediction on a stand-wise level gives very good results. Phase prediction error of a little more than 0.27 radians (15.5 degrees) is a low value. Coherence was found to be rather constant, somewhere between 0.3 and 0.5 with root-mean-square error of 0.07.

Map-based prediction gives equally good results: RMSE of 0.08 for magnitude and 20 degrees of root-mean-square error for phase. Also, looking at the scatter plot in Figure 22 one can see that phase is well-predicted. The effect of non-local statistics of the fitted parameters (as observed in Figure 17) is less prominent here.

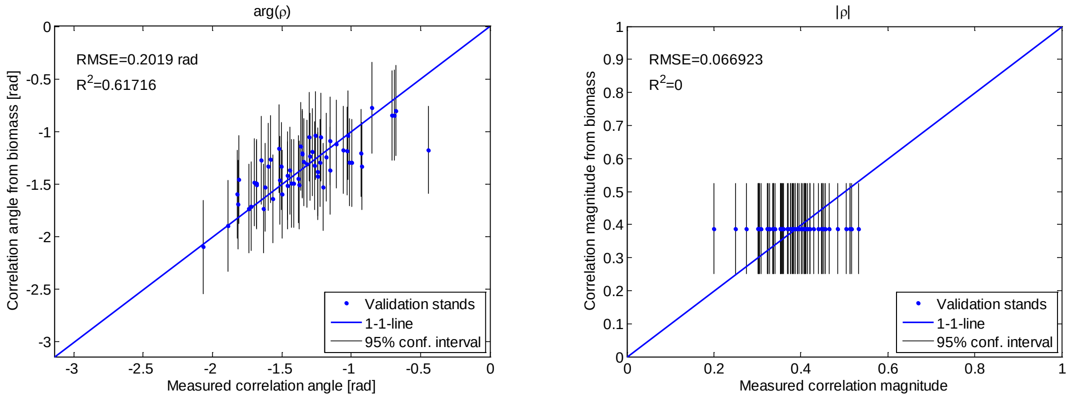

Figure 20 Verification of the fitted model. Since the phase angle of the HH-VV correlation is well correlated with the stand-wise biomass, the prediction results are very good with approximately 0.2-radian (11.5-degree) RMSE. The coefficient of determination gives a value of 0.62. The magnitude of HH-VV correlation was found impossible to be predicted from biomass only and this can be also seen in the graph to the right. Vertical lines represent the 95% confidence interval for each prediction.

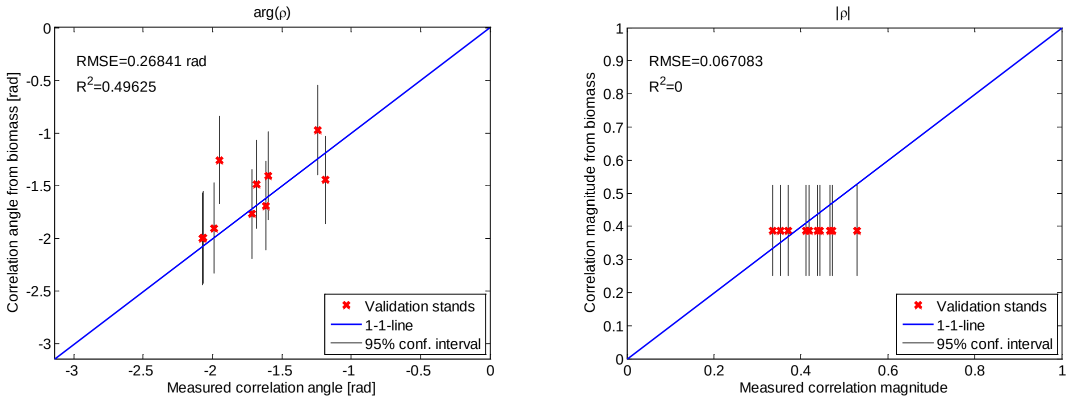

Figure 21 The evaluation of the model done on the validation stands shows good prediction of correlation phase (error of approximately 0.27 radians or 15.5 degrees). Magnitude cannot, once again, be well predicted from biomass. Vertical lines represent the 95% confidence interval for each prediction.

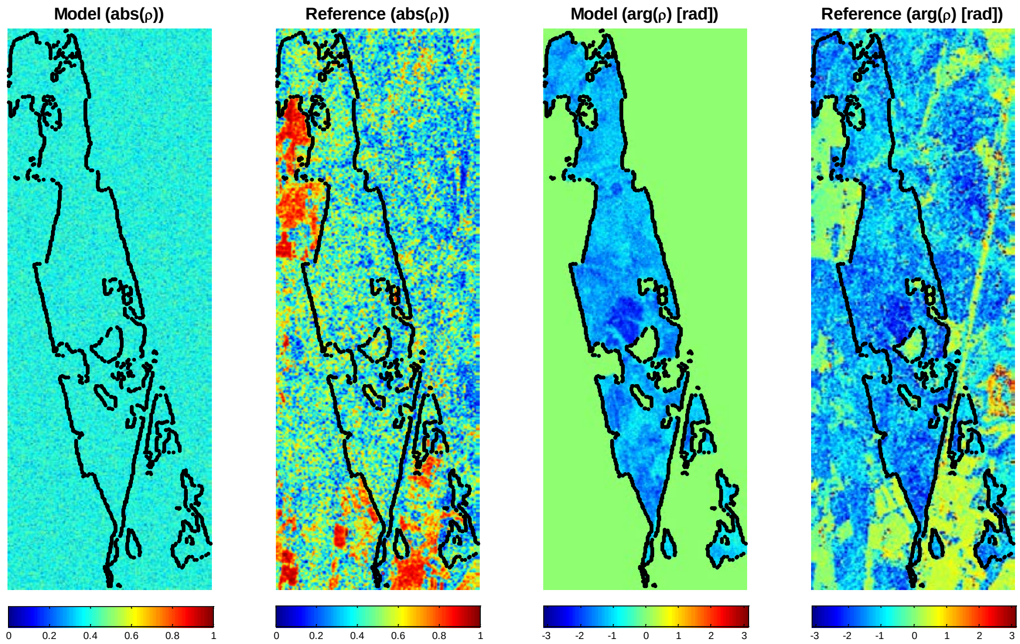

Figure 22 Modelled polarimetric (HH-VV) correlation (phase and coherence) for Remningstorp. The black contour delineates the region of known biomass. Outside that region biomass was assumed to be zero and the model gives reasonable results (compare with non-forested areas in the ESAR images). There is a very good correlation between both phase images. However, since almost no correlation with biomass was found for the HH-VV coherence, the modelled image shows no spatial variation except the pixel-to-pixel randomness.

3.6.4 Interferometric Prediction Evaluation

First, the prediction of ground-to-volume ratios is evaluated, see Figure 23 and Figure 24. Since the ground-to-volume ratios were found to be weakly correlated with the input variables, predicted values suffer from the lack of dynamics observed in the measured values. Nevertheless, prediction on image-level shows rather good results, see Figure 25, Figure 26, and Figure 27. For an estimation of model errors on stand and image level, consult Table 10 and Table 11.

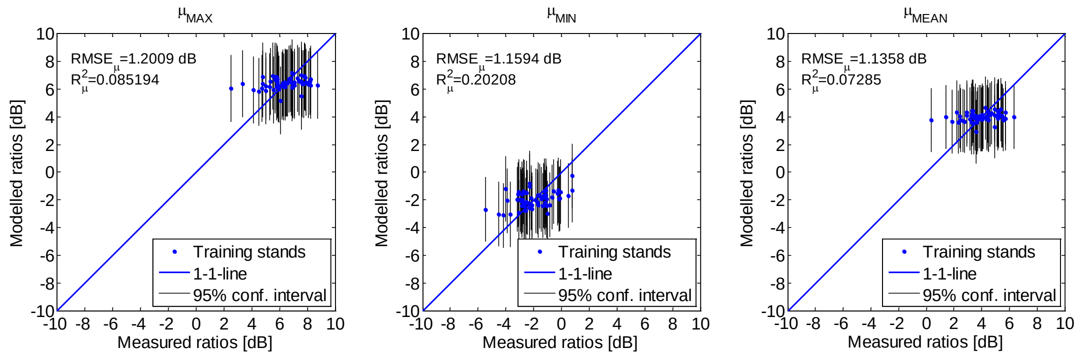

Figure 23 Modelled ground-to-volume ratios for 58 training stands in Remningstorp. The two channels HH and HV were chosen to be modelled by functions fitted to the maximal and minimal observed ground-to-volume ratios. Ground-to-volume ratio for VV channel was chosen to be modelled as the mean of these for HH and HV. This choice was based on the empirical observations in the real data.

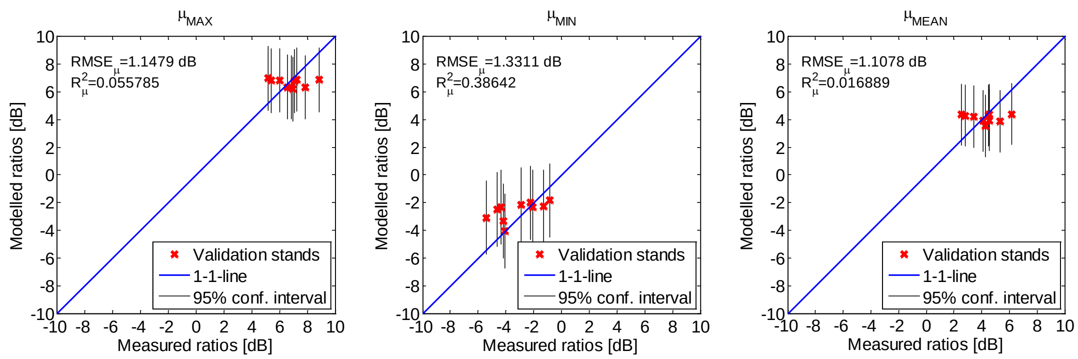

Figure 24 Modelled ground-to-volume ratios for 10 validation stands in Remningstorp. The two channels HH and HV were chosen to be modelled by functions fitted to the maximal and minimal observed ground-to-volume ratios. Ground-to-volume ratio for VV channel was chosen to be modelled as the mean of these for HH and HV. This choice was based on the empirical observations in the real data.

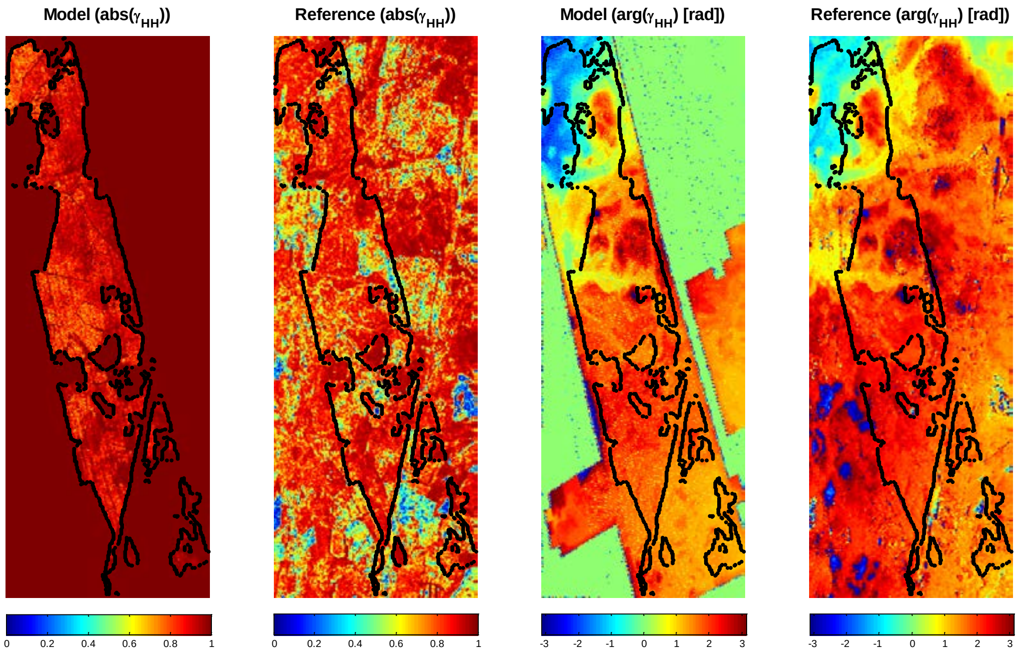

Figure 25 Modelled interferometric HH correlation (phase and coherence) for Remningstorp. The black contour delineates the smallest region where all input parameters are known. Outside this region, some input parameters are set to zero. Compare with Figure 16 for reference. The model overestimates coherence in some regions of high biomass. The phase is predicted very well. The marbling pattern seen in the second image from the right is an error introduced in the DEM during resampling to radar geometry and does not originate from the model.

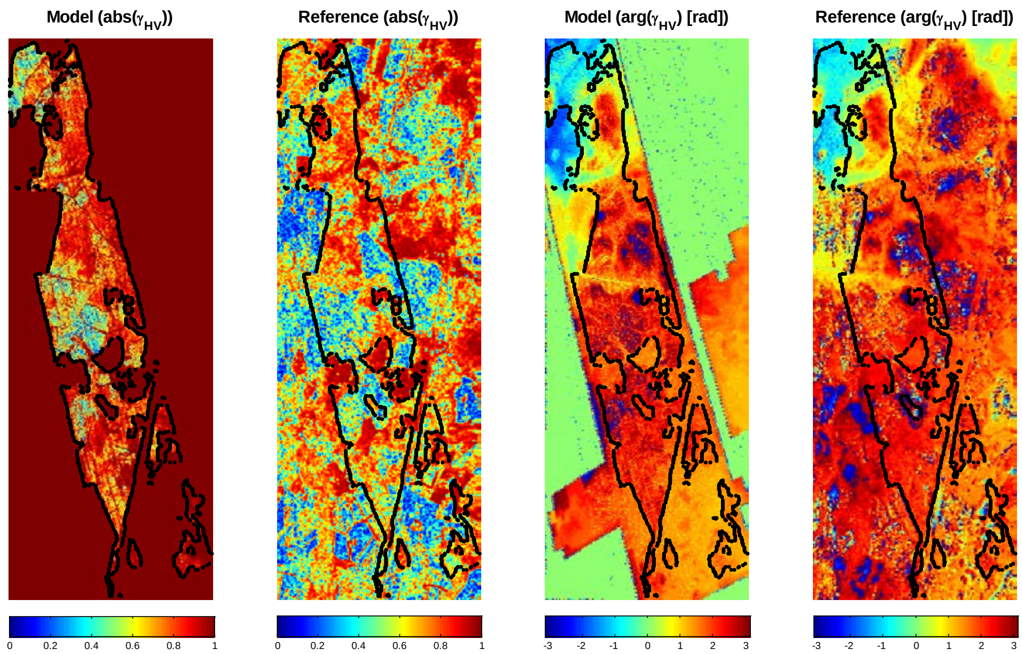

Figure 26 Modelled interferometric HV correlation (phase and coherence) for Remningstorp. The black contour delineates the smallest region where all input parameters are known. Outside this region, some input parameters are set to zero. Compare with Figure 16 for reference. The spatial structures are reproduced well except in some regions where the trees are high. The phase is predicted very well. The marbling pattern seen in the second image from the right is an error introduced in the DEM during resampling to radar geometry and does not originate from the model.

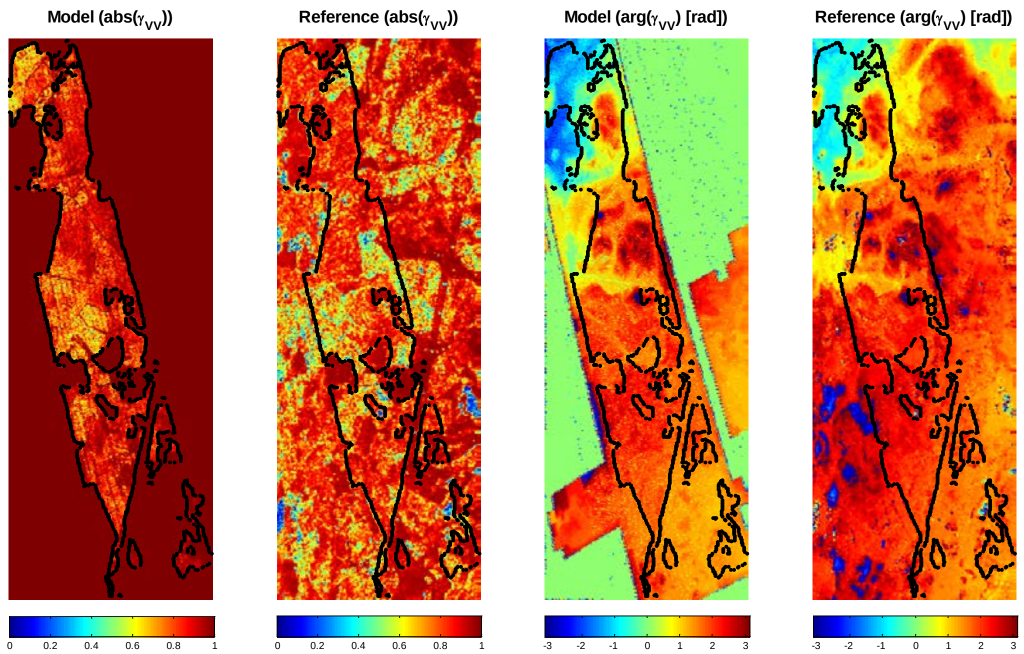

Figure 27 Modelled interferometric VV correlation (phase and coherence) for Remningstorp. The black contour delineates the smallest region where all input parameters are known. Outside this region, some input parameters are set to zero. Compare with Figure 16 for reference. The spatial structures are reproduced well except in some regions where the trees are high. The phase is predicted very well. The marbling pattern seen in the second image from the right is an error introduced in the DEM during resampling to radar geometry and does not originate from the model.

Table 10 Errors in estimation of the quantities computed with empirical formulas. "Residuals" refers to evaluation on the same data set as training (see Figure 18). "Validation" refers to evaluation on a separate data set (see Figure 18).

Predicted quantity:	RMSE (residuals):	R^2 (residuals):	RMSE (validation):	R^2 (validation):
$\left[\sigma^0_{HH}\right]_{dB}$	1.29 dB	0.74	1.36 dB	0.54
$\left[\sigma^0_{HV}\right]_{dB}$	0.67 dB	0.77	0.81 dB	0.60
$\left[\sigma^0_{VV}\right]_{dB}$	1.06 dB	0.079	1.10 dB	0.14
$\lvert\tilde{\rho}\rvert$	0.067	0	0.067	0
$\arg(\tilde{\rho})$	0.20 rad	0.62	0.27 rad	0.50
μ_{MAX} (used for HH)	1.20 dB	0.085	1.33 dB	0.39
μ_{MIN} (used for HV)	1.16 dB	0.20	1.33 dB	0.39

μ_{MEAN} (used for VV)	1.14 dB	0.072	1.11 dB	0.017

Table 11 Forward model prediction errors. Comparison between synthesized and reference images. Only areas with biomass>0 tons/ha counted.

Predicted quantity:	RMSE (magnitude):	RMSE (phase):
$\left[\sigma_{HH}^{0}\right]_{dB}$	2.24 dB	
$\left[\sigma_{HV}^{0}\right]_{dB}$	1.64 dB	
$\left[\sigma_{VV}^{0}\right]_{dB}$	2.02 dB	
ρ	0.083	0.35
γ_{HH}	0.099	0.38
γ_{HV}	0.16	0.72
γ_{VV}	0.097	0.40

References

[R1] Papathanassiou, K. and Cloude, S. R. (2005). “Single vs. Multi-Polarization Interferometry”, Available at: http://earth.eo.esa.int/polsarpro/Manuals/2_Single_vs_Multi_Polarization_Interferometry.pdf

[R2] Cloude, S. and Papathanassiou, K. (1998). "Polarimetric SAR Interferometry." IEEE Transactions on Geoscience and Remote Sensing 36(5): 1551-1565.

[R3] Papathanassiou, K. And Cloude, S. (2001). "Single-Baseline Polarimetric SAR Interferometry." IEEE Transactions on Geoscience and Remote Sensing 39: 2352-2363.

[R4] Cloude, S. and Papathanassiou, K. (2003). "Three-stage Inversion Process for Polarimetric SAR Interferometry." IEE Proceedings on Radar, Sonar & Navigation 150(3): 125-134.

[R5] Soja, M. J. and Ulander, L. M. H. (2011), “A Hybrid Model for Interferometric and Polarimetric P-band SAR Modelling of Forests”, Conference Paper for PolInSAR 2011

[R6] Ulander, L. M. H. (1996). "Radiometric Slope Correction of Synthetic Aperture Radar Images." IEEE Transactions on Geoscience and Remote Sensing 34(5): 1115-1122.

[R7] Cloude, S. R. (2010). Polarisation Applications in Remote Sensing, Oxford University Press.

[R8] Lee, J.-S. and Pottier, E. (2009), “Polarimetric Radar Imaging”, CRC Press

[R9] Hajnsek, I., Scheiber, R., et al. (2008). BioSAR 2007 Technical Assistance for the Development of Airborne SAR and Geophysical Measurements during the BioSAR 2007 Experiment: Final Report without Synthesis.

[R10] Hajnsek, I., R. S. M. Keller, et al. (2009). BioSAR 2008 Technical Assistance for the Development of Airborne SAR and Geophysical Measurements during the BioSAR 2008 Experiment: Draft Final Report - BioSAR Campaign.

[R11] Papathanassiou, K., et al. (2010), Slides from 1st Progress Meeting and slide set: Polarimetric SAR Interferometry for Quantitative Parameter Estimation

[R12] Sandberg, G., Ulander, L. M. H., et al. (2009). "L-band versus P-band SAR for Biomass Retrieval in Hemiboreal Forest." Remote Sensing of the Environment.

[R13] Garestier, F. and Le Toan, T., (2010). "Forest Modeling for Height Inversion Using Single-Baseline InSAR/Pol-InSAR Data." IEEE Transactions on Geoscience and Remote Sensing 48(3): 1528-1539.

[R14] Hagberg, J. O., Ulander, L. M. H., Askne, J., (1995). ”Repeat-Pass SAR Interferometry Over Forested Terrain”, IEEE Transactions on Geoscience and Remote Sensing 33(2): 331-340.

[R15] Nghiem, S. V., Yueh, S. H., Kwok, R., and Li, F. K. (1992). ”Symmetry Properties in Polarimetric Remote Sensing”, Radio Science 27(5): 693-711

Paper D

Update on Forward Model

Authors:

M. J. Soja

Status:

Manuscript submitted to DLR as annex to Paper C, September 2011.

1 Update on Forward Model

In this annex, an update on the forward model is presented. Apart from the previously described boreal scenario from the BioSAR 2007-campaign, a tropical scenario is included based on data from TropiSAR 2009-campaign. The tropical data come from the test site of Paracou in French Guyana and the boreal data come from the test site of Remningstorp in southern Sweden. Only one acquisition was chosen from both data sets: 0104 from TropiSAR 2009 and 0411 from BioSAR 2007 since it was decided that temporal changes should not be modelled. Also, a truncated Gaussian profile function will be introduced here.

The validity of the presented forward model is as follows:

1) Boreal scenario: biomass ranges 0-300 tons/ha. However, below 10 tons/ha, the output is set to values that are reasonable but not fully based on experimental data.

2) Tropical scenario: biomass ranges 300-500 tons/ha.

Outside the ranges of validity, the model returns NaN.

1.1 Backscatter Intensity Modelling

The model presented in Eq. (28) in Section 3.5.2 of this report was fitted to both boreal and tropical data. The resulting curves are plotted in Figure 1. The fitted model parameters are shown in Table 1 together with the p-value for the F-statistics ($p<0.05$ means that the model describes the behaviour well). The error levels and the coefficients of determination are shown in 0. One can observe higher correlation between VV and biomass for the tropical forest as compared with boreal forest. The mean backscatter levels differ by up to approximately 10 dB between BioSAR and TropiSAR data. The variability of the data is also lower for the tropical scenario than for the boreal scenario.

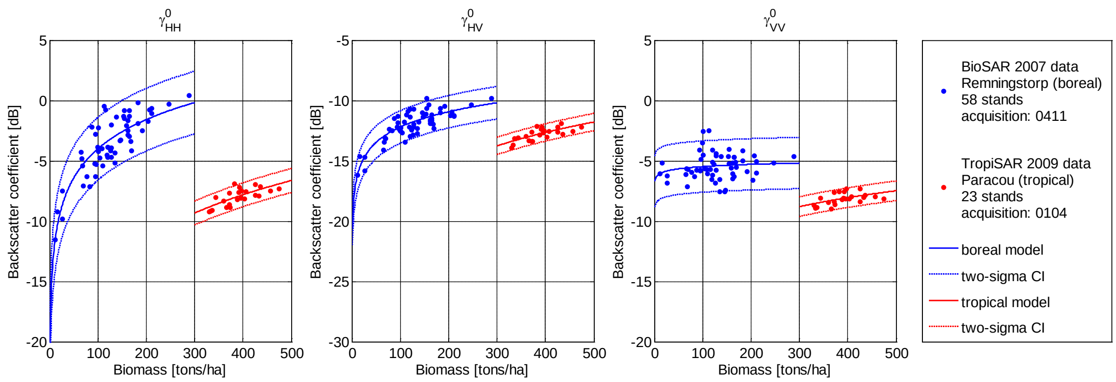

Figure 1 Backscatter gamma nought plotted versus biomass for 58 stands in Remningstorp (boreal forest) and 23 stands in Paracou (tropical forest). The fitted curves are plotted with solid lines, and the corresponding two-sigma (approximately 95%) confidence intervals (CI) with dashed lines.

Table 1 Results from least-squares fitting of Eq. (26) in Section 3.5.2 to the data from 58 stands in Remningstorp and 23 stands in Paracou. The fitted parameters are shown with their corresponding 95% confidence intervals. The VV-model for the boreal forest is not a good model as the uncertainty in the estimation of parameter *b* is very high.

Pol:	a (boreal) [dB]	b (boreal)	p-value	a (tropical) [dB]	b (tropical)	p-value

HH	-20.1±2.73	8.05±1.32	0	-39.44±13.67	12.15±5.28	0
HV	-20.65±1.42	4.23±0.68	0	-35.89±9.89	8.93±3.82	0
VV	-6.72±2.24	0.62±1.08	0.255	-23.48±11.23	5.93±4.34	0.01

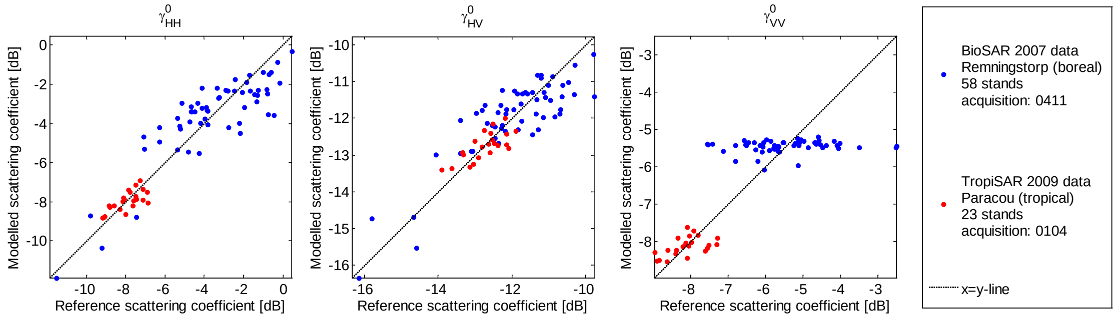

Figure 2 Prediction results for boreal and tropical models. VV cannot be predicted from biomass in a satisfactory way.

Table 2 Prediction errors for the boreal and tropical models (see also Figure 2). Boreal forest in light green and tropical forest in dark green.

Pol:	RMSE [dB]	R-squared	RMSE [dB]	R-squared
HH	1.29	0.73	0.48	0.52
HV	0.67	0.73	0.35	0.53
VV	1.06	0.02	0.4	0.28

1.2 Polarimetric Correlation Modelling

The model (30) presented in Section 3.5.2 was fitted to tropical and boreal data and the results are plotted in Figure 3. The estimated parameter values are shown in Table 3 together with the p-value for the F-statistics for the non-constant modelFigure 1. The magnitude of the HH-VV correlation (coherence) was found almost uncorrelated with biomass and therefore is to be modelled by a constant.

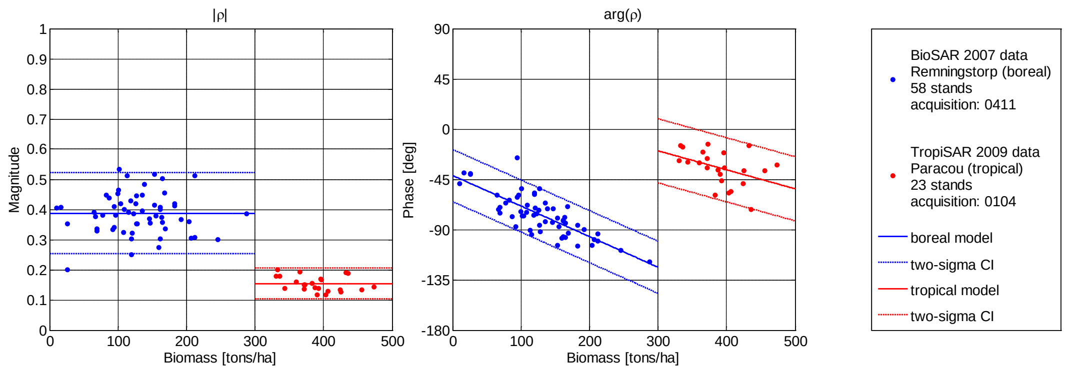

Figure 3 Magnitude and phase of the HH-VV correlation is here plotted versus biomass for 58 stands in Remningstorp (boreal forest) and 23 stands in Paracou (tropical forest). The modelling lines are shown in solid and the corresponding two-sigma (approximately 95%) confidence intervals (CI) in dashed. Due to

low correlation between the HH-VV coherence and biomass, the mean value was chosen to be modelled as a constant.

Table 3 Results from least-squares fitting of elements from Eq. (30) in Section 3.5.3 to the data from 58 stands in Remningstorp and 23 stands in Paracou. The fitted parameters are shown with their corresponding 95% confidence intervals.

Pol:	$\bar{\rho}$	ψ_0 [deg]	η	p-value (phase)
Boreal	0.39±0.02	-41.47±8.07	-0.27±0.06	0
Tropical	0.15±0.01	31.61±66.35	-0.17±0.17	0.05

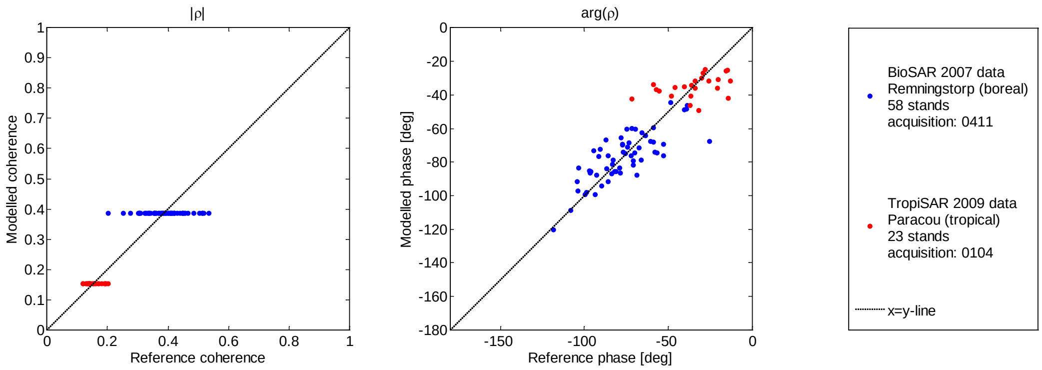

Figure 4 Prediction results for boreal and tropical models. Coherence is predicted as a constant value due to its poor correlation with biomass and other input parameters.

Table 4 Statistics of model predictions. Boreal forest in light green and tropical forest in dark green.

Pol:	RMSE	R-squared	RMSE	R-squared
Magnitude	0.07	-	0.02	-
Phase [deg]	11.57	0.62	14.04	0.17

1.3 Interferometric Modelling

1.3.1 Ground-to-volume Ratio Modelling

The ground-to-volume ratios were extracted according to the procedures described in Section 3.5.4. However, it was found that the correlation of ground-to-volume ratios with all input variables was too low for satisfactory modelling. The ground-to-volume ratios were thus chosen to be modelled as constants, so that parameters *b*, *c*, and *d* were set to zero in Eq. (49). In Figure 5, the stand-wise ground-to-volume ratios for the maximal and minimal contribution are plotted for boreal and tropical forests. The ground-to-volume ratios for HH, HV, and VV correlation were modelled as described in the end of Section 3.5.4. In Table 5, the estimated values for the ground-to-volume ratios are shown. In Table 6, the root-mean-square prediction error for the maximal and minimal ground-to-volume values are shown for both boreal and tropical forest.

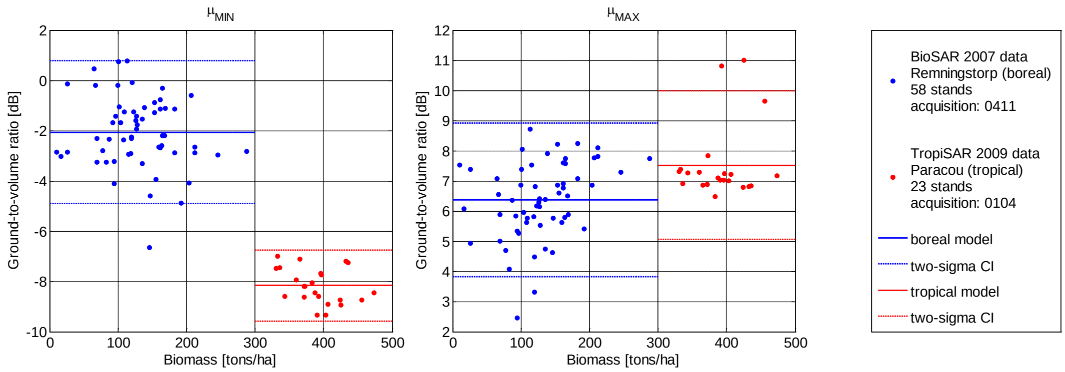

Figure 5 Maximal and minimal ground-to-volume ratios (GTV) extracted from tropical and boreal data. GTV for HH is modelled as the mean value of the maximal GTV. GTV for HV is modelled as the mean value of the minimal GTV. GTV for VV is modelled as the mean of the GTV for HH and HV.

Table 5 Values for ground-to-volume ratios used in the forward model for tropical and boreal scenario.

Pol:	HH (from MAX) [dB]	HV (from MIN) [dB]	VV (from MEAN in dB) [dB]
Boreal	6.37±0.34	-2.06±0.37	2.16±0.25
Tropical	7.52±0.53	-8.16±0.31	-0.32±0.31

Table 6 Statistics of model predictions. Boreal forest in light green and tropical forest in dark green.

Pol:	RMSE	RMSE
MAX [dB]	1.27	1.2
MIN [dB]	1.41	0.69

1.3.2 Profile Function

Two profile functions are available to be inserted in Eq. (31), Section 3.5.4:

- Exponential profile function: $f_1(z) = \exp\left(\dfrac{2\sigma(z)\cdot z}{\cos\theta_i}\right)$ with $\sigma(z) = \alpha + \beta z$

- Truncated Gaussian function: $f_2(z) = \exp\left(-\dfrac{(z-\delta)^2}{2\chi^2}\right)$

The chosen values of the parameters δ, χ, α, and β are shown in Table 7. For the exponential profile, the values were chosen based on reports for BioSAR 2007 and TropiSAR 2009 (as described in Section 3.5.4). For the truncated Gaussian function, the parameter setup is a guesstimate.

Table 7 Profile function setup parameters. Boreal forest in light green and tropical forest in dark green. h_V is the volume height.

	α [dB/m]	β [dB/m^2]	δ [m]	χ [m]
Boreal	0.1±0.2	0	$(0.5\pm0.1)\cdot h_V$	$(0.25\pm0.05)\cdot h_V$
Tropical	0.3±0.2	0	$(0.75\pm0.15)\cdot h_V$	$(0.25\pm0.05)\cdot h_V$

Paper E

Spaceborne SAR for Detection of Boreal Wind-Thrown Forest and Clear-Cuts

Authors:

L. E. B. Eriksson, J. E. S. Fransson, **M. J. Soja**, and M. Santoro

Status:

Submitted to *Remote Sensing of Environment*, August 2011

*Manuscript

Spaceborne SAR for detection of boreal wind-thrown forest and clear-cuts

L.E.B. Eriksson[a], J.E.S. Fransson[b], M.J. Soja[a], M. Santoro[c]

[a] Chalmers University of Technology, Department of Earth and Space Sciences, Gothenburg, Sweden

[b] Swedish University of Agricultural Sciences, Department of Forest Resource Management, Umeå, Sweden

[c] Gamma Remote Sensing AG, Gümligen, Switzerland

Abstract

A controlled experiment simulating wind-thrown forest was carried out at a hemi-boreal test site in Sweden. The simulation was done by manual felling of trees in September 2009. The trees were left on the ground until November 2009 to ensure image acquisitions after the simulated storm. SAR data from the satellites TerraSAR-X, RADARSAT-2 and ALOS were acquired before, during and after this period. The backscatter signatures were analyzed to evaluate possibilities to detect wind-thrown forest and clear-cuts. TerraSAR-X HH-polarized backscatter showed a significant increase when the trees were felled and the difference to selected reference forest stands was 1.2 dB to 2.0 dB. The corresponding differences for RADARSAT-2 were 0.2 dB to 1.2 dB for HH-polarization and 0.1 to 1.1 dB for HV-polarization. When the trees were felled, the ALOS backscatter decreased to 1.6 dB below the reference forest for HH-polarization and 0.4 dB to 0.8 dB for HV-polarization. Shadowing effects in fine resolution TerraSAR-X and RADARSAT-2 data showed a high potential for detection of wind-throw with separation to the reference forest backscatter of

between 4.9 dB and 9.2 dB. For clear-cut detection ALOS proved to give the most suitable data.

Keywords: SAR, Forestry, Wind-thrown forest, Storm damage, Clear-cut, X-band, C-band, L-band

1. Introduction

Each year storms and hurricanes cause destruction in many areas around the world. In Europe, an annual average of 35 million m^3 wood was damaged by natural disturbances during the period 1950 to 2000, and storms were responsible for 53% of the total damage (Schelhaas et al., 2003). In 2005 and 2007 devastating storms hit Scandinavia causing large damage to forested areas. In Sweden it was estimated that about 70 million cubic meters of timber were blown down in 2005 (Anon., 2006) and about 12 million cubic meters in 2007, to a value of billions of Euro. At such occasions, rapid mapping of wind-thrown forests is crucial in order to salvage timber values and prevent insect outbursts that could kill the remaining standing trees. After a severe storm, it is also of high importance to get a fast overview to assess the roads that should be cleared from wind-thrown trees as well as to detect power lines that are broken. Due to the large geographical extent of forests, rapid monitoring and mapping of forests can in practice only be done efficiently by means of airborne and spaceborne remote sensing methods. Synthetic aperture radar (SAR) has the potential of being a useful tool due to its independence of weather and sun illumination that allow rapid and frequent acquisitions, but few results have been published about detection of wind-thrown forest..

Fully polarimetric airborne SAR campaigns following acute storm damages have been performed with the Japanese Pi-SAR platform to study forest damages on the Hokkaido Island after the Songda typhoon in September 2004 (Wang et al., 2010) and the Canadian CONVAIR platform to study ice storm damages in the Ottawa region in January 1998 (Touzi et al., 1999). The first study compared polarimetric L-band data collected before and after the typhoon and observed changes in double-, volume- and surface scattering of respectively 27.5 dB, -0.20 dB and -20.3 dB. The classification accuracy of the generated damage map was 77.7 %. The second study indicated that a polarimetric parameter could detect differences between pre and post storm data that could not be seen in the normal linear or circular polarizations. Storm damage detection has also been studied using the Swedish airborne VHF-band platform CARABAS-II (Fransson et al., 2001; Fransson et al., 2002; Ulander et al., 2005; Ulander et al., 2006, Fransson et al., 2007). Operating at very low frequencies (20-90 MHz) and HH-polarization, CARABAS-II gave a response from horizontal trees that was significantly higher than from vertical trees, provided the horizontal trees were not lying directly on the ground and their axes were parallel to the flight track within about ±30° (±22° for single trees). In addition to the capability to detect areas where all trees have been wind-thrown, CARABAS-II also showed a potential to detect storm-felled trees in stands with standing forest and near borders with high trees. A method for automatic detection of wind-thrown forest in VHF SAR images is described by Folkesson et al. (2006). The method use autocorrelation functions to identify elongated structures created by fallen trees. However, due to the relatively low coverage, high expenses and long deployment time for airborne platforms, spaceborne systems are preferable for mapping and monitoring of large areas.

After the hurricane Mitch hit Central America in November 1998, SAR data from the European ERS-1 and ERS-2 satellites were used together with optical SPOT images to assess the damage. The study showed that damaged forest could be detected when SAR images acquired before and after the hurricane were compared (Nezry et al., 2000). After the severe storm Lothar that hit France, Switzerland and southern Germany on the 26th of December 1999, a comparison of classification performance for selected airborne and spaceborne optical and SAR sensors was performed for an Alpine forest area (Steinmeier et al., 2002). This study showed that during the winter season, the optical images gave severe classification problems due to snow, long shadows and the fact that the spectral properties of forest without foliage resembled those of the wind-thrown forest. With SAR, the investigators were not able to detect the wind-thrown forest using only backscatter intensity. On the contrary, the interferometric coherence helped in detecting areas affected by storm damage. After Lothar, successful storm damage detection using SAR interferometry with the ERS-1 and ERS-2 satellites was also presented by Dwyer et al. (2000), Yesou et al. (2000) and Wiesmann et al. (2000). Unfortunately, the ERS-1/2 constellation is no longer operational.

After the storm in Sweden in 2005, research activities for detection of wind-thrown forest with satellite images were initiated following the activation of the International Charter Space and Major Disaster, an instrument for rapid provision of images at catastrophic events. . The usefulness of optical data was limited by the prevailing winter conditions (low sun-angle, extensive cloud cover and variable snow cover). The analysis of SAR data showed that with a limited number of backscatter intensity images from C-band SAR onboard the Envisat and Radarsat-1 satellites it was not possible to detect wind-thrown forests, except in the highest resolution Radarsat-1 images where in some cases changes in texture could be observed, primarily related to changes in shadowing from standing/fallen trees (Ulander et al., 2005).

The lack of sensitivity of C-band backscatter measurements to standing and wind-thrown trees at decametric spatial resolution can be explained as the felling of trees does not significantly change the total backscatter, since the needles and small branches are still present as a randomly oriented scattering volume. At coarse resolution, the speckle noise is also more extended compared with higher resolution SAR images, limiting the possibilities to detect wind-thrown forests. On the other hand, longer wavelengths are sensitive to larger structures like stems and large branches that change the general orientation when a tree is felled, which could improve the possibilities for detection of wind-thrown forest. Improved spatial resolution of satellite SAR images is also expected to improve the possibilities to identify forest damaged by a storm. Thus, to further explore the use of radar remote sensing to detect wind-thrown forest it is of interest to analyze images from satellite SAR systems with longer wavelength or finer spatial resolution than the SAR data from Envisat and Radarsat-1.

A preliminary investigation on the feasibility of mapping wind-thrown forest using data from the Advanced Land Observing Satellite (ALOS) Phased Array type L-band Synthetic Aperture Radar (PALSAR) was carried out as a controlled experiment, where trees were manual felled to simulated wind-thrown forest (Fransson et al., 2007). The experiment took place in 2006 at the test site

Remningstorp located in the south of Sweden. When comparing the reference forest stand with the wind-thrown stands, the backscatter intensity decreased about 1.6 dB for ALOS PALSAR acquired in Fine Beam Single polarization (FBS) images with look angle 34.3° and HH polarization.

This paper presents results from a second experiment that was conducted in Sweden in 2009. The aim was to evaluate the possibility to detect forest change caused by storm felling (primary goal) and clear cutting (secondary goal) using multitemporal SAR data from three satellites, TerraSAR-X (X-band), RADARSAT-2 (C-band) and ALOS (L-band). Preliminary results based on visual interpretation of a limited number of co-polarized images acquired by these satellites are available in Fransson et al. (2010). In this paper a larger data set, including both co- and cross-polarized images, are analyzed and the first quantitative results are presented. The investigation is done by comparing the backscatter intensity of images acquired before and after a simulation of wind-thrown forest.

The test site and the available data will be presented in Section 2 and the experiment and the methods in Section 3. In Section 4 results are presented for each of the three satellites and a summary and discussion is given in Section 5.

2. Test site and data description

2.1 Test site

The Remningstorp test site is located in the southern part of Sweden (Lat. 58°30’ N, Long. 13°40’ E) and covers about 1,200 ha of productive forest land (Fig. 1). The test site is characterized by hemi-boreal coniferous forests and the dominant tree species are Scots pine (*Pinus sylvestris*) and Norway spruce (*Picea abies*). The dominant soil type is till (i.e. a mixture of glacial debris) with a field layer consisting of different herbs, blueberry (*Vaccinium myrtillus*), and narrowleaved grass (e.g. *Deschampsia flexuosa*). In denser old spruce stands the field layer is absent. The ground elevation is moderately varying between 120 and 145 m above sea level.

2.2 Satellite data

The SAR dataset consisted of TerraSAR-X images acquired in spotlight mode with 1.2 m and 1.1 m spatial resolution (slant range and azimuth) and RADARSAT-2 images acquired in ultra-fine beam mode with 1.6 – 2.4 m spatial resolution in range and 3 m in azimuth The images were acquired in single polarization mode (HH-polarization for TerraSAR-X images, HH- or HV-polarization for RADARSAT-2 images). Both satellites were programmed to acquire data at different look angles and in both ascending and descending passes to study differences in the shadowing effects. For the satellite data that have been used in this study, acquisition dates and observation configurations are listed in Table 1 for TerraSAR-X and in Table 2 for RADARSAT-2.

ALOS PALSAR data were acquired according to JAXA's global observation strategy for ALOS (Rosenqvist et al., 2007), which for Sweden means summer and autumn acquisitions in Fine Beam Dual polarization (FBD) mode at 34.3° look angle in ascending pass. Compared to the ALOS PALSAR images in Fine Beam Single polarization (FBS) mode that were used in the study after the first storm simulation experiment in 2006 (Fransson et al., 2007), FBD mode provide images with HV polarization in addition to the HH images, but at the expense of a reduced spatial resolution of about 20 m. Acquisition dates and observation configurations for the used ALOS PALSAR images are listed in Table 3.

All SAR images were obtained in radar geometry, i.e. in range-azimuth coordinates and to reduce speckle noise multi-look processing was applied. The multi-look factors were determined based on the initial pixel size of the data and the desired output spatial resolution. Data were obtained in a form that only required application of a calibration constant to obtain calibrated sigma zero images. The calibration constants are given by the processing facilities. To allow inter-comparison between datasets, the images were geocoded to the Swedish coordinate system RT90. For image geocoding, a Digital Elevation Model (DEM) acquired from the Swedish National Land Survey (Lantmäteriet) with 50 m posting was used. The DEM was oversampled to allow geocoding of the SAR images to the selected pixel sizes of 5 m for TerraSAR-X and RADARSAT-2 and 25 m for ALOS PALSAR. A lookup table that described the relationship between the radar and the map geometry was used (Wegmüller, 1999). The transformation described in the lookup table is set up based on orbital data. In case of inaccuracies of the orbital data, refinement of the lookup table is necessary. This is implemented in form of cross-correlation algorithm between the SAR image and a reference image for the output geometry. Matching features in the two images are used to detect possible offsets, which are directly related to errors in the geocoding transformation.

2.3 *In situ* observations

Meteorological observations, including temperature, precipitation and snow depth were obtained from a weather station located within the Remningstorp test area and managed by the Swedish Meteorological and Hydrological Institute (SMHI). For each day the maximum, minimum and average temperatures were available. Relevant observations for satellite acquisition dates are included in Table 1, Table 2 and Table 3. The temperatures in the tables are the daily averages, but in cases when the recorded minimum temperature was below 0º C at some point during the day, a note is given in the table. As precipitation might affect the moisture for the following days, information about rainfall has been included not only for the acquisition date but also for the day before the acquisition. In case of rainfall during several consecutive days, the total amount of precipitation during five days (including the acquisition date) has been indicated.

3. Methods

3.1 Experiment description

A controlled experiment simulating wind-thrown forest was carried out at the Remningstorp test site in the beginning of September 2009. The simulation was done by manual felling of trees and instead of stripping and removing the trees (as is done in clear-felling), the trees were left for a few orbit repeat cycles to ensure image acquisitions after the simulated storm. In total, four coniferous stands with a size of about 1.2 ha were used to simulate wind-thrown forest (Fig. 2, Fig. 3 and Fig. 4). The trees were felled in two directions to simulate two possible main wind directions during a storm. For two of the stands (T1 and T4 in Fig. 4) the trees were felled in 80° and for the others (T2 and T3 in Fig. 4) in 35° with the heading measured clockwise from north (0°). The felled trees were then harvested and removed from the forest in November 2009. In total, more than 2500 cubic metre of timber were felled. The stem volumes recorded by the harvester were about 650, 590, 330, 520 m3/ha for T1, T2, T3 and T4, respectively. The test areas were situated in forest stand with tree height of about 25 m.

3.2 Analysis of satellite data

In order to study changes of the forest backscatter after a severe storm, satellite datasets were divided in three phases:

- Phase 1: Before felling = mature forest
- Phase 2: Trees lying on the ground = simulated wind-thrown forest
- Phase 3: After trees were removed = clear-cut

In addition to the test areas T1 to T4 where the trees were felled, four reference areas were selected, two with mature forest, R1 and R2 (Fig. 4) and two in clear-cuts, R3 and R4 (Fig.

4). The stem volumes for the reference areas R1 and R2 were estimated using laser scanning data in combination with *in situ* data to about 240 and 300 m3/ha with an average tree height of 18 and 21 m, respectively. R3 and R4 are two of the four forest areas that were felled during the previous storm experiment in 2006. The reference areas were included to avoid misinterpretation due to backscatter changes caused by rainfall or other environmental conditions not related to the storm experiment.

In the image analysis, each of the four test areas was divided in three smaller regions, one that was affected by shadowing during ascending passes, one that was affected by shadowing during descending passes and one that was outside the shadowed region for both ascending and descending passes. For T1, T2 and T3, these regions are shown in Fig. 5. The polygons that were selected for each region were used for all satellite images and the average backscatter values for each region and each reference area were measured. The backscatter values in the shadowed regions were significantly lower than for the surrounding areas, but in most cases a region that is brighter than the surrounding area can also be observed in each test area. This increase in backscatter is caused by layover from trees at the side of the test area opposite to the shadowed region. For ascending passes these areas roughly correspond to the regions that were defined as shadow for descending passes and in the same way the shadow regions for ascending passes can be used to estimate the backscatter for the layover areas for descending passes. To avoid biases specific for one test area, the backscatter values that are reported in this paper are averages of the values for each region type from all four test areas, and for both areas in the case of reference forest and reference clear-cut.

4. Results

The main objective of the analysis was to evaluate the detection of wind-thrown forest in the dataset of satellite images acquired during phase 2, i.e. from 2009-09-17 until November 2009. The backscatter values from phase 3, i.e. from all images acquired during 2010, are included to permit an analysis of clear-cut signatures as a secondary objective.

4.1 TerraSAR-X

4.1.1. No shadow

For images acquired before the trees were felled, the backscatter values from the polygons that represent regions with no shadow were about 0.3 dB below the backscatter values from the reference forest and the temporal variability was identical (Fig. 6). This confirms that the forest in the test areas and in the reference areas were similar in terms of properties that are relevant for SAR backscatter at X-band. After felling, the backscatter values increased compared to the reference forest and the measured differences were between 1.2 dB and 2.0 dB. The backscatter values from the felled areas were also higher than those from the reference clear-cuts, but the differences were in most cases smaller than for the reference forest. Analysis of variance (ANOVA) was used for a statistical analysis. The null hypothesis tested was that the difference between backscatter values from test areas and reference forest were the same before and after the trees were felled. This hypothesis could be strongly rejected ($p < 0.001$). This implies that the observed differences are real and not coincidental.

For images acquired after the trees were removed, the variability of the backscatter from the test areas was larger, with a tendency towards higher values compared to the reference forest areas. At one occasion the difference with respect to the reference forest was 3.1 dB. This behaviour was also observed for the values from the reference clear-cuts during all three phases of the experiment. Differences between the test areas and the reference clear-cuts during phase 3 were likely due to the fact that the reference clear-cuts are three years older, which has allowed some growth of vegetation. This young vegetation could be enough to give more moderate variations in ground moisture. Slight differences in topography and surface roughness should also have a larger effect on the backscatter from clear-cuts than from mature or wind-thrown forest. The occasions when the backscatter is higher for clear-cuts than forest is in most cases related to rainfall (see Table 1) and predominantly occur for descending orbits, which could be explained by a more moist ground surface and vegetation during the early morning passes than during the late afternoon ascending passes.

4.1.2. Shadow and layover

The measured backscatter values for the shadow and layover regions are presented in Fig. 7 for ascending passes and in Fig. 8 for descending passes. For images acquired after the trees had been felled, the backscatter values in the shadow regions decreased from about -10 dB to around -19 dB. The backscatter differences between the shadow regions and the reference forest increased to values in the range from 7.8 dB to 9.2 dB for the ascending orbits and 6.5 dB to 8.6 dB for descending orbits. The backscatter in the layover regions increased and the backscatter difference between these regions and the reference forest was between 3.2 dB and 4.6 dB for ascending orbits and between 2.8 dB and 3.4 dB for descending orbits. The shadowing and layover appear when the trees are felled and remain as long as the trees that surround the test areas are still standing. This effect would in theory span both phase 2 and 3, but as shown in Fig. 7 and Fig. 8, the backscatter levels in correspondence of shadowing and layover disappear after the end of phase 2. When the felled trees were removed after phase 2, the forest manager at the Remningstorp estate decided to cut down a larger area, which included most of the trees surrounding the test areas T1 to T3 and all trees on the eastern side of T4.

4.2 RADARSAT-2

4.2.1. No shadow

The RADARSAT-2 backscatter shows many similarities with the TerraSAR-X backscatter, although some of the trends were not quite as clear. The values from test regions without shadow or layover were slightly lower than the values from the reference forest areas, but followed the same temporal variations until the trees are felled. For HH-polarized data (Fig. 9), the test area values were between 0.3 dB and 0.8 dB below the reference forest values. For HV polarization (Fig. 10), the backscatter was either 0.1 dB above the reference forest or at most 0.7 dB below.

In Figures 9 and 10, two image acquisitions have been included from the period when the felling was on-going. These acquisitions have been included for completeness and represent a transition period when the trees in parts of the test areas had been felled. For images acquired after the trees were felled, the backscatter was slightly above the level measured for the reference forest. The backscatter difference was between 0.2 dB and 1.2 dB for HH polarization, thus being less than the in the TerraSAR-X case. For HV-polarization the difference was between 0.1 dB and 1.1 dB.

For images acquired after the trees were removed, the backscatter decreased and in three cases out of four (one for HH and two for HV), the separation between the test areas and the reference forest was over 3 dB. On the fourth occasion, 2010-10-29, the backscatter for the test areas was instead 0.4 dB higher than for the reference forest. At all four dates there was no or negligible amounts of rainfall (see Table 2). However, while the three first acquisitions were preceded by dry and relatively warm periods, the conditions before the last acquisition were different. During the period 2010-10-21 to 2010-10-24 Remningstorp received 29 mm of precipitation, partly as snow, and this was followed by two days with temperatures below the freezing point. It is likely that on the acquisition day, the ground surfaces of the clear-cuts were still wet. As for TerraSAR-X, the backscatter values for the reference clear-cuts showed large temporal variations, but for the RADARSAT-2 measurements on any given day, the backscatter from the reference clear-cuts never reach values that are higher than from the reference forest.

4.2.2. Shadow and layover

Five RADARSAT-2 images were acquired during phase 2. Two images were acquired in HH polarization and three in HV polarization. The HH images and two of the HV images are from ascending passes and only one HV image is from a descending orbit. The measured backscatter values from the HH images are presented in Fig. 11 and the HV backscatter in Fig. 12 (ascending) and Fig. 13 (descending).

For the first HH image (2009-10-10) the backscatter values from the shadow regions are as low as -17.2 dB and the separation to the reference forest is 7.5 dB, while the backscatter value for the second HH image (2009-10-21) is -14.2 dB and the separation is only 4.9 dB. In addition to environmental differences between the two acquisition dates, a possible explanation to the difference could be that the smaller incidence angle of the RADARSAT-2 U3 observation mode that was used for the second acquisition gives less shadow within the shadow polygons than the larger incidence angle of the U25 mode that was used for the first acquisition. The difference between the backscatter levels from the regions with layover and the reference forest is 2.2 dB and 2.9 dB, which is lower than what was observed for the TerraSAR-X images.

The HV backscatter levels for the shadow regions range from -20.9 dB to -22.6 dB and the separation to the reference forest is between 5.9 dB and 7.0 dB. The HV images were acquired in the observation modes U14 and U16, so the differences in incidence angle are small and should not be the main cause for differences in the backscatter. The HV images cannot be compared with any TerraSAR-X data, but display a separation between layover and reference forest that is in the range 1.8 dB to 2.9 dB, which is on the same order as for the RADARSAT-2 HH data.

4.3 ALOS PALSAR

4.3.1. No shadow

The time series of ALOS PALSAR backscatter measurements in HH- and HV-polarization have been plotted in Fig. 14 and Fig. 15 respectively. Regardless of polarization, the values from the test regions without shadow and the reference forest only showed small differences (below 0.6 dB for HH-polarization and 0.5 dB for HV-polarization) during phase 1. For images acquired after the trees were felled, the backscatter of the test areas decreased compared to the backscatter level of the reference forest. The decrease was significantly larger for HH-polarization (1.6 dB compared to 0.4 dB and 0.8 dB for HV). For HH-polarization, the decrease in backscatter is likely due to removal of the double bounce component. The 1.6 dB decrease was in line with results from the experiment in Remningstorp in 2006 (Fransson et al., 2007). At HV-polarization, volume scattering is the main component and the scattering volume is still present when the trees have been felled. Conversely to the behaviour of the backscatter for the shorter wavelengths of TerraSAR-X and RADARSAT-2, at L-band the backscatter in phase 2 decreased with respect to the undisturbed conditions in phase 1. For images acquired after the trees had been removed, the backscatter from the test areas dropped with respect to the reference forest between 4.7 dB and 6.4 dB for HH-polarization and between 7.2 dB and 8.3 dB for HV-polarization. Compared to the backscatter measured in the reference clear-cut areas, the level of backscatter of the test areas was 1- 4 dB lower. In general the separation between the reference forest and the reference clear-cuts is considerably larger than for TerraSAR-X and RADARSAT-2. This is in line with theory that states that longer wavelengths are more sensitive to differences in forest biomass and therefore should give a larger dynamic range between low and high biomass (e.g. Le Toan, 1992).

4.3.2. Shadow and layover

Due to the relatively coarse resolution of the ALOS PALSAR data, the polygons that had been defined for regions with ascending or descending shadow contained too few pixels to give reliable backscatter values for this sensor. However, a comparison with values from the polygons without shadow or layover gives a clear indication that shadow and layover do affect the backscatter significantly also for ALOS PALSAR images at this coarse resolution.

5. Summary and discussion

The backscatter signatures from mature forest, felled trees and clear-cuts have been studied with satellite SAR data from Terra-SAR-X, RADARSAT-2 and ALOS-PALSAR. A summary of the backscatter difference between reference forest and test regions without shadowing or layover is presented in Fig. 16. For TerraSAR-X the backscatter (HH) increased when the trees were felled while for ALOS PALSAR the HH polarized backscatter decreased. In both cases the backscatter differences between reference forest and felled forest without shadowing or layover were in the range 1.2 to 2.0 dB. For RADARSAT-2 (HH and HV) and HV polarized ALOS PALSAR images, only minor changes in backscatter levels were detected when the trees were felled.

The decrease in backscatter that has been measured for regions where shadowing appear after the trees are felled is significantly larger than the change in backscatter for areas that are not affected by shadowing or layover. This indicates that identification of new shadows gives a more reliable detection of wind-thrown forest, but after a real storm the shadows might be more diffuse than from the square test areas that have been used in the experiments in Remningstorp. In addition, a field or an open area will never create a shadow if the neighbouring forest is blown down and shadows will only appear if there are trees that remain standing after the storm. To increase the chance to find new shadows, images should be acquired in both ascending and descending passes when possible.

When a tree is felled by strong wind it is either uprooted or the stem breaks. Uprooting often occur for trees with shallow root systems, e.g. the spruce that is common in Northern Europe. The uprooted root system is often several meters in diameter and cause additional roughness and scattering surfaces that has not been possible to simulate in the experiment described in this paper. This difference between the conducted experiment and real conditions is expected to have a larger effect on the backscatter for longer wavelengths and might introduce double bounce scattering if the trees are felled in the same direction as the look direction of the SAR. This should be taken into account in case an operational system for detection of wind-thrown forest is to be designed.

The study shows that the variations in backscatter levels are larger for clear-cuts than for mature forest, which can be explained by a larger sensitivity to changes in environmental conditions like moisture of the ground and vegetation. For TerraSAR-X the backscatter levels from the clear-cuts overlap those of mature forest, which imply that X-band SAR backscatter is not suitable for clear-cut detection or monitoring. With increasing wavelength the separation between backscatter levels from clear-cuts and mature forest increase (see phase 3 in Fig. 16) and the results from ALOS PALSAR confirm results from previous studies that have indicated that L-band SAR backscatter can be used for clear-cut detection.

This study has been limited to backscatter signatures. Further work will be focussed on possibilities to use texture measures for detection of wind-thrown forest. Available material could also allow a sensitivity analysis for incidence angles and deviations between tree trunk direction and orbit direction, which has shown to influence detectability of wind-thrown forest for fine resolution low frequency airborne SAR systems (Fransson et al., 2007). A limited number fully polarimetric ALOS PALSAR images from 2006 and Radarsat-2 images from 2009 might also allow an evaluation of the usefulness of spaceborne SAR polarimetry for detection of shifts in scattering components when trees are felled.

Acknowledgments

This work was financially supported by the Swedish National Space Board and the Hildur and Sven Wingquist’s Foundation for Forest Research. ALOS PALSAR data have been provided by JAXA EORC within the framework of the JAXA Kyoto & Carbon Initiative. Data from RADARSAT-2 were granted within the Canadian program for Science and Operational Applications Research for RADARSAT-2 (SOAR), project number 3931 and data from TerraSAR-X were provided by the German Aerospace Center (DLR) under the agreement for proposal LAN0126. Meteorological observations from Remningstorp were available through a license agreement with SMHI. A. Pantze is acknowledged for his contribution to the planning of the storm simulation. G. Sandberg, Chalmers University of Technology is acknowledged for advice on the statistic analysis.

References

Anon. (2006). Stormen 2005 – en skoglig analys. *Meddelande 1*. Skogsstyrelsen. 199 s. (In Swedish).

Dwyer, E., Pasquali, P., Holecz, F., & Arino, O. (2000). Mapping Forest Damage Caused by the 1999 Lothar Storm in Jura (France), Using SAR Interferometry. *Earth Observation Quarterly, 65*, 28-29.

Folkesson, K., Hallberg, B., Smith-Jonforsen, G., Fransson, J.E.S., Magnusson, M., and Ulander, L.M.H. (2006). Automatic detection of wind-thrown forest in VHF SAR images. *Proceedings of IEEE International Geoscience and Remote Sensing Symposium 2006*, Denver, USA, 31 July – 4 August, 3599–3602.

Fransson, J.E.S., Gustavsson, A., Ulander, L.M.H., & Walter, F. (2001). Mapping of wind-thrown forests using CARABAS-II VHF SAR image data. *Proceedings of IEEE International Geoscience and Remote Sensing Symposium 2001*, Sydney, Australia, 9-13 July, vol. 6, 2737-2739.

Fransson, J.E.S., Walter, F., Blennow, K., Gustavsson, A., & Ulander, L.M.H. (2002). Detection of storm-damaged forested areas using airborne CARABAS-II VHF SAR image data. *IEEE Transactions on Geoscience and Remote Sensing*, *40*(10), 2170- 2175.

Fransson, J.E.S., Magnusson, M., Folkesson, K., Hallberg, B., Sandberg, G., Smith-Jonforsen, G., Gustavsson, A., & Ulander, L.M.H. (2007). Mapping of Wind-Thrown Forests Using VHF/UHF SAR Images. *Proceedings of International Geoscience and Remote Sensing Symposium 2007*, Barcelona, Spain, July 23–27.

Fransson, J.E.S., Magnusson, M., Olsson, H., Eriksson, L.E.B., Sandberg, G., Smith-Jonforsen, G., & Ulander, L.M.H. (2007). Detection of forest changes using ALOS PALSAR satellite images. *Proceedings of International Geoscience and Remote Sensing Symposium 2007*, Barcelona, Spain, July 23–27. 2330–2333.

Fransson, J.E.S., Pantze, A., Eriksson, L.E.B., Soja, M.J., & Santoro, M. (2010). Mapping of wind-thrown forests using satellite SAR images. *Proceedings of IEEE International Geoscience and Remote Sensing Symposium 2010*, Hawaii, USA, 25-30 July, 1242-1245.

Le Toan, T., Beaudoin, A., Riom, J., & Guyon, D. (1992). Relating Forest Biomass to SAR Data. *IEEE Transactions on Geoscience and Remote Sensing, 30*(2), 403-411.

Nezry, E., Yakam-Simen, F., Romeijn, P., Supit, I., & Bally, Ph. (2000). Assessment of Mitch Hurricane Damages in Honduras, Nicaragua and El-Salvador Using ERS and SPOT Images. *Proceedings of ESA ENVISAT Symposium*, Gothenburg, Sweden, 16-20 October, ESA SP-461.

Rosenqvist, Å., Shimada, M., Ito, N., & Watanabe, M. (2007). ALOS PALSAR: A pathfinder mission for global-scale monitoring of the environment. *IEEE Transactions on Geoscience and Remote Sensing*, *45*(11), 3307–3316.

Schelhaas, M-J., Nabuurs, G-J., & Schuck, A. (2003). Natural disturbances in the European forests in the 19th and 20th centuries. *Global Change Biology*, *9*, 1620–1633.

Steinmeier, C., Schwarz, M., Holecz, F., Stebler, O., & Wagner, S. (2002). The evaluation of different sensors and techniques for the detection of storm damages in forests. *Proceedings of IEEE International Geoscience and Remote Sensing Symposium 2002*, Toronto, Canada, 24-28 June 2002, vol.3, 1774- 1776.

Touzi, R., Sikaneta, I., Landry, R., & Yeremy, M. (1999). On the use of the polarization information for ice storm tree damage assessment in the Ottawa region. *Proceedings of IEEE International Geoscience and Remote Sensing Symposium 1999*, Hamburg, Germany, 28 June – 2 July, vol.5, 2455-2457.

Ulander, L.M.H., Smith, G., Eriksson, L., Folkesson, K., Fransson, J.E.S., Gustavsson, A., Hallberg, B., Joyce, S., Magnusson, M., Olsson, H., Persson, A., & Walter, F. (2005). Mapping of wind-thrown forests in southern Sweden using space- and airborne SAR. *Proceedings of IEEE International Geoscience and Remote Sensing Symposium 2005*, Seoul, Korea, July 25-29, 3619–3622.

Ulander, L.M.H., Gustavsson, A., Smith-Jonforsen, G., Folkesson, K., Hallberg, B., Eriksson, L., Fransson, J.E.S., & Magnusson, M. (2006). Mapping of wind-thrown forests using the VHF-band CARABAS-II SAR". *Proceedings of IEEE International Geoscience and Remote Sensing Symposium 2006*, Denver, USA, 31 July – 4 August, 3684–3687.

Wang, H., Ouchi, K., & Ya-Qiu Jin (2010). Extraction of typhoon-damaged forests from multi-temporal high-resolution polarimetric SAR images. *IEEE International Geoscience and Remote Sensing Symposium 2010*, Hawaii, USA, 25-30 July, 3271-3274.

Wegmüller, U. (1999). Automated terrain corrected SAR geocoding, *Proceedings of IEEE International Geoscience and Remote Sensing Symposium 1999*, Hamburg, Germany, 28 June – 2 July, 1712-1714.

Wiesmann, A., Demargne, L., Ribbes, F., Honikel, M., Yesou, H., & Wegmuller, U. (2000). Forest Storm Damage Assessment with ERS Tandem Data. *Proceedings of ESA ENVISAT Symposium*, Gothenburg, Sweden, 16-20 October, ESA SP-461.

Yesou, H., Weber, S., Herrmann, A., Fellah, K., Bally, Ph., Bequignon, J., & de Fraipont, P. (2000). Mapping Storm Forest Damage Using SAR Coherence Data. The Case of the Haguneau Forest – France. *Proceedings of ESA ENVISAT Symposium*, Gothenburg, Sweden, 16-20 October, ESA SP-461.

Tables

Table 1. List of the TerraSAR-X data, including information about acquisition date, observation mode (HS = High resolution Spotlight), track number (incidence angles: 2 = 43.6°, 55 = 49.5°, 78 = 34.0°, 146 = 41.4°), flight direction (Asc = ascending, Desc = descending), polarization (HH = horizontal co-polarized) and environmental conditions (T = temperature, PD = previous day) at and before the acquisition.

ID	Acquisition date	Obs. mode	Track	Flight direction	Polarization	Environmental conditions
X1	2009-08-24	HS	146	Asc	HH	T≈16 °C; Dry
X2	2009-08-26	HS	2	Desc	HH	T≈15 °C; Rain: 2 mm + 3 mm PD
X3	2009-08-29	HS	55	Asc	HH	T≈13 °C; Rain: 4 mm + 16 mm PD
X4	2009-08-31	HS	78	Desc	HH	T≈14 °C; Rain: < 1 mm
X5	2009-09-04	HS	146	Asc	HH	T≈13 °C; Rain: 4 mm + 13 mm PD
X6	2009-09-06	HS	2	Desc	HH	T≈14 °C; Rain: 22 mm PD
X7	2009-10-03	HS	78	Desc	HH	T≈6 °C; Rain: 19 mm
X8	2009-10-07	HS	146	Asc	HH	T≈9 °C; Rain: 6 mm PD
X9	2009-10-09	HS	2	Desc	HH	T≈4 °C; Rain: 9 mm PD
X10	2009-10-12	HS	55	Asc	HH	T≈4 °C; Rain: 7 mm + 1 mm PD
X11	2009-10-14	HS	78	Desc	HH	T≈-1 °C; No precipitation

X12	2009-10-18	HS	146	Asc	HH	T≈2 °C; Frozen at night; No precip.
X13	2009-10-20	HS	2	Desc	HH	T≈5 °C; Rain: 2 mm + 2 mm PD
X14	2009-10-23	HS	55	Asc	HH	T≈5 °C; Rain: 1 mm
X15	2010-08-22	HS	146	Asc	HH	T≈15 °C; Rain: 4 mm PD
X16	2010-08-24	HS	2	Desc	HH	T≈14 °C; Rain: 9 mm + 5 mm PD
X17	2010-08-27	HS	55	Asc	HH	T≈12 °C; Rain: 6 mm, 5 days: 47 mm
X18	2010-09-02	HS	146	Asc	HH	T≈10 °C; Dry
X19	2010-09-04	HS	2	Desc	HH	T≈8 °C; Dry
X20	2010-09-07	HS	55	Asc	HH	T≈12 °C; Dry

Table 2. List of the RADARSAT-2 data, including information about acquisition date, observation mode (U = Ultra-fine resolution beam with the following elevation angles to inner edge of beam: U3 = 27.8°, U14 = 35.0°, U16 = 36.2°, U25 = 40.9°), track number, flight direction (Asc = ascending, Desc = descending), polarization (HH = horizontal co-polarized, HV = cross-polarized) and environmental conditions (T = temperature, PD = previous day) at and before the acquisition.

ID	Acquisition date	Obs. mode	Track	Flight direction	Polarization	Environmental conditions
R1	2009-07-27	U14	209	Desc	HV	T≈14 °C; Rain: 10 mm, 5 days: 49 mm
R2	2009-07-30	U25	259	Asc	HH	T≈16 °C; Rain: 9 mm
R3	2009-08-20	U14	209	Desc	HV	T≈16 °C; Rain: 2 mm
R4	2009-08-23	U25	259	Asc	HH	T≈15 °C; Dry
R5	2009-09-03	U3	73	Asc	HH	T≈15 °C; Rain: 13 mm + 4 mm PD
R6	2009-09-06	U16	116	Asc	HV	T≈14 °C; Rain: 0 mm, 5 days: 43 mm
R7	2009-09-13	U14	209	Desc	HV	T≈12 °C; Dry

R8	2009-09-16	U25	259	Asc	HH	T≈10 °C; Dry
R9	2009-09-30	U16	116	Asc	HV	T≈4 °C; Rain: 14 mm
R10	2009-10-07	U14	209	Desc	HV	T≈9 °C; Rain: 6 mm PD
R11	2009-10-10	U25	259	Asc	HH	T≈4 °C; Frozen at night; No precip.
R12	2009-10-21	U3	73	Asc	HH	T≈4 °C; Rain: 2 mm PD
R13	2009-10-24	U16	116	Asc	HV	T≈4 °C; Rain: 1 mm + 1 mm PD
R14	2010-09-08	U14	209	Desc	HV	T≈13 °C; Dry
R15	2010-09-11	U25	259	Asc	HH	T≈14 °C; Rain: 2 mm + 1 mm PD
R16	2010-10-02	U14	209	Desc	HV	T≈9 °C; Dry
R17	2010-10-29	U25	259	Asc	HH	T≈8 °C; Rain: 1 mm PD

Table 3. List of the ALOS PALSAR data, including information about acquisition date, observation mode (FBD34 = Fine Beam Dual polarization with look angle 34.3°), Reference System for Planning (RSP) number, flight direction (Asc = ascending, Desc = descending), polarization (HH = horizontal co-polarized, HV = cross-polarized) and environmental conditions (T = temperature, PD = previous day) at and before the acquisition.

ID	Acquisition date	Obs. mode	RSP	Flight direction	Polarization	Environmental conditions
A1	2008-05-03	FBD34	629	Asc	HH + HV	T≈11 °C; Rain: 18 mm PD
A2	2008-05-20	FBD34	630	Asc	HH + HV	T≈8 °C; Dry
A3	2008-08-03	FBD34	629	Asc	HH + HV	T≈17 °C; Rain: 1 mm + 2 mm PD
A4	2008-08-20	FBD34	630	Asc	HH + HV	T≈15 °C; Rain: 8 mm + 1 mm PD
A5	2008-10-05	FBD34	630	Asc	HH + HV	T≈8 °C; Rain 11 mm + 3 mm PD
A6	2009-07-08	FBD34	630	Asc	HH + HV	T≈16 °C; Rain: 9 mm, 5 days: 57 mm
A7	2009-09-21	FBD34	629	Asc	HH + HV	T≈12 °C; Rain: 1 mm

A8	2009-10-08	FBD34	630	Asc	HH + HV	T≈5 °C; Rain: 9 mm
A9	2010-08-09	FBD34	629	Asc	HH + HV	T≈16 °C; Rain: 6 mm + 5 mm PD
A10	2010-08-26	FBD34	630	Asc	HH + HV	T≈13 °C; Rain: 8 mm, 4 days: 41 mm
A11	2010-09-24	FBD34	629	Asc	HH + HV	T≈15 °C; Rain: 9 mm
A12	2010-10-11	FBD34	630	Asc	HH + HV	T≈2 °C; Frozen at night; No precip.

Figures

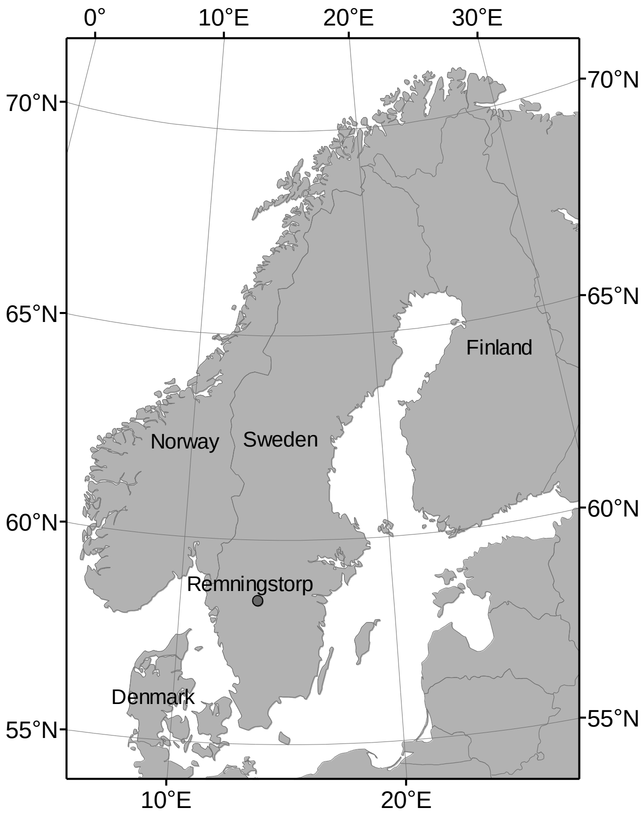

Fig. 1. The location of Remningstorp test site, shown on a map of Northern Europe.

Fig. 2. A mosaic of digital aerial photographs captured by a UAV (courtesy SmartPlanes AB) covering three of the simulated wind-thrown forest stands, each with a size of about 110 × 110 m^2.

Fig. 3. Photograph taken from the ground of one of the simulated wind-thrown stands.

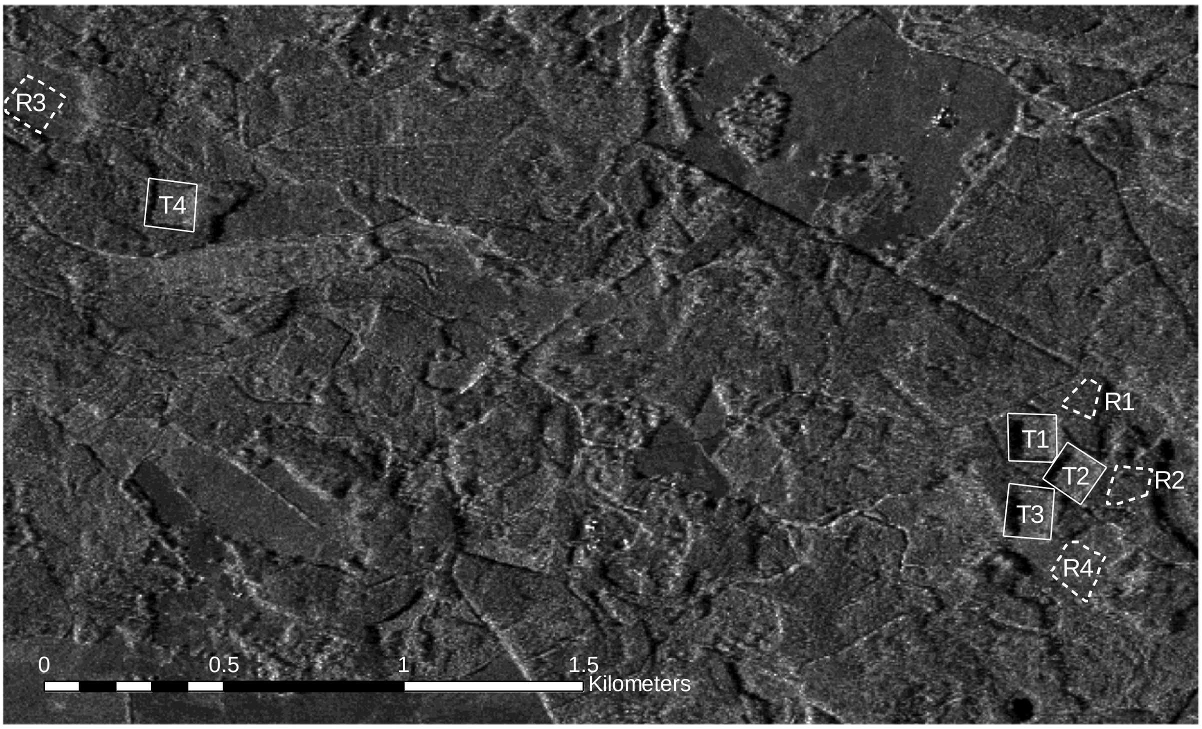

Fig. 4. Location of test areas (T1-T4) and reference areas (R1-R4). R1 and R2 are reference forest and R3 and R4 are reference clear-cuts. The background image is a temporal average of four TerraSAR-X images with acquisition dates 2009-10-07, 2009-10-12, 2009-10-18 and 2009-10-23.

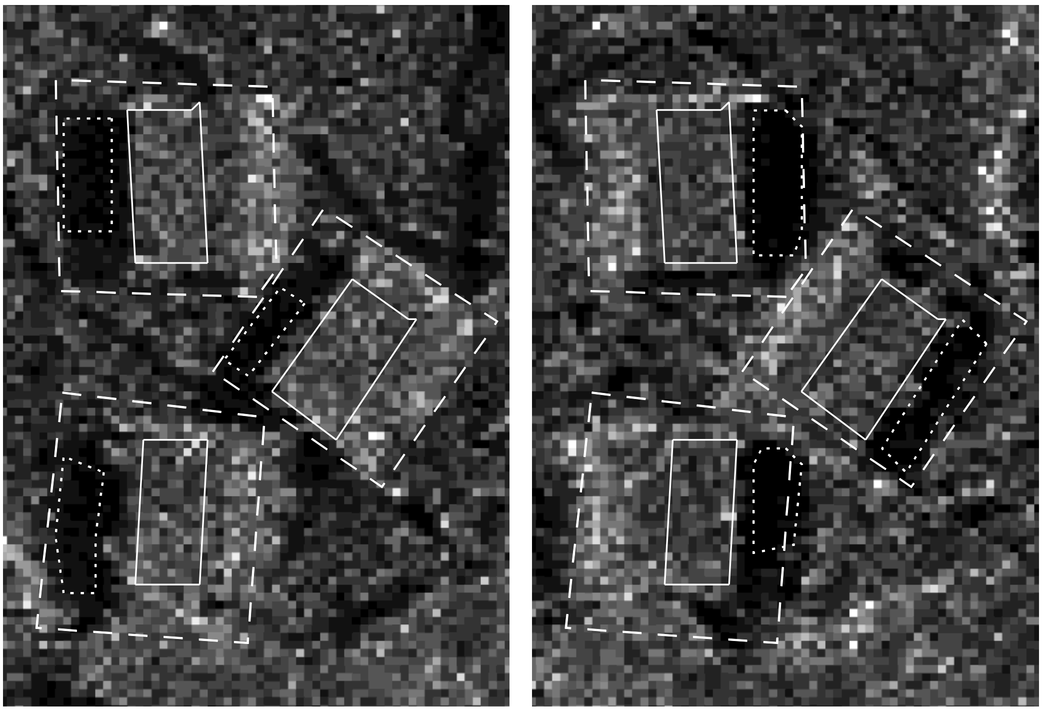

Fig. 5. The left image shows the division of the test areas T1, T2 and T3 into shadowed and non-shadowed regions for ascending passes (in this case the TerraSAR-X image from track 55 acquired 2009-10-23). The right image shows the regions that have been used for descending passes (exemplified by TerraSAR-X image from track 2, acquired 2009-10-09). The perimeters of the test areas are indicated with dashed lines, while polygons for shadow are marked with dotted lines and polygons for regions without shadow with solid lines.

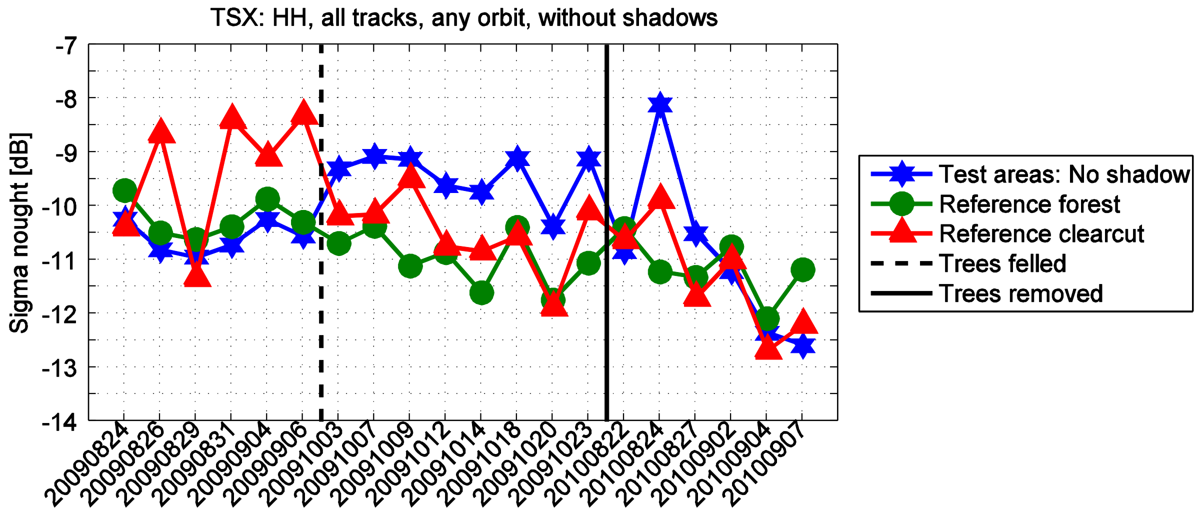

Fig. 6. Time series of TerraSAR-X backscatter values for regions of the test areas without shadow. Includes all acquired images from both ascending and descending passes.

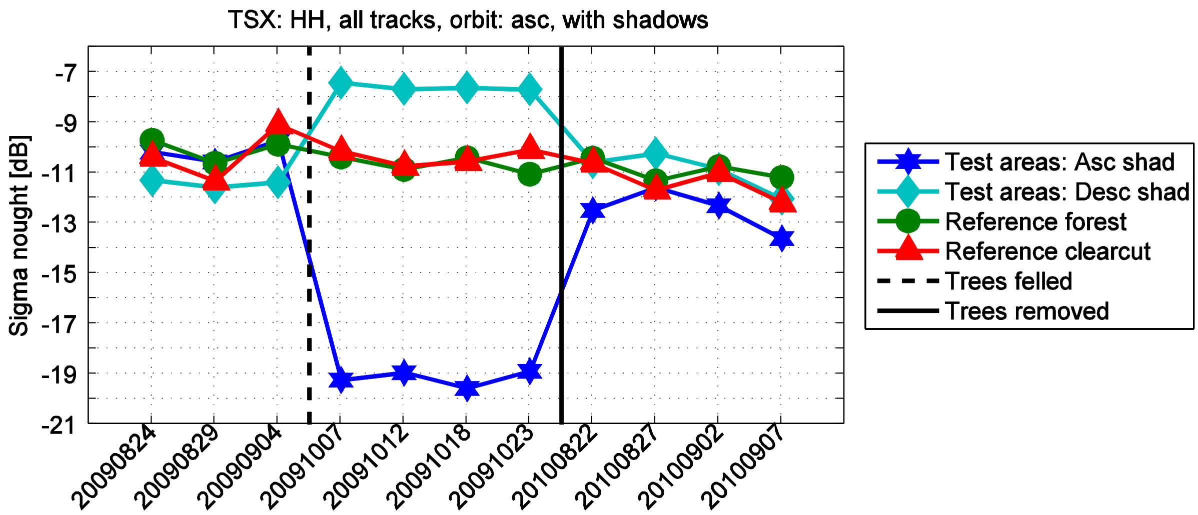

Fig. 7. Time series of TerraSAR-X backscatter values for regions of the test areas with shadow or layover. Includes all acquired images from ascending passes.

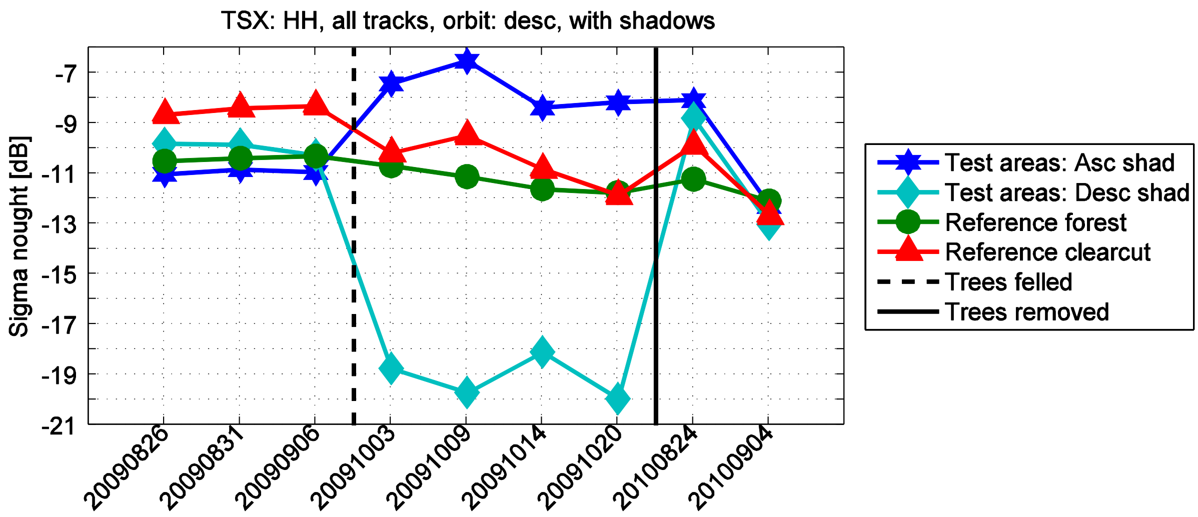

Fig. 8. Time series of TerraSAR-X backscatter values for regions of the test areas with shadow or layover. Includes all acquired images from descending passes.

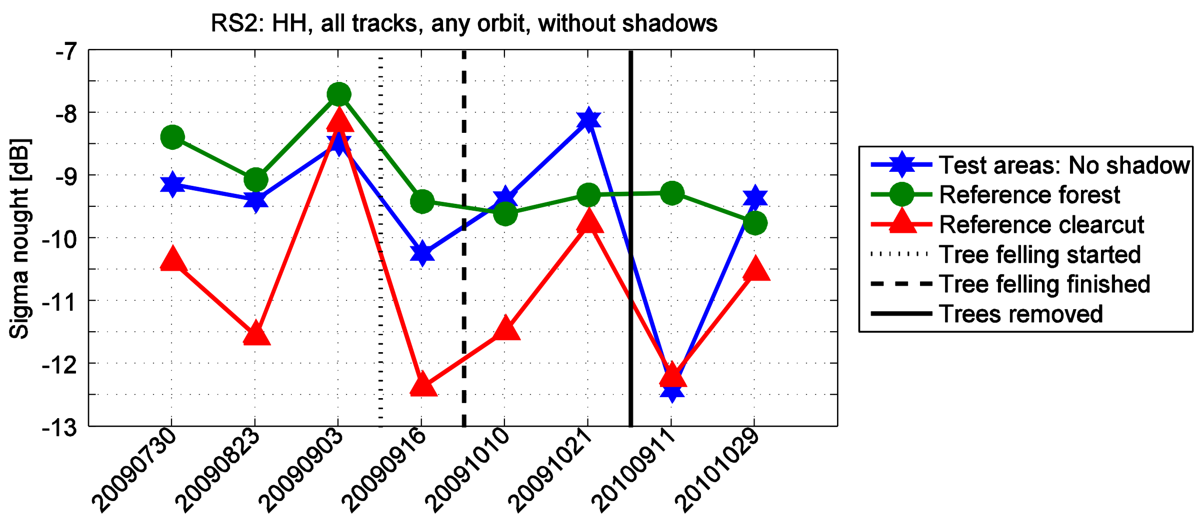

Fig. 9. Time series of RADARSAT-2 backscatter values for regions of the test areas without shadow. Includes all acquired images with HH polarization. All images are from ascending passes.

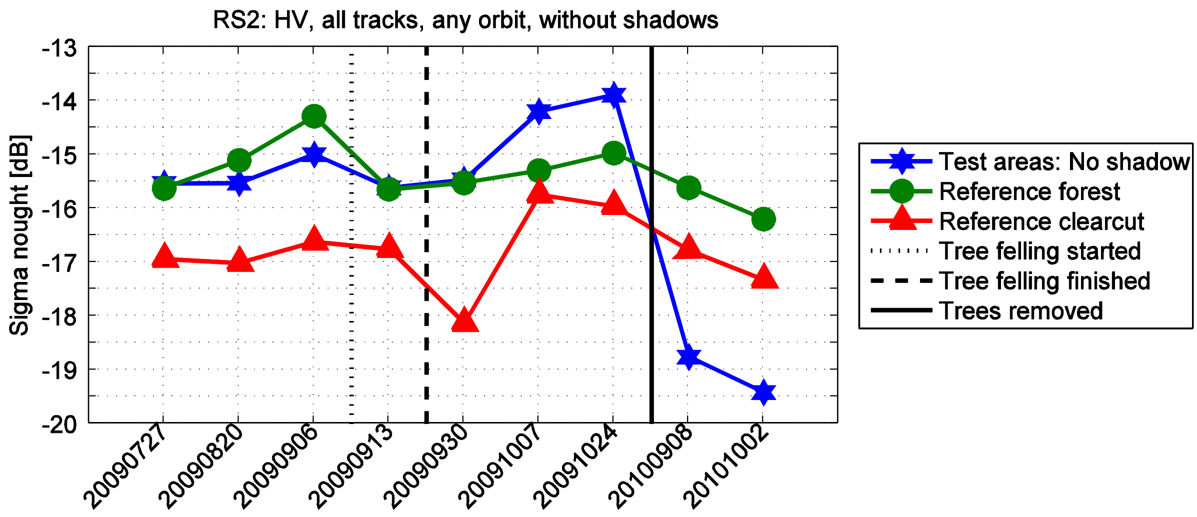

Fig. 10. Time series of RADARSAT-2 backscatter values for regions of the test areas without shadow. Includes all acquired images with HV polarization from both ascending and descending passes.

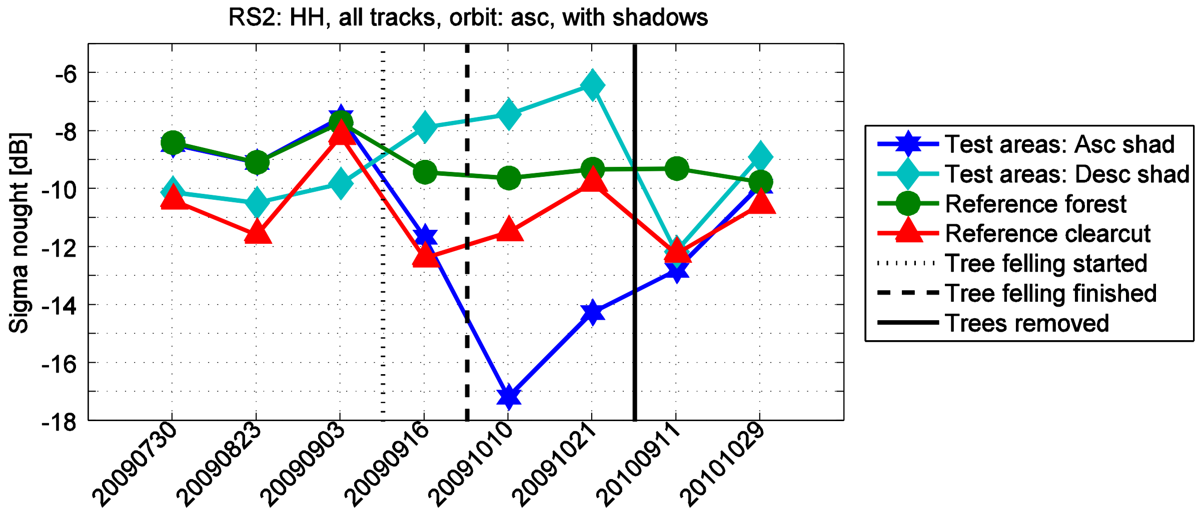

Fig. 11. Time series of RADARSAT-2 backscatter values for regions of the test areas with shadow or layover. Includes all acquired images with HH polarization. All images are from ascending passes.

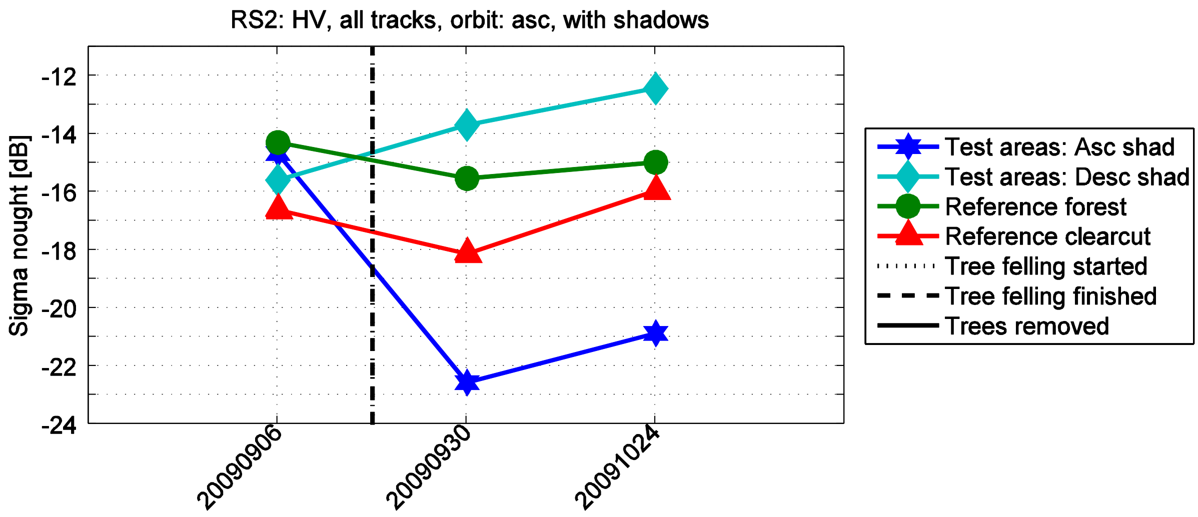

Fig. 12. Time series of RADARSAT-2 backscatter values for regions of the test areas with shadow or layover. Includes all acquired images with HV polarization from ascending passes.

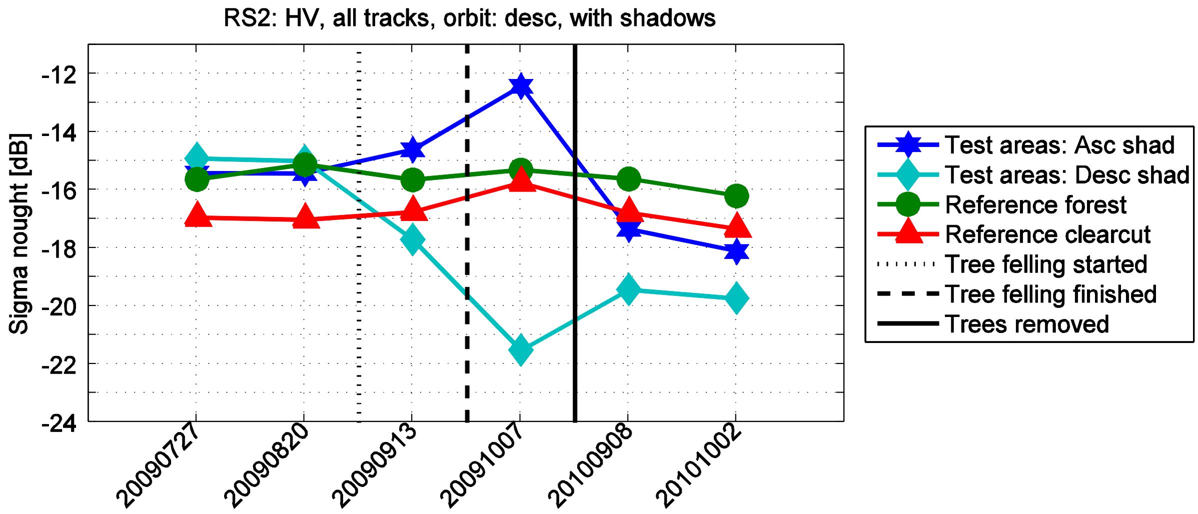

Fig. 13. Time series of RADARSAT-2 backscatter values for regions of the test areas with shadow or layover. Includes all acquired images with HV polarization from descending passes.

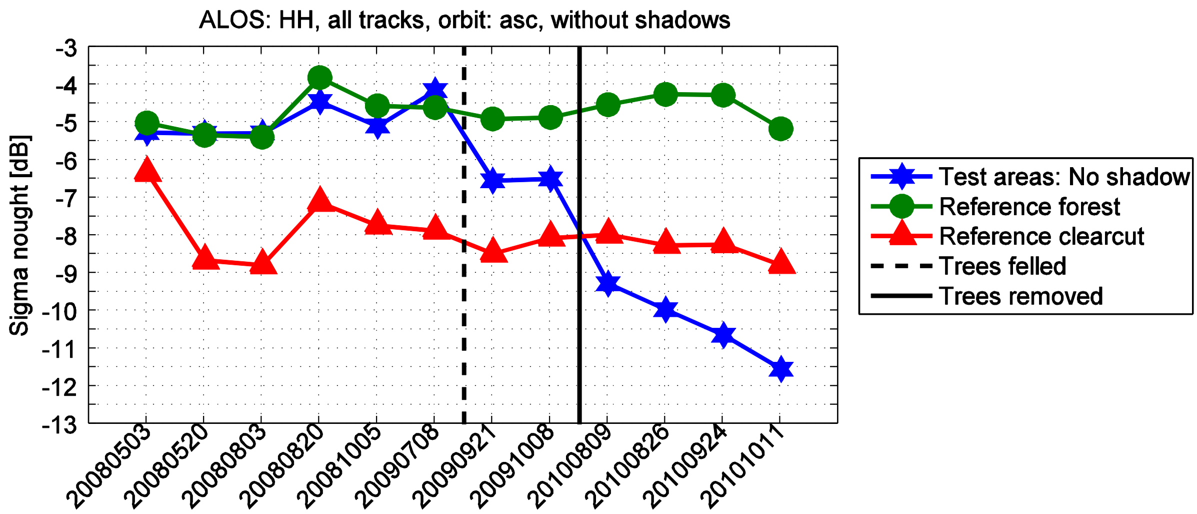

Fig. 14. Time series of ALOS PALSAR backscatter values for regions of the test areas without shadow. Includes all acquired images with HH polarization. All images are from ascending passes.

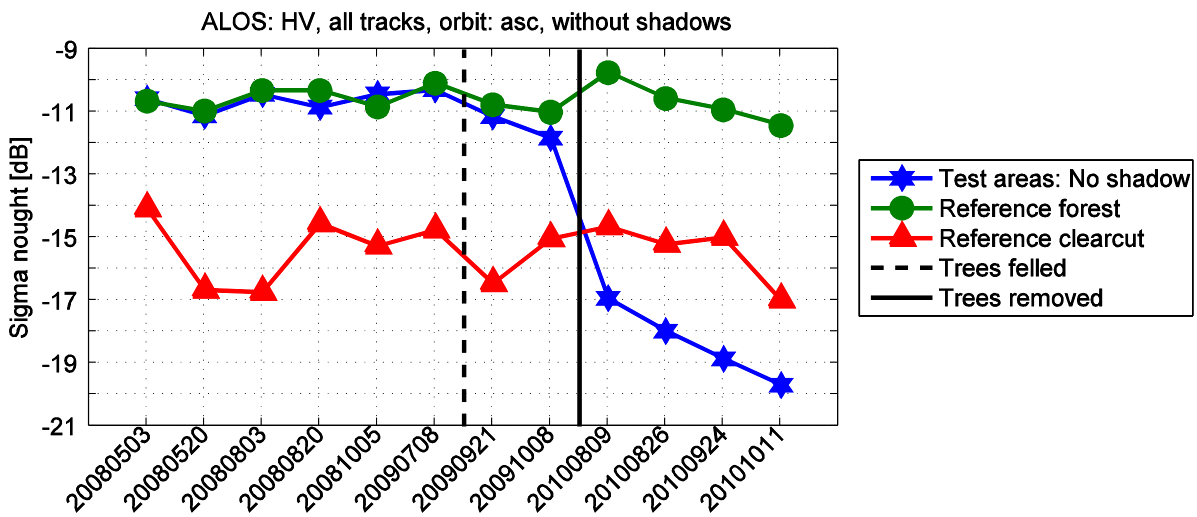

Fig. 15. Time series of ALOS PALSAR backscatter values for regions of the test areas without shadow. Includes all acquired images with HV polarization. All images are from ascending passes.

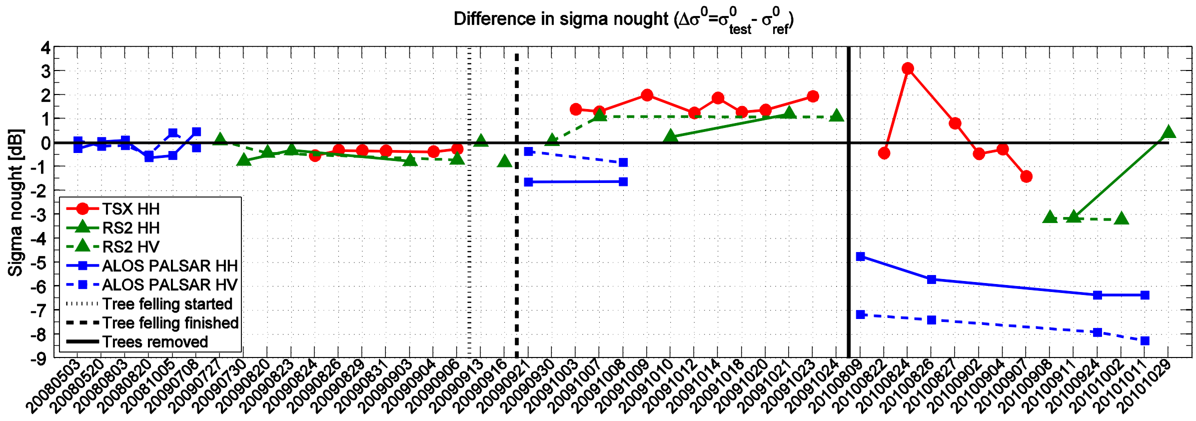

Fig. 16. Differences in sigma nought between test regions without shadow and reference forest. The temporal spacing along the x-axis is not equidistant.